

PHOTOMETRY AND PROPER MOTIONS OF M, L, AND T DWARFS FROM THE Pan-STARRS1 3π SURVEY

WILLIAM M. J. BEST¹, EUGENE A. MAGNIER¹, MICHAEL C. LIU¹, KIMBERLY M. ALLER¹, ZHOUIAN ZHANG¹, W. S. BURGETT², K. C. CHAMBERS¹, P. DRAPER³, H. FLEWELLING¹, N. KAISER¹, R.-P. KUDRITZKI¹, N. METCALFE³, J. L. TONRY¹, R. J. WAINSCOAT¹, C. WATERS¹

¹Institute for Astronomy, University of Hawaii, 2680 Woodlawn Drive, Honolulu, HI 96822, USA; wbest@ifa.hawaii.edu

²GMTO Corporation, 465 N. Halstead St., Suite 250, Pasadena, CA 91107, USA

³Department of Physics, Durham University, South Road, Durham DH1 3LE, UK

ABSTRACT

We present a catalog of 9888 M, L and T dwarfs detected in the Pan-STARRS1 3π Survey (PS1), covering three-quarters of the sky. Our catalog contains nearly all known objects of spectral types L0–T2 in the PS1 field, with objects as early as M0 and as late as T9, and includes PS1, 2MASS, AllWISE, and *Gaia* DR1 photometry. We analyze the different types of photometry reported by PS1, and use two types in our catalog to maximize both depth and accuracy. Using parallaxes from the literature, we construct empirical SEDs for field ultracool dwarfs spanning $0.5 - 12 \mu\text{m}$. We determine typical colors of M0–T9 dwarfs, and we highlight the distinctive colors of subdwarfs and young objects. Our catalog includes 494 L dwarfs detected in r_{P1} , the largest sample of L dwarfs detected at such blue wavelengths. We combine astrometry from PS1, 2MASS, and *Gaia* DR1 to calculate new proper motions for our catalog. We achieve a median precision of 2.9 mas yr^{-1} , a factor of $\approx 3-10$ improvement over previous large catalogs. Our catalog contains proper motions for 2405 M6–T9 dwarfs and includes the largest set of homogeneous proper motions for L and T dwarfs published to date, 406 objects for which there were no previous measurements, and 1176 objects for which we improve upon previous literature values. We analyze the kinematics of ultracool dwarfs in our catalog and find evidence that bluer but otherwise generic late-M and L field dwarfs (i.e., not subdwarfs) tend to have higher tangential velocities compared to typical field objects. With the public release of the PS1 data, this survey will continue to be an essential tool for characterizing the ultracool dwarf population.

Keywords: brown dwarfs — stars: late-type

1. INTRODUCTION

Ultracool dwarfs (spectral types M6 and later) are the lowest-mass members of the stellar population, encompassing the coolest stars, brown dwarfs, and planetary-mass objects. The discovery of brown dwarfs over 20 years ago launched an understanding of the complex properties and evolution of ultracool atmospheres (e.g., Burrows et al. 2006), and allowed us to constrain the low-mass end of the stellar mass and luminosity functions in the solar neighborhood (Marocco et al. 2015, and references therein). In addition, the youngest ($\approx 10-100$ Myr) ultracool dwarfs in the field appear to be our best analogs to directly-imaged giant planets (e.g., Liu et al. 2013), and they are far easier to observe without the drowning glare of host stars. The major drivers for ultracool discoveries, which now include $\approx 2,000$ L and T dwarfs and many thousands of late-M dwarfs, have been wide-field imaging surveys such as the Deep Near Infrared Survey of the Southern Sky (DENIS, Epchtein et al. 1999), the Sloan Digital Sky Survey (SDSS; York et al. 2000), the Two Micron All Sky Survey (2MASS; Skrutskie et al. 2006), the UKIRT Infrared Deep Sky Survey (UKIDSS; Lawrence et al. 2007), and the Wide-Field Infrared Survey Explorer (*WISE*; Wright et al. 2010).

Large photometric samples obtained from these imaging surveys have provided much of our fundamental knowledge about ultracool dwarfs. Samples of L dwarfs have revealed a surprising diversity of near-IR colors (e.g. Leggett et al. 2002; Knapp et al. 2004; Gizis et al. 2012) which are believed to be caused by variations in surface gravity and/or dusty clouds (e.g. Kirkpatrick et al. 2008; Allers & Liu 2013a) or thermo-chemical instabilities (Tremblin et al. 2016). Objects transitioning from L to T spectral types undergo a dramatic shift to bluer near-IR colors thought to be driven by the clearing of clouds and the formation of methane (e.g., Burgasser et al. 2002; Chiu et al. 2006; Saumon

& Marley 2008). UKIDSS and *WISE* have illustrated the diversity of late-T and Y dwarf near- and mid-IR colors (e.g., Burningham et al. 2010a; Kirkpatrick et al. 2011; Mace et al. 2013), and *WISE* has enabled the discovery of the coolest known substellar objects (e.g., Cushing et al. 2011; Kirkpatrick et al. 2012; Luhman 2014). Large samples have revealed the mass and luminosity functions of the local ultracool population (e.g., Allen et al. 2005; Cruz et al. 2007; Burningham et al. 2010a). Measurements of the space density of brown dwarfs (e.g. Reid et al. 2008; Metchev et al. 2008) have identified a relative paucity of L/T transition dwarfs, indicating that this evolutionary phase is short-lived and constraining the birth history of substellar objects (e.g., Day-Jones et al. 2013; Marocco et al. 2015). The surveys have also enhanced brown dwarf searches in star-forming regions (e.g., Lodieu et al. 2009; Martín et al. 2010), important for determination of the substellar initial mass function. Photometric samples encompassing more than one survey have enabled us to determine ultracool colors across a broad range of wavelengths (e.g., Schmidt et al. 2015; Skrzypek et al. 2015) and to measure bolometric luminosities that yield effective temperatures and constraints on atmospheric and evolutionary models (e.g. Leggett et al. 2002; Golimowski et al. 2004).

Similarly, large samples of proper motions have contributed significantly to our discovery and understanding of the ultracool population. Proper motions have enabled searches to distinguish ultracool dwarfs from distant luminous red objects such as giants and galaxies (e.g., Kirkpatrick et al. 2000; Lépine & Shara 2005; Theissen et al. 2016, 2017) and to determine whether individual discoveries are members of star-forming regions (e.g., Lodieu et al. 2007a, 2012a). Proper motions have helped to find objects in crowded areas of the sky such as the Galactic plane (e.g., Luhman 2013; Smith et al. 2014b) and to identify ultracool dwarfs with atypical colors that were missed by color cuts used in photometry-only searches (e.g., Kirkpatrick et al. 2010). Several studies have found clear evidence for dynamically cold (slow-moving) and hot (fast-moving) populations of ultracool dwarfs that are consistent with thin disk and thick disk/halo populations (e.g., Faherty et al. 2009; Schmidt et al. 2010; Dupuy & Liu 2012), implying that ultracool dwarfs form in the same manner as hotter stars. Searches for high-proper motion objects, often using surveys with shorter time baselines, have identified rare fast-moving objects that are typically members of the older, low-metallicity populations (e.g., Jameson et al. 2008; Smith et al. 2014a; Kirkpatrick et al. 2014) or very nearby, previously overlooked objects (e.g., Luhman & Sheppard 2014; Luhman 2014; Schneider et al. 2016a; Kirkpatrick et al. 2016). Proper motions measured from the large surveys have enabled us to identify the substellar members of nearby young moving groups (e.g., Gagné et al. 2015b,c; Faherty et al. 2016; Liu et al. 2016), a population crucial to our understanding of brown dwarf evolution over their first few hundred million years. Proper motions from large catalogs have also identified wide comoving companions to higher-mass stars whose ages and metallicities can more easily be determined (e.g., Zhang et al. 2013; Luhman et al. 2012; Burningham et al. 2013; Smith et al. 2014b), making the ultracool companions important benchmarks for constraining atmospheric and evolutionary models.

The Panoramic Survey Telescope And Rapid Response System (Pan-STARRS1) is a large multi-epoch, multi-wavelength, optical imaging survey using a 1.8-m wide-field telescope on Haleakala, Maui (Kaiser et al. 2010). Pan-STARRS1 uses a 1.4 gigapixel camera (GPC1) with a $0''.258$ pixel scale. The Pan-STARRS1 3π Survey (PS1; Chambers et al. 2017) observed the entire sky north of $\delta = -30^\circ$ (three-quarters of the sky) in five filters ($g_{P1}r_{P1}i_{P1}z_{P1}y_{P1}$) over four years (2010 May – 2014 March), imaging ≈ 12 times in each filter and achieving a median angular resolution of $\approx 1''.1$ with a floor of $\approx 0''.7$ (Magnier et al. 2017). PS1 images are ~ 1 mag deeper in z -band than the most comparable optical survey to date (SDSS), and the novel y_{P1} filter (0.918–1.001 μm) extends further toward the near-infrared than previous optical surveys. This long-wavelength sensitivity allows PS1 to better detect and characterize red objects such as ultracool dwarfs. In addition, the multi-epoch astrometry of PS1 enables precise measurement of proper motions and parallaxes that help to distinguish faint, nearby ultracool dwarfs from reddened background stars and galaxies.

Significant ultracool discoveries from PS1 include many wide ultracool companions to main sequence stars (Deacon et al. 2012a,b, 2014) and young stars (Aller et al. 2013), L/T transition dwarfs that are difficult to identify with near-IR photometry alone (Deacon et al. 2011; Best et al. 2013, 2015), new low-mass members of the Hyades (Goldman et al. 2013) and Praesepe (Wang et al. 2014a), and new brown dwarf members of nearby young moving groups (Liu et al. 2013; Aller et al. 2016). PS1 has also enabled studies with large samples of more massive stars, including fiducial sequences of Galactic star clusters (Bernard et al. 2014), proper motions and wide binaries in the *Kepler* field (Deacon et al. 2016, who also present SEDs for spectral types B9V through M9V in the PS1 photometric system), and photometric distances and reddening for all stars detected by PS1 (Green et al. 2014; Schlafly et al. 2014). PS1 can detect ultracool dwarfs at larger distances than SDSS and 2MASS, so its optical photometry helps to create a rich multi-color catalog that will enable even bigger searches based solely on photometry, a precursor to science with the Large Synoptic Survey Telescope (LSST; Ivezić et al. 2008). In addition, the proper motions and parallaxes in PS1 should be fertile ground for identifying more ultracool dwarfs that have eluded detection due to their locations in

crowded areas of the sky (e.g., [Liu et al. 2011](#)), or are too red and faint to be measured by *Gaia* ([Gaia Collaboration et al. 2016b](#)).

In this paper we present a comprehensive catalog of ultracool dwarfs observed by PS1, including photometry, proper motions, spectral types, gravity classifications, and multiplicity. Section 2 describes the contents and assembly of our catalog. The PS1 photometry and proper motions are discussed in detail in Sections 3 and 4, respectively. We briefly describe a binary M7 dwarf newly identified by PS1 in Section 5. We summarize our catalog and its features in Section 6.

2. CATALOG

Our catalog of ultracool dwarfs in Pan-STARRS1 contains photometry and proper motions from PS1 for 9888 M, L, and T dwarfs, along with photometry from 2MASS, AllWISE, and *Gaia* DR1 whenever available. The catalog includes all published L and T dwarfs as of 2015 December with photometry in at least one of the five PS1 bands ($g_{P1}r_{P1}i_{P1}z_{P1}y_{P1}$). The catalog does not contain all known M dwarfs, but does include a large sample in order to accurately represent the colors and kinematics of M dwarfs in PS1.

We describe the construction of our catalog in Section 2.1. In Sections 2.2 and 2.3, we provide more details about our selection of L+T and M dwarfs, respectively. In Section 2.4, we discuss the spectral types used in our catalog. We describe our identification of young objects in Section 2.5 and our treatment of binaries in Section 2.6. In Section 2.7 we assess the completeness of our catalog.

2.1. Construction

To create our catalog, we compiled a list of late-M, L and T dwarfs from DwarfArchives¹, M dwarfs from [West et al. \(2008\)](#), and numerous literature sources from 2012–2017. We included positions, proper motions, spectral types, and photometry from 2MASS ([Cutri et al. 2003](#)), AllWISE ([Cutri et al. 2014](#)), and *Gaia* DR1 ([Lindegren et al. 2016](#)) when available. We also tracked objects identified as binaries and those with spectroscopic or other indications of youth. The catalog includes new discoveries through 2015 December and a handful of updates to photometry, astrometry, and spectral types from 2016 and 2017.

In order to ensure that every object in our catalog is a bona fide M, L, or T dwarf, we included only published objects with spectroscopic classification. We have therefore excluded objects with only photometric spectral types (e.g., based on optical or near-infrared colors or methane imaging). Our catalog also does not include close substellar companions to main sequence stars detected by high-angular resolution imaging and/or radial velocity because these objects are not resolved by PS1.

We cross-matched our list with the full PS1 Processing Version 3.3 database (PV3.3, 2017 March) by position using a 3" matching radius, retaining the closest object matched in PS1. PV3.3 includes an update to the 2016 December public data release (PS1 DR1) that reduced the astrometric errors but did not affect photometry ([Magnier et al. 2017](#)). In order to maximize the number of accurate matches, we used PS1 positions published in the literature (from earlier processing versions) or AllWISE positions (nearly contemporaneous with PS1) whenever possible for the objects in our list. If neither of those were available, we used the most recent positions reported in the literature; frequently these came from 2MASS, SDSS, or UKIDSS. When these objects had reported proper motions, we used the proper motions to project expected PS1 coordinates and adopted those for our cross-match.

To ensure that our catalog contains only secure PS1 measurements of real astrophysical objects, we applied photometric quality cuts described in detail in Section 3.1.1. Briefly, we required our PS1 matches to have photometric errors less than 0.2 mag in at least one PS1 band, with detections at two or more epochs in that band, and we excluded objects likely to be saturated in all bands. In addition, we excluded any sources flagged as having poor PSF fits ($\text{psf_qf} < 0.85$), and we verified that none of our PS1 matches were marked as quasars, transients, periodic variables, or solar system objects. Any object without a PS1 match within 3" of the expected coordinates was removed from our catalog.

To check for incorrect matches, we calculated colors using the 2MASS, AllWISE, and PS1 photometry for our matches (Section 3.4). We sorted our list into bins of one spectral sub-type, and inspected every object with a $g_{P1} - y_{P1}$, $r_{P1} - i_{P1}$, $r_{P1} - z_{P1}$, $r_{P1} - y_{P1}$, $i_{P1} - z_{P1}$, $i_{P1} - y_{P1}$, $z_{P1} - y_{P1}$, $y_{P1} - J_{2MASS}$, or $y_{P1} - W1$ color differing from the mean for its spectral type by more than 3 times the rms color for that spectral type bin. We also inspected every T dwarf with a reported g_{P1} , r_{P1} , or i_{P1} detection. In addition, since the cool temperatures of M, L, and T dwarfs

¹ Hosted at <http://DwarfArchives.org>. Last updated 2013-05-29.

necessitate reddish PS1 (optical) colors, we inspected all objects having a secure detection in a bluer band but not in a redder band (e.g., some nearby M dwarfs were saturated in i_{P1} , z_{P1} , and y_{P1} , but not in g_{P1} or r_{P1}). To inspect an object, we examined stacked images from PS1, 2MASS, and AllWISE, and searched in all three surveys within a 60" radius around the PS1 position for other possible matches. We discarded PS1 matches for which an image artifact, a nearby brighter star, or a blue or extended background object had clearly contaminated the detection (i.e., the source of contamination lay within the visible PSF of the object from our list). In cases where contamination affected some but not all of the PS1 bands, we retained the object in our catalog and rejected photometry only from the contaminated bands. (All g_{P1} and r_{P1} detections of T dwarfs were discarded in this manner.) We corrected a match when the images and colors clearly pointed to a different PS1 source, but we did not make corrections in ambiguous cases in order to minimize rejection of objects with naturally-occurring unusual photometry.

For most outliers we found nothing to indicate the object was anything other than an object with unusual colors. Many red outliers were young objects in star-forming regions and/or with low gravity spectral classifications, both associated with redder-than-typical colors for L dwarfs (e.g., Faherty et al. 2013). We discovered a few cases in which the 2MASS or AllWISE photometry was for a different nearby object, often a brighter source with which the ultracool object was blended. In the case of blends we rejected the 2MASS or AllWISE photometry; otherwise we adopted the photometry of the correct ultracool object.

2.2. L and T Dwarfs

Although ultracool dwarfs are normally brightest in the near-infrared, the depth and red-optical sensitivity of Pan-STARRS1 have allowed PS1 to detect 1617 L and T dwarfs, including spectral types as late as T9. Barring unintentional omissions, our catalog contains all spectroscopically confirmed L and T dwarfs published through 2015 December and meeting our detection standards in PS1. The L and T dwarfs in our catalog are primarily drawn from DwarfArchives and Mace (2014), supplemented by other literature sources. The final catalog includes 1265 L dwarfs and 352 T dwarfs.

2.3. M Dwarfs

M dwarfs comprise the majority of the stars in our galaxy, so a clear understanding of M dwarf properties is essential for characterizing the local stellar population and constraining models of star formation and evolution. In addition, M dwarfs provide context for the photometric and kinematic properties of L and T dwarfs, and more massive brown dwarfs younger than ~ 200 Myr will have late-M spectral types. Compiling a complete list of known M dwarfs would require an effort far beyond what is needed to accurately characterize the PS1 photometry and proper motions of the nearby field population. Instead, we built a representative sample of the field population from two sub-samples.

The first sub-sample comprises objects with well-studied and/or potentially distinctive photometry and kinematics from the recent literature, and contains 463 M6–M9 dwarfs. These objects were included in order to sample the diversity of colors and kinematics in late-M dwarfs. We included M dwarfs from the proper motion and parallax compilations of Faherty et al. (2009, 2012) and Dupuy & Liu (2012), the young object list from Allers & Liu (2013a), the young moving group members and non-members from Gagné et al. (2015c), the catalog of SpeX spectra from Bardalez Gagliuffi et al. (2014), and wide ultracool companions to main sequence stars from Deacon et al. (2014).

The second sub-sample is a large set of M dwarfs with high-quality photometry, representative of the generic field population. We cross-matched all M0–M9 dwarfs listed in the catalog of West et al. (2008) with PS1, 2MASS, and AllWISE using a matching radius of 5". We required sources to have photometric errors < 0.05 mag in at least five of the eight total PS1 and 2MASS bands (*grizyJHK*), and at least two detections in individual exposures in each PS1 band. To avoid saturated objects, we rejected any sources brighter than the limits listed in Section 3.1.2 or flagged by PS1 for poor PSF fits ($\text{psf_qf} < 0.85$). We then removed objects with non-zero confusion, saturation, extendedness, or de-blending flags in either 2MASS or AllWISE. These cuts are more stringent than for the late-M, L and T dwarfs in our catalog in order to ensure a very clean field M dwarf sample with high-quality photometry. This sub-sample contains 7808 M dwarfs from West et al. (2008), bringing the total for M dwarfs in our catalog to 8271.

2.4. Spectral Types

For the objects in our catalog, we use spectral types from the literature. These spectral types were determined by a variety of methods, based on visual or numerical analysis of red-optical ($\approx 0.65 - 1 \mu\text{m}$) or near-infrared ($\approx 1 - 2.5 \mu\text{m}$) spectra. In cases where an object has both an optical and a near-IR spectral type, we adopt the optical type for M and L dwarfs and the near-IR type for T dwarfs. The spectral types for the M dwarfs drawn from West et al. (2008) were all derived from optical spectra.

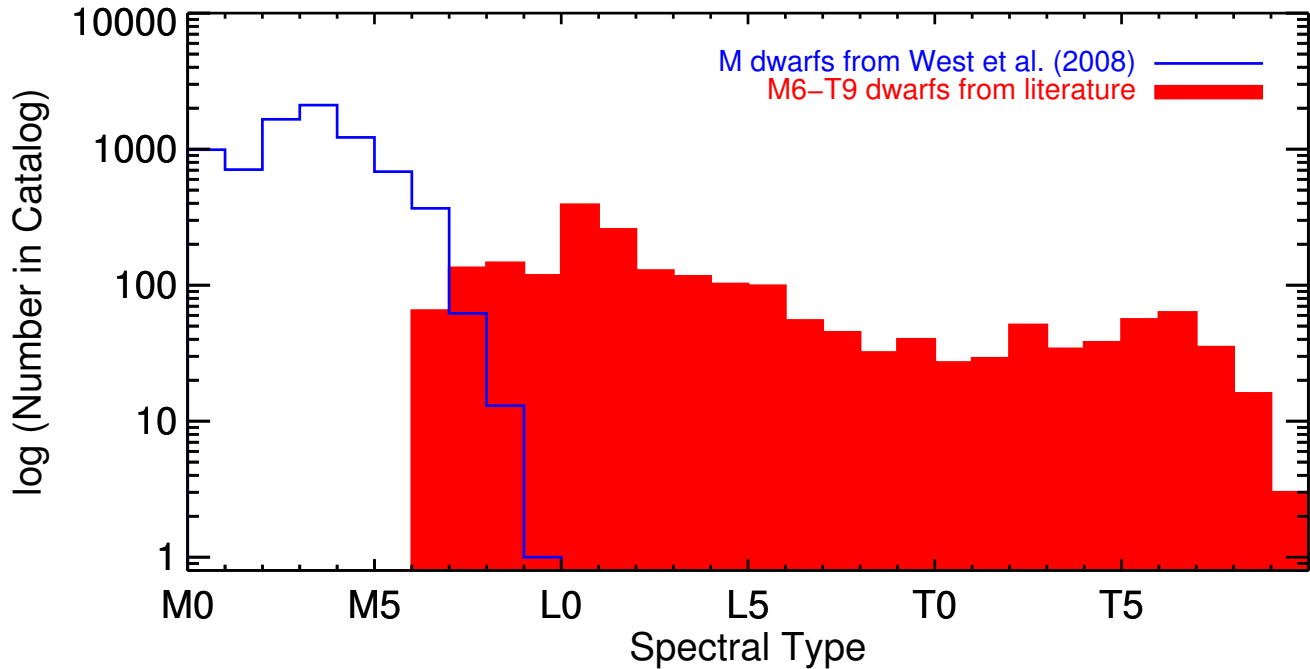


Figure 1. The distribution of spectral types in our catalog. The late-M, L and T dwarfs compiled from the literature are shown in solid red, while the M dwarfs from [West et al. \(2008\)](#) are shown with a blue outline. The catalog robustly samples the temperature range of all but the coolest brown dwarfs, and includes objects with spectral types as late as T9.

There are seven objects in our catalog with an optical L type and a near-IR T type. For these we use the T spectral type (all T0–T1). All seven objects show clear methane absorption at $1.6 \mu\text{m}$ and/or $2.2 \mu\text{m}$ in their near-IR spectra, a hallmark of T dwarfs. We note that these objects are all confirmed binaries (by high-resolution imaging) or candidate binaries (based on peculiar spectra) with components spanning the L/T transition. The spectral types are therefore based on unresolved spectral blends, explaining the disagreement between the optical and near-IR types.

We show the distribution of all spectral types in our catalog in [Figure 1](#). The earliest type in our catalog is M0 (by construction), and the latest spectral type detected by PS1 is T9. Our catalog contains more than 20 objects of each spectral sub-type through T7, robustly sampling the ultracool dwarf population for all but the coolest objects. We compare the distribution of L and T dwarfs in our catalog to all L and T dwarfs in the PS1 field (north of $\delta = -30^\circ$) in [Figure 2](#). The known objects not present in our catalog are mostly later-T dwarfs too faint to be detected by PS1. These have chiefly been discovered by deeper near-IR searches over narrower fields (e.g., [Albert et al. 2011](#); [Burningham et al. 2013](#)) or by searches for late-T and Y dwarfs using *WISE* (e.g., [Kirkpatrick et al. 2011](#)). The ≈ 30 L dwarfs not detected by PS1 are mostly unresolved companions to higher-mass stars or discoveries from deep imaging of star-forming regions.

2.5. Young Objects

Our catalog includes many young objects (ages $\lesssim 200$ Myr), which are known to have distinctive colors and kinematics (e.g., [Kirkpatrick et al. 2008](#); [Faherty et al. 2009](#)). We identify young objects primarily by low-gravity classifications reported in the literature: β , γ , and δ classes based on optical ([Kirkpatrick 2005](#); [Cruz et al. 2009](#)) or near-IR ([Gagné et al. 2015c](#)) spectra, and INT-G and VL-G based on near-IR spectra ([Allers & Liu 2013a](#)). We also identify any object in a star-forming region as young. In addition, we include objects in our young sample that lack formal low-gravity classifications but have other evidence for youth: NLTT 13728, LP 423-31, and 2MASS J19303829–1335083 ([Shkolnik et al. 2009](#)), LSPM J1314+1320 ([Schlieder et al. 2014](#)), 2MASS J17081563+2557474 ([Kellogg et al. 2015](#)), and 2MASS J22344161+4041387 ([Allers et al. 2009](#)) show spectroscopic signs of low gravity; SDSSp J111010.01+011613.1 ([Gagné et al. 2015a](#)) and WISEA J114724.10–204021.3 ([Schneider et al. 2016b](#)) are members of young moving groups; and LP 261-75B ([Reid & Walkowicz 2006](#)) and Gl 417BC ([Kirkpatrick et al. 2001a](#)) are wide companions to young stars.

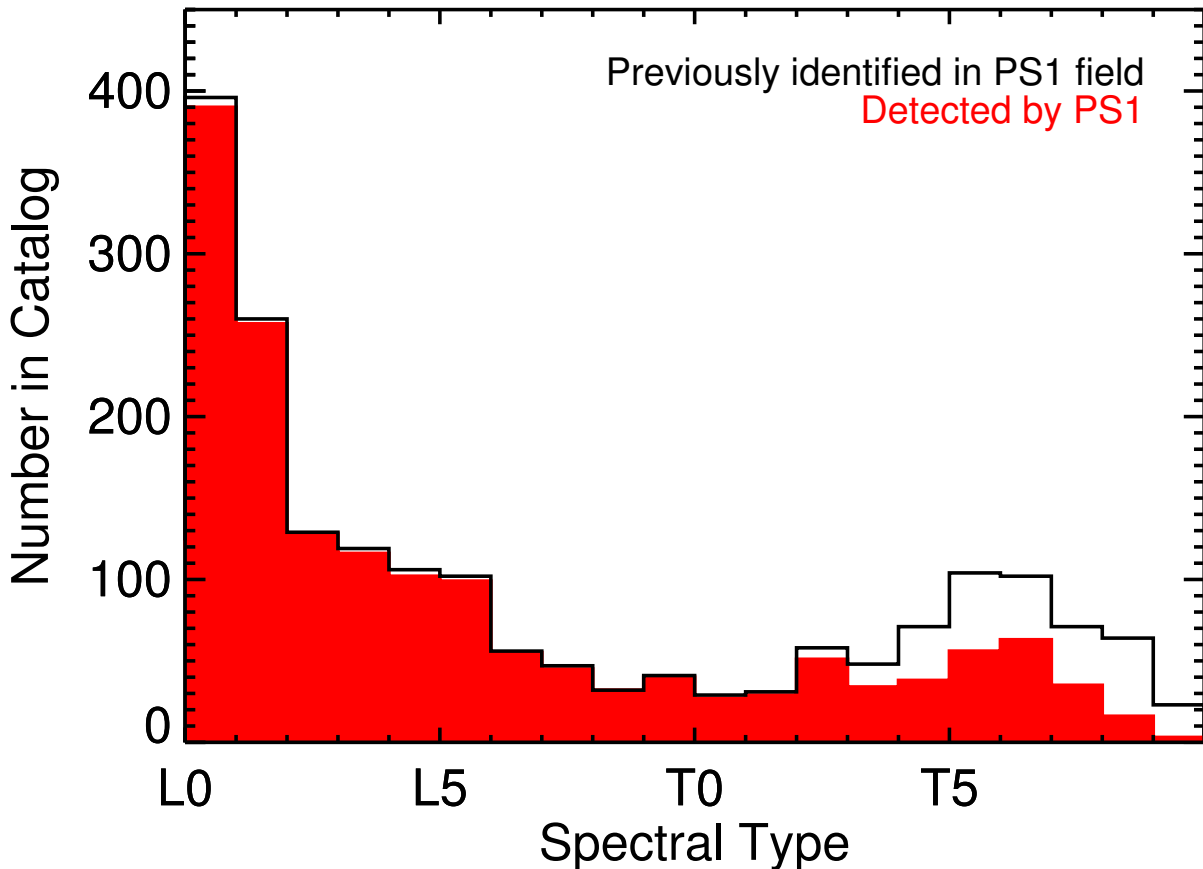


Figure 2. The distribution of L and T spectral types in our catalog, compared to previously identified L and T dwarfs in the PS1 field. PS1 has detected nearly all previously-known L dwarfs; the handful of non-detections are mostly faint objects in star-forming regions or unresolved companions to higher-mass stars. The T dwarfs (mostly later-type) not detected by PS1 have primarily been discovered by deeper near-IR searches over narrower fields or in the mid-IR using the *WISE* survey.

2.6. Binaries

Our catalog naturally includes ultracool binaries with separations wide enough to be resolved in PS1, as well as many that are unresolved. In our catalog, we assigned the term “binary” only to pairs that are unresolved in PS1 but confirmed by high-resolution imaging or radial velocity measurements. We treat these as single objects, reporting their blended photometry. We note that peculiar spectral features have been used to identify candidate unresolved binaries (Burgasser et al. 2010a; Bardalez Gagliuffi et al. 2014), but this technique has not been demonstrated to robustly distinguish actual blends from single objects with unusual atmospheric properties. Given our conservative approach, we expect our catalog to contain some unidentified binaries. Our catalog identifies a total of 81 unresolved binaries and two unresolved triple systems among the 2080 late-M, L, and T dwarfs from the literature. This binary fraction of only 4% is less than the $\approx 20\%$ estimated by population studies (e.g., Marocco et al. 2015), implying that our catalog indeed contains unrecognized binaries. This is not surprising given that many ultracool dwarfs have not yet been targeted with high-resolution imaging.

The $\approx 1''.1$ angular resolution of PS1 allows it to resolve binaries that were not resolved in either 2MASS ($\approx 2''.5$ Skrutskie et al. 2006) or AllWISE ($\approx 6''$ for the W1 and W2 bands Wright et al. 2010). However, the literature contains fewer than twenty binaries with separations wider than $1''$ for which both components are ultracool dwarfs. Most of these binaries do not appear in our catalog because they are too far south for PS1 ($\delta < -30^\circ$) or because both components are M dwarfs (for which our catalog is not complete). Our catalog contains a single instance of a binary resolved in PS1 and 2MASS, but not in AllWISE: UScoCTIO 108 and UScoCTIO 108b (Béjar et al. 2008). For this

pair, we report the AllWISE photometry (blended) only for the primary (treating it as an unresolved binary), and no AllWISE photometry for the secondary.

Our catalog also contains three ultracool binaries that are resolved in PS1, 2MASS, and AllWISE. We report the photometry and proper motion for each component individually. One pair, LP 704-48 and SDSS J000649.16–085246.3 (itself an unresolved binary), is well-separated at $27''.4$ (Burgasser et al. 2012). Another pair, the blue L6 dwarf SDSS J141624.08+134826.7 and the T7.5 dwarf ULAS J141623.94+134836.3, has a separation of $9''$ (Burningham et al. 2010b) and is well resolved in PS1. ULAS J141623.94+134836.3 was not detected in 2MASS despite lying well outside the PSF of the brighter L6 primary; we include synthetic 2MASS photometry from Dupuy & Liu (2012) in our catalog. ULAS J141623.94+134836.3 appears barely resolved in AllWISE images, and we include pipeline-deblended AllWISE photometry for each component in our catalog. Finally, VHS J125601.92–125723.9AB (also an unresolved binary; Stone et al. 2016) and its companion VHS J125601.92-125723.9 b (separation $8''.1$; Gauza et al. 2015) are well-resolved in both PS1 and 2MASS. They appear partially resolved in AllWISE images. We include in our catalog the deblended photometry from AllWISE for the primary and the decontaminated photometry for the wide companion (removing a diffraction spike) from Gauza et al. (2015).

We also note two previously known binaries in our catalog with separations $\approx 1''$ that appear resolved in PS1 images, but are each represented by only a single object in the PS1 database: DENIS-P J220002.05–303832.9 and 2MASS J17072343–0558249. These cases result from the algorithm by which the PS1 database assembles multiple detections over the four years of PS1 observations into individual objects (see Section 4.1.3 and Magnier et al. 2017 for more details). Close binaries may be combined into a single object in the database, especially if the binary’s proper motion over the PS1 survey period is comparable in amplitude and direction to the binary’s separation. We have not attempted to de-blend these objects in our catalog, and we mark both as binaries (unresolved) in our catalog. More $\approx 1''$ binaries such as these are sure to appear in the PS1 database as single objects; we describe our discovery of one such binary in Section 5.

2.7. Completeness

Our catalog is a combination of discoveries from many searches for M, L, and T dwarfs, conducted using a variety of methods and therefore containing a variety of biases. Our selection of a representative sample of M dwarfs means that our catalog will be far from complete for this spectral type, especially for types M0–M5 for which our photometric quality cuts include only bright objects. While we have included all previously identified L and T dwarfs observed by PS1, there are some L and T dwarfs beyond the detection limit or angular resolution of PS1 (Figure 2), and there are sure to be undiscovered objects remaining in the PS1 field.

We assess the completeness of our catalog for spectral types M6–T9 by examining the number of objects as a function of distance, shown in Figure 3. We use trigonometric parallax distances when available from the literature. For the remaining objects we use photometric distances calculated from $W2$ magnitudes and the spectral type-absolute magnitude polynomial from Dupuy & Liu (2012). Photometric distances for unresolved binaries will be systematically too small, so we exclude known binaries from our assessment. Figure 3 also compares the cumulative distributions of late-M, L, and T dwarf distances to distributions from a simple Galactic thin disk model for space density $\rho = \rho_0 \exp[-Z/H_0]$, where ρ_0 is the space density at the Galactic plane, Z is the distance from the plane and $H_0 = 300$ pc is the scale height (Bochanski et al. 2010). We integrate this model over the PS1 survey area to account for varying lines of sight relative to the galactic plane. We normalize this model distribution with the cumulative numbers of known late-M, L, and T dwarfs at 10 pc. The numbers of objects begin to deviate from our model distributions at ≈ 10 pc for late-M and T dwarfs and ≈ 20 pc for L dwarfs, implying that our catalog is not volume-complete beyond these distances.

3. PHOTOMETRY

We present the PS1, 2MASS, and AllWISE photometry for our catalog in Table 1. PS1 photometry is on the AB magnitude scale (Tonry et al. 2012), calibrated using the procedures outlined in Schlafly et al. (2012) and Magnier et al. (2013). 2MASS, AllWISE, and *Gaia* photometry are calibrated on the Vega magnitude scale (Cohen et al. 2003; Wright et al. 2010; Carrasco et al. 2016, respectively).

The full table contains 51 columns, and is available for download in electronic form from the online journal. Table 1 is arranged in two parts: (1) the late-M, L, and T dwarfs compiled from the literature, followed by (2) the M dwarfs from West et al. (2008). For reference, Table 1 includes spectral types (with notation for subdwarfs), and indicates whether an object has been classified as a low-gravity object based on its optical or near-IR spectrum, identified as a young object (due to low gravity or other reasons), or confirmed as a binary. Table 2 shows a sample of the rows and columns of Table 1 for guidance regarding format and content.

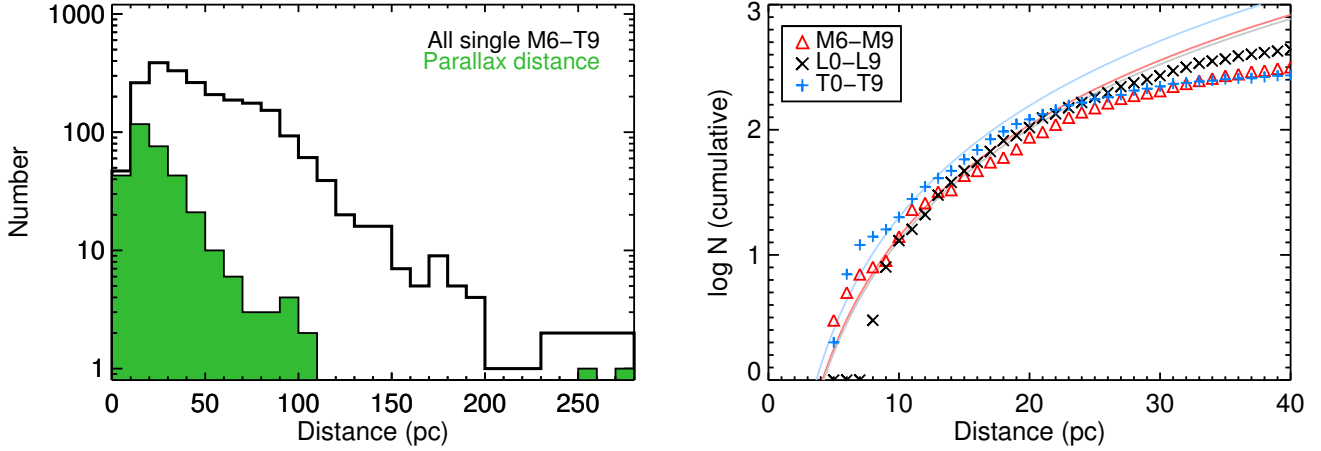


Figure 3. *Left:* Distribution of the distances of single M6–T9 dwarfs in our catalog (black outline). Where available, we use a parallax distance from the literature (solid green). For other objects we use $W2$ -based photometric distances. *Right:* Cumulative distribution of these distances for M (red triangles), L (black \times), and T (blue $+$) dwarfs, using a format similar to Figure 5 in Faherty et al. (2009). The curves indicate density distributions from a simple Galactic thin disk model with a scale height of 300 pc, normalized at 10 pc. We use light red, grey, and blue curves for M, L, and T dwarfs, respectively. Our catalog is not consistent with the expected density distribution beyond 10 pc for late-M and T dwarfs and 20 pc for L dwarfs, implying that our catalog is incomplete beyond these distances.

Table 1. Photometry of M, L, and T Dwarfs in the Pan-STARRS1 3π Survey

Column	Label	Description
1	Name	Name used in the object’s discovery or spectral confirmation paper
2	Spectral Type: Opt	Optical spectral type ^{a,b}
3	Spectral Type: NIR	Near-infrared spectral type ^{a,b}
4	Spectral Type: Adopted	Adopted spectral type ^{a,b}
5	Gravity: Opt	Low-gravity classification from an optical spectrum ^b
6	Gravity: NIR	Low-gravity classification from a near-infrared spectrum ^b
7	Binary	”Y” or ”triple” for known binary or triple systems not resolved in PS1
8	Young	”Y” for known young objects ^c
9	Pan-STARRS1 Name	PS1 Designation ^d , rrr.rrrr+dd.dddd (J2000)
10	g_{P1}	PS1 g magnitude
11	$err_{g_{P1}}$	Error in PS1 g magnitude
12	N_g	Number of measurements used in the g_{P1} photometry
13	S_g	Source of the g_{P1} photometry: chip (C), recalculated chip ^e (R), or forced warp (W)
14	r_{P1}	PS1 r magnitude
15	$err_{r_{P1}}$	Error in PS1 r magnitude
16	N_r	Number of measurements used in the r_{P1} photometry
17	S_r	Source of the r_{P1} photometry: chip (C), recalculated chip ^e (R), or forced warp (W)
18	i_{P1}	PS1 i magnitude
19	$err_{i_{P1}}$	Error in PS1 i magnitude
20	N_i	Number of measurements used in the i_{P1} photometry
21	S_i	Source of the i_{P1} photometry: chip (C), recalculated chip ^e (R), or forced warp (W)
22	z_{P1}	PS1 z magnitude
23	$err_{z_{P1}}$	Error in PS1 z magnitude
24	N_z	Number of measurements used in the z_{P1} photometry
25	S_z	Source of the z_{P1} photometry: chip (C), recalculated chip ^e (R), or forced warp (W)
26	y_{P1}	PS1 y magnitude
27	$err_{y_{P1}}$	Error in PS1 y magnitude

Table 1 continued on next page

Table 1 (*continued*)

Column	Label	Description
28	N_y	Number of measurements used in the y_{P1} photometry
29	S_y	Source of the y_{P1} photometry: chip (C), recalculated chip ^e (R), or forced warp (W)
30	2MASS Name	2MASS catalog designation
31	J	J magnitude or upper limit (2MASS)
32	err $_J$	Error in J magnitude
33	H	H magnitude or upper limit (2MASS)
34	err $_H$	Error in H magnitude
35	K_S	K_S magnitude or upper limit (2MASS)
36	err $_{K_S}$	Error in K_S magnitude
37	2MASS Clfg	2MASS contamination and confusion flags: three-character string corresponding to JHK bands.
38	AllWISE Name	AllWISE catalog designation
39	$W1$	$W1$ magnitude or upper limit (AllWISE)
40	err $_{W1}$	Error in $W1$ magnitude
41	$W2$	$W2$ magnitude or upper limit (AllWISE)
42	err $_{W2}$	Error in $W2$ magnitude
43	$W3$	$W3$ magnitude or upper limit (AllWISE)
44	err $_{W3}$	Error in $W3$ magnitude
45	$W4$	$W4$ magnitude or upper limit (AllWISE)
46	err $_{W4}$	Error in $W4$ magnitude
47	AllWISE cc.flags	AllWISE contamination and confusion flags: four-character string corresponding to W1W2W3W4 bands.
48	AllWISE neighbor	Number of other AllWISE objects detected within 8'' of the AllWISE position.
49	G	<i>Gaia</i> DR1 G magnitude
50	err $_G$	Error in <i>Gaia</i> DR1 G magnitude
51	References	References: Discovery, Spectral Type, Gravity, Binarity, 2MASS photometry, AllWISE photometry

^a Spectral types taken from the literature (Section 2.4). When both optical and near-IR types are available, we adopt the optical type for M and L dwarfs and the near-IR type for T dwarfs. Most spectral types have an uncertainty of ± 0.5 subtypes; “:” = ± 1 subtype; “::” = ± 2 or more subtypes. “sd” = subdwarf; “esd” = extreme subdwarf (Gizis 1997).

^b β , γ , and δ indicate classes of increasingly low gravity based on optical (Kirkpatrick 2005; Cruz et al. 2009) or near-infrared (Gagné et al. 2015c) spectra. FLD-G indicates near-infrared spectral signatures of field-age gravity, INT-G indicates intermediate gravity, and VL-G indicates very low gravity (Allers & Liu 2013a).

^c Young objects identified by low-gravity classifications or other spectroscopic evidence for youth, membership in star-forming regions or young moving groups, or companionship to a young star (Section 2.5).

^d Pan-STARRS names are from the 3π Survey, Processing Version 3.3 (PV3.3). Photometry listed here is from PV3.3 and supersedes values in previous publications.

^e Chip photometry recalculated by combining the measurements for an object that is split into two or more “partial objects” in PS1 (Sections 3.1.4 and 4.1.3).

^f Although classified as FLD-G, the spectrum shows hints of intermediate gravity (as described in Aller et al. 2016).

^g Photometry rejected for this band after visual inspection of stack images found no detection at the PS1 coordinates.

^h Photometry rejected for this band after visual inspection of stack images found obvious contamination by a background object.

ⁱ Photometry rejected for this band after visual inspection of stack images found an image processing artifact at the PS1 coordinates.

^j Photometry rejected for this band after visual inspection of stack images found obvious contamination from a nearby bright star.

^k UScoCTIO 108 and UScoCTIO 108b (Béjar et al. 2008) are not resolved in AllWISE. For this binary, we report AllWISE photometry (blended) only for the primary, and no AllWISE photometry for the secondary.

NOTE—This table is available in its entirety in machine-readable form in the online journal. A sample of the rows and columns is shown in Table 2.

3.1. PS1 Photometry

3.1.1. Chip and Forced Warp Photometry

Our catalog uses two types of PSF photometry from the PS1 database, known as “chip” and “forced warp.” These types are described in detail in Magnier et al. (2017), and we explain them briefly here.

During PS1 data processing, each raw image was individually detrended and calibrated to create a “chip” image, and each detected object on a chip was fitted with a PSF model to determine its photometry and astrometry. The chip pixels were geometrically transformed onto a grid with uniform $0.25'' \text{ pixel}^{-1}$ scale representing pre-defined sky coordinates (R.A. and Decl.), creating “warp” images. The warps for each filter matching the same portions of the sky were then summed together, forming “stack” images. Detections in the warps and stacks were again fit with PSFs to measure photometry and astrometry.

Chip photometry is the mean measurement from all chips in which an object was detected, and is likely to be the most accurate photometry for a well-detected object due to the individual calibration of each chip. Stack photometry is measured from the single fit to a stack detection. Stack photometry will generally be less accurate because individual images forming a stack were taken in varying conditions and at different locations on the Pan-STARRS1 detector, creating poorly-defined PSFs. However, the stacks can identify objects too faint to be detected in individual images, as long as the objects do not move significantly over the 4-year time baseline of the survey. To take advantage of the greater depth of the stacks without sacrificing too much of the calibration of the chip images, the PS1 data pipeline fit a model PSF on every warp image at the location of each object detected in a stack. The warp photometry reported by PS1 is the mean of the fluxes from the forced PSF fits at a given location, excluding cases where the warp pixels were excessively masked. Warp photometry will not have the full accuracy of the chip measurements, but achieves the depth of the stack photometry with more accuracy than the stack image alone. Warp photometry is therefore most useful, at least in theory, for slow-moving objects with magnitudes comparable to or fainter than the chip detection limit.

Table 3. Flux overestimation bias thresholds for PS1 chip photometry

Band	Threshold (mag)
g_{P1}	21.0
r_{P1}	21.0
i_{P1}	20.5
z_{P1}	20.0
y_{P1}	19.0

NOTE—PS1 chip magnitudes fainter than these thresholds may be significantly affected by flux overestimation bias. For slow-moving objects ($<100 \text{ mas yr}^{-1}$), warp photometry is more likely to be accurate.

To quantify where PS1 chip and warp photometry differ significantly, we examined the photometry of a large sample of well-detected objects in PS1 chip images. For each of the five PS1 bands, we extracted the chip and warp magnitudes for all objects having at least three chip detections in a 4 deg^2 patch of sky (centered at $\alpha = 80^\circ$, $\delta = 5^\circ$) at moderate galactic latitude ($\approx -18^\circ$) and away from regions of significant reddening. This gave us a sample of more than 60,000 objects in each band, $\gtrsim 99\%$ having proper motions less than 100 mas yr^{-1} . Figure 4 plots the differences between y_{P1} chip and warp magnitudes for each object, normalized by the quadrature sum of the chip and warp errors, as a function of magnitude. For brighter unsaturated objects ($y_{P1} \approx 13 - 19 \text{ mag}$), the difference between chip and warp magnitudes is nearly always less than 2σ . For objects fainter than $y_{P1} \approx 19 \text{ mag}$, however, the chip photometry becomes significantly brighter for many objects, due to a flux overestimation bias for objects near the chip detection threshold. This well-known bias is discussed in depth in the context of 2MASS in Cutri et al. (2006) and Kellogg et al. (2015), and is important for detections with $S/N \lesssim 10$. Briefly, since the chips have brighter detection limits than the warps, mean chip photometry may not include the fainter measurements that are present in the warp photometry. For example, an object near the chip detection limit may have 10 forced warp measurements but only 3 chip detections due to noise at the detection threshold. Those chip detections will be the 3 brightest measurements of the object, so the mean chip magnitude will be brighter than the mean warp magnitude. Warp photometry is therefore more likely to be accurate for faint objects near the chip detection limits in each band. We list the magnitudes at which the flux overestimation bias becomes significant for chip photometry in each PS1 band in Table 3, based on visual inspection of Figure 4 and analogous plots for the other PS1 bands. We note that for even fainter objects, flux overestimation bias will also impact the warp photometry, but for those objects there is no deeper PS1 photometry available.

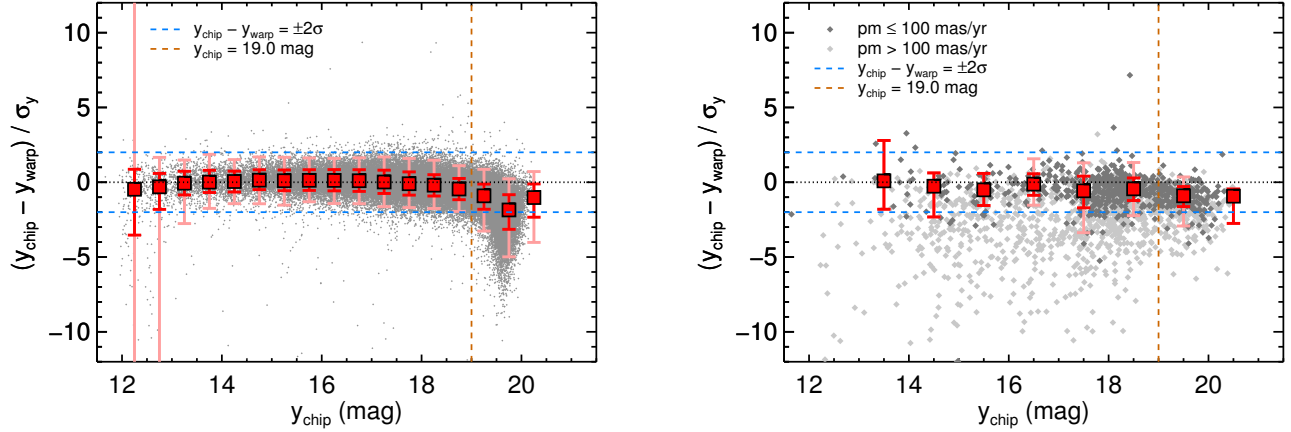


Figure 4. *Left:* Differences in y_{P1} chip and warp mean magnitudes (gray dots) for objects in an arbitrary 4 deg^2 patch of sky, normalized by the uncertainties. $>99\%$ of these objects have proper motions less than 100 mas yr^{-1} . The red boxes show the median differences for objects in bins of 0.5 mag ; the dark and light red error bars indicate 68% and 95% confidence limits, respectively. For reference, the blue dashed lines mark $y_{\text{chip}} - y_{\text{warp}}$ differences of $\pm 2\sigma$, and the dotted black line indicates no difference. For objects of moderate brightness, the differences between chip and warp magnitudes are nearly always less than 2σ significance. At the bright end, saturation causes significant scatter in magnitudes. At the faint end, many chip magnitudes become significantly brighter due to flux overestimation bias. The vertical brown dashed line at $y = 19 \text{ mag}$ marks the onset of this bias. *Right:* The same plot for objects from our ultracool catalog. Those having proper motions less than 100 mas yr^{-1} are plotted in dark grey, with faster moving objects in light grey. The red boxes indicate the median $y_{\text{chip}} - y_{\text{warp}}$ differences only for the slower ($\mu \leq 100 \text{ mas yr}^{-1}$) objects. Warp photometry is significantly fainter than chip photometry for most of the faster moving objects because an object is not at the same force-fit position in all warps. We use chip photometry in our catalog as our default, but use warp photometry for objects with $y_{\text{chip}} > 19.0 \text{ mag}$ and proper motion $< 100 \text{ mas yr}^{-1}$. Analogous plots for the other four PS1 bands show similar results.

Objects that moved significantly over the four years of PS1 observations will be smeared on the stack images. This smearing will also impact the warp photometry, because the warp PSF fits are applied at the same location on each warp but a moving object will not be centered at that location in every warp. To assess the impact of proper motion on warp photometry, we examined the difference between chip and warp magnitudes for objects brighter than the faint thresholds in Table 3, sorted into bins of PS1-measured proper motion. We determined that nearly all objects for which chip and warp photometry are $>2\sigma$ different have proper motions exceeding 100 mas yr^{-1} (Figure 4), so we do not use warp photometry for objects moving faster than 100 mas yr^{-1} .

3.1.2. PS1 Photometry Reported in Our Catalog

For each object and PS1 band ($g_{P1}r_{P1}i_{P1}z_{P1}y_{P1}$) in our catalog, we report a single magnitude, either chip or warp. By default, we use the chip photometry for objects with chip errors $< 0.2 \text{ mag}$ and detected in at least two chip exposures. We use the warp photometry only in specific cases, when either:

1. Chip photometry is fainter than the thresholds listed in Table 3, to avoid flux overestimation bias in the chip photometry.
2. Chip photometry is either not measured or of insufficient quality (i.e., fewer than two detections or error $\geq 0.2 \text{ mag}$).

However, since warp photometry degrades for faster-moving objects, we only use warp photometry when both of the following are true:

1. A proper motion of $\mu > 100 \text{ mas yr}^{-1}$ with $\frac{\mu}{\sigma_\mu} > 3$ has not been measured in PS1 or the literature, to avoid fast-moving objects.
2. A proper motion with $\mu - \sigma_\mu > 100 \text{ mas yr}^{-1}$ has not been measured in PS1 or the literature, to avoid most fast-moving objects with poorly-measured proper motions.

Finally, we only use warp photometry with errors $< 0.2 \text{ mag}$ and calculated from at least two successful warp fits, the same standards we use for chip photometry.

On the bright end, we rejected any photometry with $g_{P1} < 14.5$ mag, $r_{P1} < 14.5$ mag, $i_{P1} < 14.5$ mag, $z_{P1} < 13.5$ mag, or $y_{P1} < 12.5$ mag to avoid saturation.

For many objects in our catalog we use chip photometry for some bands and warp for others, depending on the values and quality of the chip photometry. If neither the chip nor the warp photometry meet or quality standards in a given band, we report no photometry for that band. Objects with no chip or warp photometry of sufficient quality in any of the five PS1 bands do not appear in our catalog.

The photometric errors reported in the PS1 database are formal errors that do not include systematics. Given the sensitivity of the Pan-STARRS1 camera and the multiple epochs of photometry, these formal errors can be very small, less than 0.0005 mag in some cases. A full assessment of the systematic errors for PV3.3 has not yet been completed, but a calibration of the first 1.5 years of PS1 photometry performed by [Schlafly et al. \(2012\)](#) found per-image zeropoints had rms scatter ≈ 10 mmag in all five PS1 filters, so we adopt this value (0.01 mag) as a floor for our catalog.

3.1.3. *False Warp Detections of Faint Objects*

While inspecting the PS1 colors of our catalog objects, we discovered a few dozen instances where very faint objects near the stack detection limit (e.g., $g_{P1} \gtrsim 23$ mag) had warp photometry with implausibly small errors (as small as 0.01 mag) despite only two or three warps contributing to the mean photometry. In particular, we found T dwarfs with high-S/N warp photometry reported for g_{P1} and r_{P1} . T dwarfs are much too faint in these visual bands to be detected by PS1. We confirmed that the g_{P1} and r_{P1} stack images showed no objects at the locations of these false detections.

We traced the source of these false high-S/N detections to the method used to calculate PS1 photometry errors. This method is described in detail in [Magnier et al. \(2017\)](#); here we give a brief summary. Each individual photometry measurement (chip, warp, or stack) includes a measurement uncertainty, which naturally is large for faint objects. Mean chip and warp magnitudes are computed using an iterative reweighting process to reject outliers, and the errors for the mean photometry are calculated by bootstrap resampling of the non-outlier measurements. Bootstrapping uses the individual measurements but not their uncertainties, instead sampling the outlier-cleaned photometry measurements to determine the error. For well-detected objects with multiple measurements, bootstrapping is demonstrated to calculate errors consistent with standard errors on the mean photometry while effectively clipping outliers such as transient image artifacts ([Magnier et al. 2017](#)). However, in cases where photometry was measured only a few times for an object, and those measurements are very similar (a statistical possibility even for objects at the detection limit), the bootstrapping process will produce a very small error, even if the individual measurements had large uncertainties. The false g_{P1} and r_{P1} warp detections in our catalog were the result of ≈ 2 – 3 low-S/N forced warp measurements of background noise that happened to find similar values, resulting in errors < 0.2 mag (from bootstrapping) on the mean warp photometry.

To identify and remove these false detections from our catalog in a systematic fashion, we extracted the individual warp flux measurements used to calculate the mean PS1 warp photometry for each object in our catalog, along with the formal uncertainties for the measurements. For each object and band, we calculated a weighted-mean warp magnitude (using inverse variance weighting) and the standard error on this weighted mean. If the reported warp error in PS1 (from bootstrapping) was less than 0.2 mag but our calculated standard error was greater than 0.2 mag, we discarded the warp photometry for that object and band. This procedure removed 12% of the PS1-reported warp measurements for the late-M, L, and T dwarfs from the literature that passed our original criteria for inclusion in the catalog (i.e., slow-moving objects with secure proper motion measurements, Section 3.1.2), affecting 255 objects in at least one band and demonstrating that false detections in the warps can be a significant source of contamination at the faint end. Specifically, we discarded 129 out of 199 measurements in g_{P1} , 123 out of 410 in r_{P1} , 27 out of 601 in i_{P1} , 19 out of 677 in r_{P1} , and 0 out of 698 in y_{P1} , consistent with the red nature of the objects in our sample (nearly all have strong y_{P1} detections). If the reported warp error in PS1 and the standard error were both less than 0.2 mag, we retained the PS1-reported photometry and error for our catalog. We used our calculated standard errors only to assess the reliability of small warp photometry errors reported by PS1, and do not include them in our catalog.

3.1.4. *Fast-Moving Objects*

As discussed in detail in Section 4.1.3, we found that objects with proper motions $\gtrsim 200$ mas yr $^{-1}$ were often split into two or more distinct “partial objects” in the PS1 database. In these cases we use the photometry from the partial object with the chip photometry in the most PS1 bands, giving preference to the redder bands if no partial object had photometry in all bands. In a few dozen cases where a chosen partial object had no photometry or photometry of insufficient quality in a PS1 band, we used photometry recalculated by combining the measurements from the partial

objects into a single object (Section 4.1.3) for that band.

3.2. 2MASS and AllWISE Photometry

Our catalog contains photometry from 2MASS and AllWISE for all objects matched to PS1 detections (Section 2.1). We include 2MASS and AllWISE photometry with nonzero contamination and confusion flags for completeness’ sake, and note that some of this potentially contaminated photometry has been used in previous studies. We include columns for the 2MASS and AllWISE contamination and confusion flags in Table 1, and refer readers to the Explanatory Supplements^{2,3} for these surveys for details.

In addition, since the large $\approx 6''$ beam of WISE makes blending with nearby objects a frequent issue, we include a column in Table 1 indicating whether each object has an AllWISE neighbor within $8''$ of the AllWISE position. The AllWISE catalog includes deblended photometry for objects with overlapping PSFs, but the deblending may not be completely successful when objects are within $8''$ of each other (Theissen et al. 2016, see their Figure 6).

While we include photometry with non-zero contamination and confusion flags and potential contamination from neighbors in our catalog, we exclude such photometry from our analysis of colors and SEDs in Section 3.4.

3.3. Gaia DR1 Photometry

To obtain *Gaia* DR1 *G*-band photometry, we cross-matched our catalog (PS1 coordinates) with *Gaia* DR1 using a $2''$ matching radius. We found matches for 7772 objects including 284 L dwarfs. As *Gaia* DR1 is preliminary and does not cover the entire PS1 survey area, we do not evaluate the DR1 *G*-band photometry for M, L, and T dwarfs here, but we include it in our catalog for reference. We rejected *Gaia* photometry for objects in our catalog for which we had identified contamination to g_{P1} , r_{P1} , or i_{P1} photometry by a bluer object (Section 2.1), but performed no other quality inspection of the *Gaia*-PS1 matches. Many *G* magnitudes have reported errors less than 0.01 mag, but as *Gaia*’s systematic photometric uncertainties are not yet fully understood (Gaia Collaboration et al. 2016a), we adopt a minimum error of 0.01 mag.

3.4. Colors and SEDs

We show multiple colors from our catalog in Figures 5–8, spanning g_{P1} through *W3*. We show 11 colors using at least one PS1 band, and four more ($(J - K_S)_{2MASS}$, $J_{2MASS} - W1$, $W1 - W2$, and $W2 - W3$) that have been used in many previous studies. To create these figures, we have extracted all objects known to be young, subdwarfs, or binaries, and used these to form a sample of “unusual” objects. The remaining objects are our “normal field” sample. Figure 5 shows colors as a function of spectral type for the normal field sample, and Figure 6 shows the same colors for the unusual sample. In Figures 7 and 8, we use the same format to show colors vs. colors for the normal field and unusual samples, respectively.

For the figures and analysis presented in this section, we only use 2MASS and AllWISE photometry with errors less than 0.2 mag, the same standard we use for PS1 photometry (Section 3.1.2). (Note that Table 1 includes 2MASS and AllWISE photometry with larger errors.) In addition, we exclude any 2MASS or AllWISE magnitude with a non-zero contamination flag, and we exclude all AllWISE magnitudes for each object having an AllWISE neighbor within $8''$ (Section 3.2).

Our catalog contains 494 L dwarfs with r_{P1} detections, including 433 in the normal field sample. With these we present the largest set of *r*-band colors of L dwarfs to date, a tenfold increase over the sample presented by Liebert & Gizis (2006) and the compilation of Koen (2013). Most PS1 colors become redder through the M dwarfs, plateau for the L dwarfs and become redder again for T dwarfs (when detected), but the L dwarfs show a different behavior with r_{P1} . $r_{P1} - i_{P1}$ features a blueward turn at spectral type $\approx M8$, becoming ≈ 0.8 mag bluer by spectral type L5 where the objects become too faint for r_{P1} detection, robustly confirming previous findings using much smaller samples (Hawley et al. 2002; Liebert & Gizis 2006). $r_{P1} - z_{P1}$ and $r_{P1} - y_{P1}$ show similar but less amplified trends. Liebert & Gizis (2006) explain these unusual blueward trends as a consequence of decreasing TiO absorption, which strongly suppresses *r*-band flux in M7-M8 dwarfs but weakens in later spectral types as Ti-bearing dust grains form. The resulting reduction in r_{P1} opacity largely cancels out the drop in flux expected from cooler objects, while the flux in i_{P1} , z_{P1} , and y_{P1} continues to decrease. In addition, K I absorption doublets centered in the i_{P1} -band (7665 Å and 7699 Å) increase in strength through the L types (Kirkpatrick et al. 1999), enhancing the trend towards bluer $r_{P1} - i_{P1}$ colors. We note that another color, $y_{P1} - W1$, also takes a blueward turn, peaking at spectral type $\approx L7$ and becoming

² http://www.ipac.caltech.edu/2mass/releases/allsky/doc/sec2_2a.html

³ http://wise2.ipac.caltech.edu/docs/release/allwise/expsup/sec2_1a.html

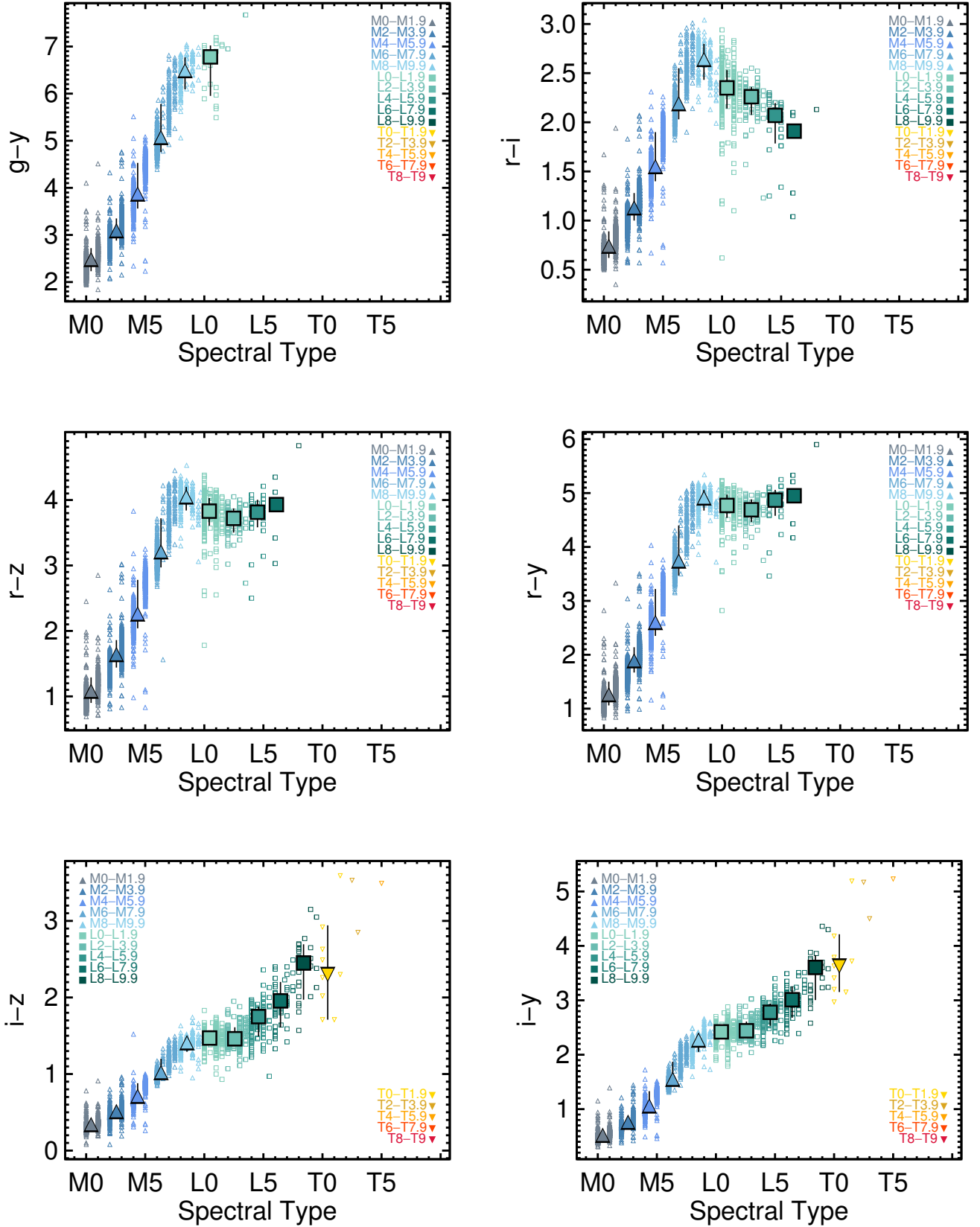


Figure 5. Color vs. spectral type plots for the M, L, and T dwarfs in our PS1-detected catalog, excluding objects known to be binaries, subdwarfs, or young. We use only photometry with errors < 0.2 mag. For objects having both optical and near-IR spectral types, we use the optical type for M and L dwarfs and the near-IR type for T dwarfs. Colors of individual objects are shown with small open symbols, while median colors and 68% confidence limits for bins of two spectral subtypes are shown with large filled symbols (see legend in each figure). Median symbols are plotted for bins with at least three objects, and confidence limits for bins with at least seven objects. Most PS1 colors plateau through the L dwarfs but become redder for T dwarfs (when detected); $r_{P1} - i_{P1}$ and $y_{P1} - W1$ are notable exceptions.

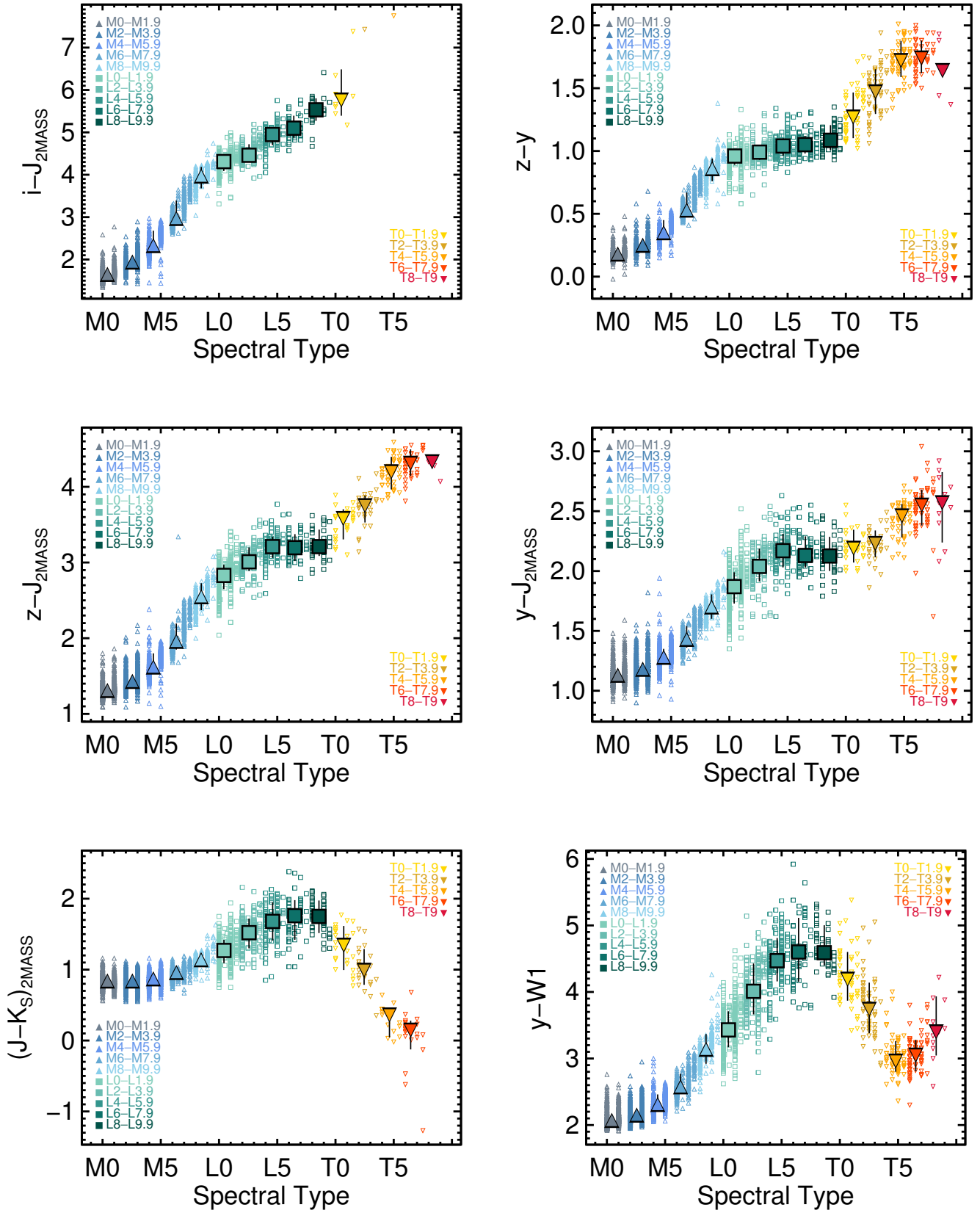


Figure 5. continued.

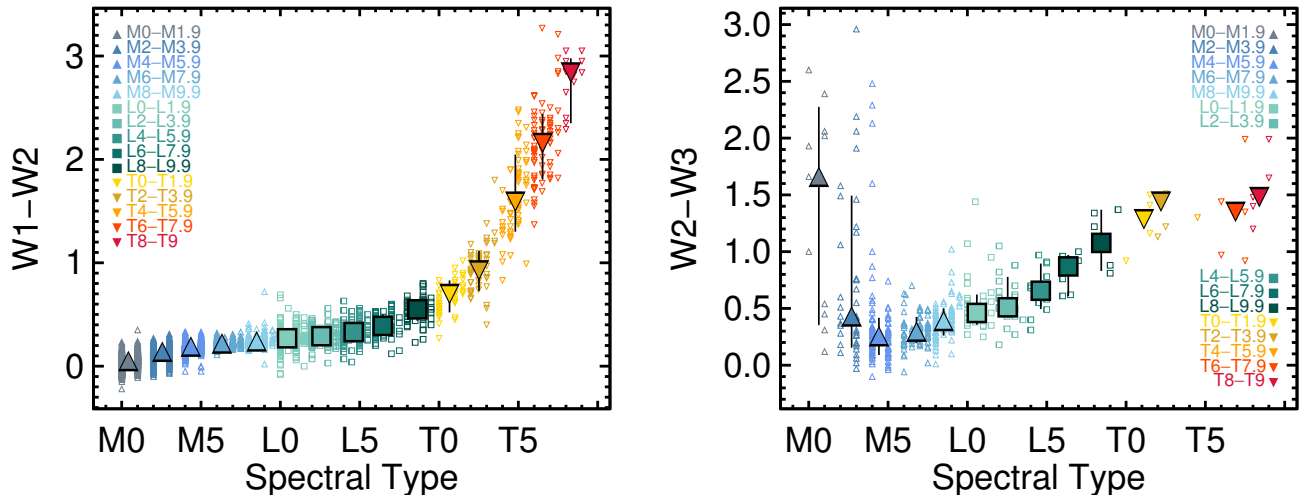


Figure 5. continued.

more than 1.5 mag bluer through spectral type T5. This trend arises from the appearance of the methane fundamental band at $3.3 \mu\text{m}$ in late-L dwarfs (Noll et al. 2000), which broadens to a deep trough spanning $3.1 - 4.0 \mu\text{m}$ by mid-T spectral types (Kirkpatrick 2005).

We also note in Figure 5 that early-M dwarfs have few detections and redder colors in $W2 - W3$. M dwarfs are relatively faint in $W3$, and the early-M dwarfs in our catalog are more distant than other spectral types, so most were not detected in $W3$. In contrast, all were detected with errors ≤ 0.05 mag in $W2$. The few early-M dwarfs that have $W3$ detections are the brightest ones in that band in our catalog, so the observed colors are redder than the overall population. The source of the $W3$ emission for the reddest objects is most likely to be debris disks or contamination from background objects, and we note that the $W2 - W3$ colors are consistent with those of other debris disks (e.g., Theissen & West 2014). We therefore do not interpret the $W2 - W3$ colors in our catalog as representative of stellar photospheres for spectral types earlier than M5.

We use the photometry from our catalog to calculate median colors of field M0–T9 dwarfs spanning ≈ 0.55 to $12 \mu\text{m}$. As with Figures 5 and 7, we have excluded all known binaries, young objects, and subdwarfs from these calculations in order to produce colors representative of the normal field population. Table 4 presents these colors in single steps of adjacent filter pairs from g_{P1} to $W3$ (excluding spectral types M0–M4 for $W2 - W3$ as explained in the preceding paragraph). Table 5 presents five additional colors previously used to study ultracool dwarfs: $i_{P1} - y_{P1}$, $i_{P1} - J_{2\text{MASS}}$, $z_{P1} - J_{2\text{MASS}}$, $(J - K_S)_{2\text{MASS}}$, and $y_{P1} - W1$. For both tables, we list the median colors and 68% confidence limits for single spectral subtypes, along with the number of objects used to determine each color.

We construct empirical spectral energy distributions (SEDs) for field ultracool dwarfs using the photometry in our catalog and parallaxes from the literature. Excluding binaries, subdwarfs, and young objects, our catalog contains 234 objects (spectral types M6–T9) with reported parallaxes and $J_{2\text{MASS}}$ photometry with no confusion or contamination flags and errors less than 0.2 mag. We calculate absolute $J_{2\text{MASS}}$ magnitudes for these objects, and determine the weighted mean and rms in bins of one spectral subtype. We then use the median colors relative to $J_{2\text{MASS}}$ from our full catalog (Table 4) to calculate absolute magnitudes for all other bands from g_{P1} to $W3$, adding the rms color for each band in quadrature with the $M_{J_{2\text{MASS}}}$ rms magnitude to determine errors. We use our catalog colors rather than directly calculating absolute magnitudes for each band because the colors are derived from a much larger and carefully vetted sample. We present our SEDs for each spectral subtype between M6 and T9 in Table 6.

Recently, Deacon et al. (2016, hereinafter D16) published empirical SEDs for the Pan-STARRS1 photometric system for spectral types B8V–M9V. Our two sets of SEDs have only spectral types M6–M9 in common. For these late-M types, the SEDs are consistent within our uncertainties, but we note that our absolute magnitudes are mostly $\approx 0.1 - 0.3$ mag fainter. In Figure 9 we compare our PS1 colors for M dwarfs from Table 4 to the PS1 colors from D16. The colors are generally quite consistent, although our $g_{P1} - r_{P1}$ colors are $\approx 0.5\sigma - 1\sigma$ bluer and our $z_{P1} - y_{P1}$ colors are $\approx 1\sigma - 2\sigma$ redder than those of D16. The differences in colors are due to the fact that D16 used an earlier processing version

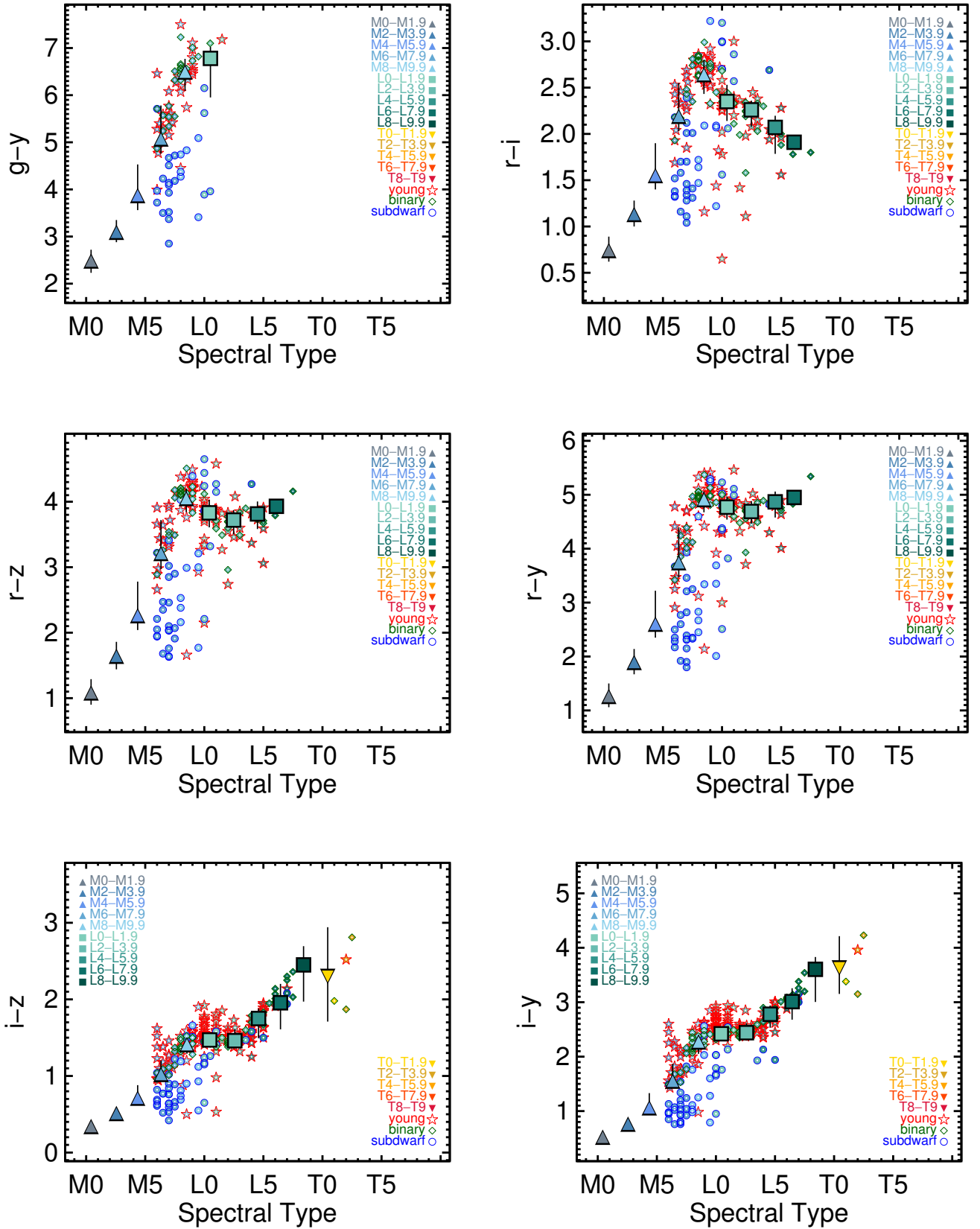


Figure 6. Color vs. spectral type plots for known young objects (outlined with red stars), binaries (green diamonds), and subdwarfs (blue circles) in our PS1-detected catalog. Interiors of the symbols use the same color scheme as in Figure 5 (see legends). Median colors and 68% confidence limits for normal field objects from Figure 5 are overplotted for reference. Typically the young objects have field-like or redder colors while the subdwarfs have bluer-than-field colors, but the $r_{P1} - i_{P1}$, $r_{P1} - z_{P1}$, and $r_{P1} - y_{P1}$ vs. SpT plots show a number of exceptions to both of these norms.

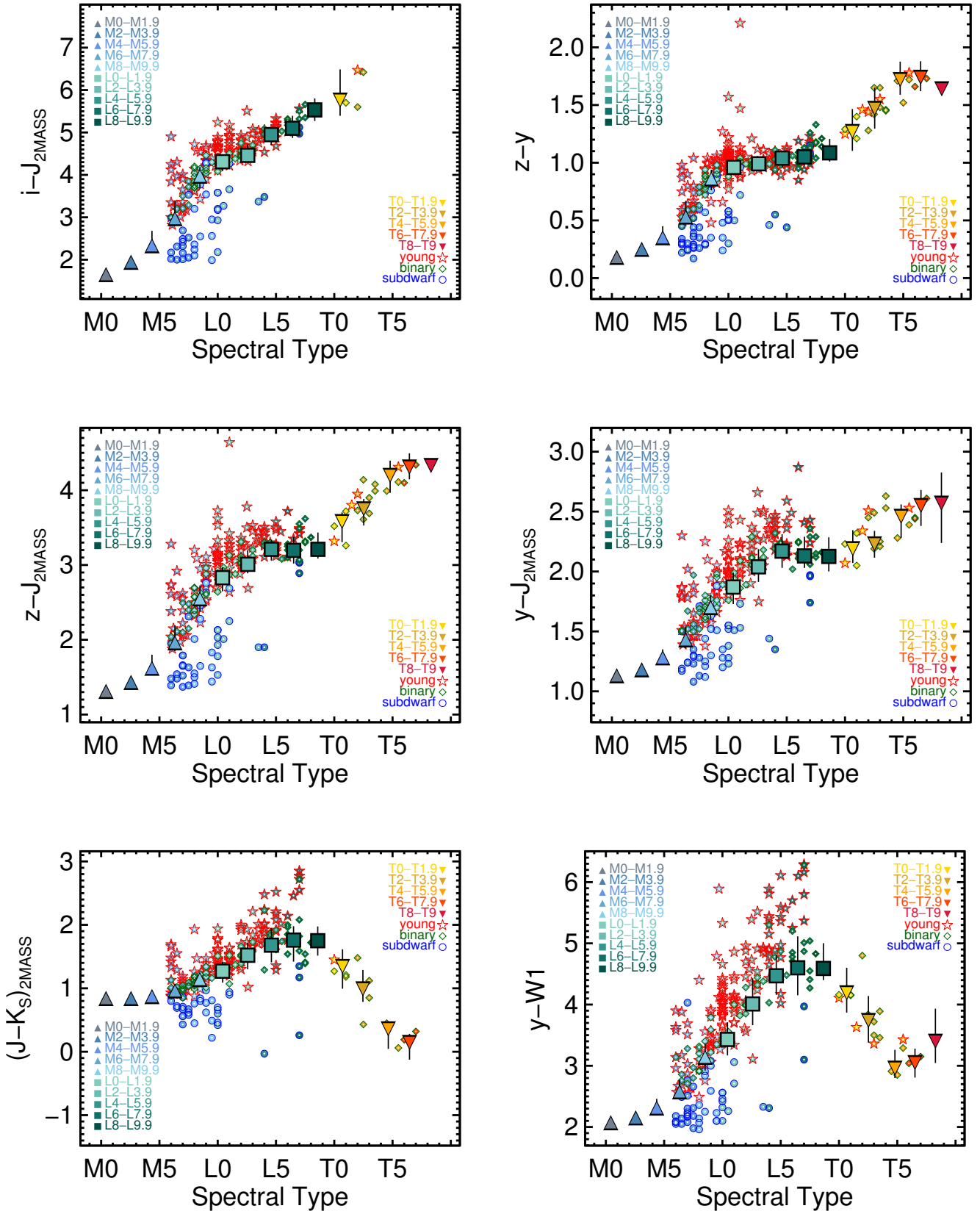


Figure 6. continued.

Table 4. Median Colors of M0–T9 Dwarfs

SpT	$gP1 - rP1$		$rP1 - iP1$		$iP1 - zP1$		$zP1 - yP1$		$yP1 - J_{2MASS}$		$(J - H)_{2MASS}$		$(H - K_S)_{2MASS}$		$K_S - 2MASS - W1$		$W1 - W2$		$W2 - W3$			
	Median (mag)	N	Median (mag)	N	Median (mag)	N	Median (mag)	N	Median (mag)	N	Median (mag)	N	Median (mag)	N	Median (mag)	N	Median (mag)	N	Median (mag)	N	Median (mag)	N
M0–M0.9	1.19	991	0.67	991	0.31	991	0.17	991	1.12	991	0.66	991	0.18	991	0.10	969	0.02	969	0.06	969	...	0
M1–M1.9	1.22	707	0.85	707	0.39	707	0.20	707	1.14	707	0.64	707	0.21	707	0.11	700	0.07	700	0.05	700	...	0
M2–M2.9	1.21	1657	1.02	1657	0.46	1657	0.23	1657	1.16	1657	0.62	1657	0.22	1657	0.12	1633	0.12	1633	0.06	1633	...	0
M3–M3.9	1.21	2107	1.22	2107	0.55	2107	0.27	2107	1.20	2106	0.60	2106	0.24	2107	0.14	2079	0.16	2079	0.05	2079	...	0
M4–M4.9	1.23	1220	1.46	1220	0.67	1220	0.32	1220	1.25	1220	0.59	1220	0.26	1220	0.16	1198	0.18	1198	0.03	1198	...	0
M5–M5.9	1.31	683	1.88	683	0.87	683	0.44	683	1.34	683	0.59	683	0.31	683	0.19	676	0.21	676	0.03	676	...	44
M6–M6.9	1.33	399	2.13	399	0.98	399	0.51	399	1.40	391	0.60	401	0.33	402	0.20	388	0.22	388	0.03	388	...	40
M7–M7.9	1.40	155	2.55	155	1.21	157	0.67	157	1.54	154	0.63	157	0.39	157	0.22	147	0.23	147	0.02	147	...	60
M8–M8.9	1.53	90	2.69	108	1.38	108	0.81	108	1.66	108	0.68	108	0.43	111	0.26	99	0.23	99	0.04	97	...	52
M9–M9.9	1.79	35	2.58	59	1.44	59	0.92	85	1.77	61	0.72	60	0.48	64	0.31	56	0.26	56	0.05	63	...	35
L0–L0.9	1.85	16	2.35	202	1.47	202	0.95	344	1.82	307	0.76	307	0.48	277	0.32	263	0.27	263	0.07	311	...	21
L1–L1.9	2.00	11	2.35	113	1.48	113	0.97	225	1.94	232	0.80	166	0.51	168	0.35	152	0.26	152	0.06	189	...	16
L2–L2.9	2.30	1	2.27	50	1.45	50	1.01	109	2.00	90	0.91	90	0.59	89	0.42	82	0.29	82	0.04	96	...	14
L3–L3.9	2.70	...	2.23	31	1.49	31	1.49	97	1.01	97	0.95	78	0.64	77	0.52	73	0.30	73	0.06	90	...	11
L4–L4.9	2.11	17	1.63	17	1.02	68	2.15	54	1.06	54	0.64	51	0.61	50	0.32	50	0.06	71	...	8
L5–L5.9	2.00	13	1.77	13	1.05	64	2.18	55	1.06	55	0.67	55	0.67	50	0.33	50	0.08	74	...	8
L6–L6.9	1.91	5	1.89	5	1.05	34	2.09	32	0.99	32	0.65	34	0.71	35	0.38	35	0.09	43	...	5
L7–L7.9	0	2.10	0	1.02	16	2.19	21	1.12	21	0.73	20	0.73	17	0.42	17	0.12	23	...	2
L8–L8.9	2.13	1	2.45	1	1.05	17	2.14	22	1.13	22	0.65	23	0.85	26	0.53	26	0.08	27	...	5
L9–L9.9	0	2.45	0	1.16	8	2.11	28	1.07	28	0.64	28	0.85	28	0.53	28	0.09	27	...	3
T0–T0.9	0	2.38	0	1.21	24	2.21	13	0.93	13	0.56	12	0.78	22	0.57	22	0.10	32	...	3
T1–T1.9	0	2.30	0	1.39	25	2.19	14	0.86	14	0.33	12	0.78	13	0.58	13	0.09	21	...	1
T2–T2.9	0	3.53	0	1.45	39	2.22	39	0.80	39	0.25	16	0.67	16	0.72	16	0.10	25	...	3
T3–T3.9	0	2.85	0	1.55	23	2.24	22	0.80	22	0.17	17	0.57	17	0.91	17	0.14	39	...	5
T4–T4.9	0	...	0	1.71	30	2.24	23	0.59	23	0.17	7	0.56	8	1.07	8	0.19	19
T5–T5.9	0	3.49	0	1.74	32	2.49	30	0.18	30	0.03	10	0.15	7	1.35	7	0.25	26	...	1
T6–T6.9	0	...	0	1.74	32	2.54	38	0.05	38	0.06	20	0.37	14	1.85	14	0.32	40	...	0
T7–T7.9	0	...	0	1.80	15	2.56	21	0.08	21	0.01	12	0.33	5	2.08	5	0.36	47	...	2
T8–T8.9	0	...	0	1.76	4	2.57	9	0.09	9	...	1	...	0	2.26	0	0.34	27	...	3
T9–T9.9	0	...	0	1.37	1	2.61	2	0.24	2	...	1	...	0	2.79	0	0.44	10	...	3

NOTE—For each spectral type and color, this table lists the median color and 68% confidence limits followed by the number of objects (N) used to determine the median. Confidence intervals were calculated only when $N \geq 7$.

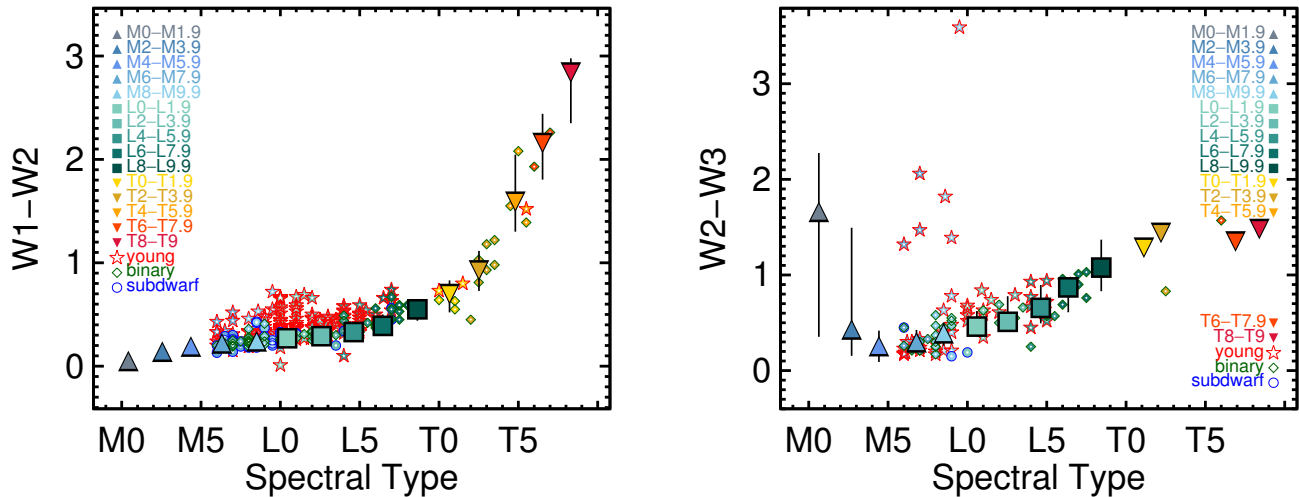


Figure 6. continued.

(PV2) of PS1 data, and likely also to differences in our input samples (DL16 used ≈ 500 M dwarfs, while our sample contains over 8000 M dwarfs). We also find a significant blueward turn in the $r_{P1} - i_{P1}$ colors of M9 dwarfs (that continues into the L dwarfs) that D16 do not identify. D16 converted spectral types into absolute magnitudes using bolometric magnitudes and a series of color transformations fitted with splines. In particular, D16 used $g_{P1} - i_{P1}$ as a proxy for spectral type, and this relation does not clearly distinguish M9 dwarfs from M6–M8 dwarfs, so the sudden turn for M9 in $r_{P1} - i_{P1}$ could not be detected by their method.

4. PROPER MOTION

Table 7 presents our proper motions for 9770 M, L, and T dwarfs based on PS1 astrometry, along with parallaxes (from the literature) or photometric distances, tangential velocities, and proper motions from the literature for comparison. The full table is available for download in electronic form from the online journal. Like Table 1, Table 7 is arranged in two parts: (1) the late-M, L, and T dwarfs compiled from the literature, followed by (2) the M dwarfs from West et al. (2008). For reference, Table 7 also repeats several columns from Table 1, including spectral types, gravity classifications, and flags for binaries and young objects.

4.1. Method

4.1.1. PS1 database proper motions

The procedure used to calculate the proper motions and errors for the objects in the PS1 database will be described in detail in Magnier et al. (2017). Briefly, all detections for an object in all filters were fit simultaneously for proper motion and parallax using iteratively-reweighted least-squares regression with outlier clipping. The detections retained in the fit were then bootstrap-resampled to determine the errors on the proper motion and parallax. For objects having a 2MASS or *Gaia* DR1 counterpart within 1" of the mean PS1 position, the PS1 proper motion calculation includes these positions. (The parallaxes will be presented in E. A. Magnier et al., 2018, in prep). For this paper we also convert the PS1-measured $\mu_{\alpha} \cos \delta$ and μ_{δ} to a combined proper motion μ and position angle PA, and we calculate errors for these in a Monte Carlo fashion. To establish a minimum quality for our PS1 proper motions, if either $\mu_{\alpha} \cos \delta$ or μ_{δ} for an object has an error greater than 100 mas yr^{-1} and $\mu/\sigma_{\mu} < 3$, we do not report a proper motion for the object. This rejects large but very uncertain proper motions that may erroneously identify fast-moving objects (e.g., $500 \pm 300 \text{ mas yr}^{-1}$), but preserves high-precision measurements of very small proper motions that have a formal $S/N < 3$ (e.g., $5 \pm 3 \text{ mas yr}^{-1}$).

4.1.2. PS1 mean positions and epoch

Table 7 includes a mean PS1 position and epoch for each object. To determine these, the PS1 astrometric pipeline calculates a weighted mean epoch t_0 , in which the epochs are weighted by the rms of the R.A. and Decl. astrometric

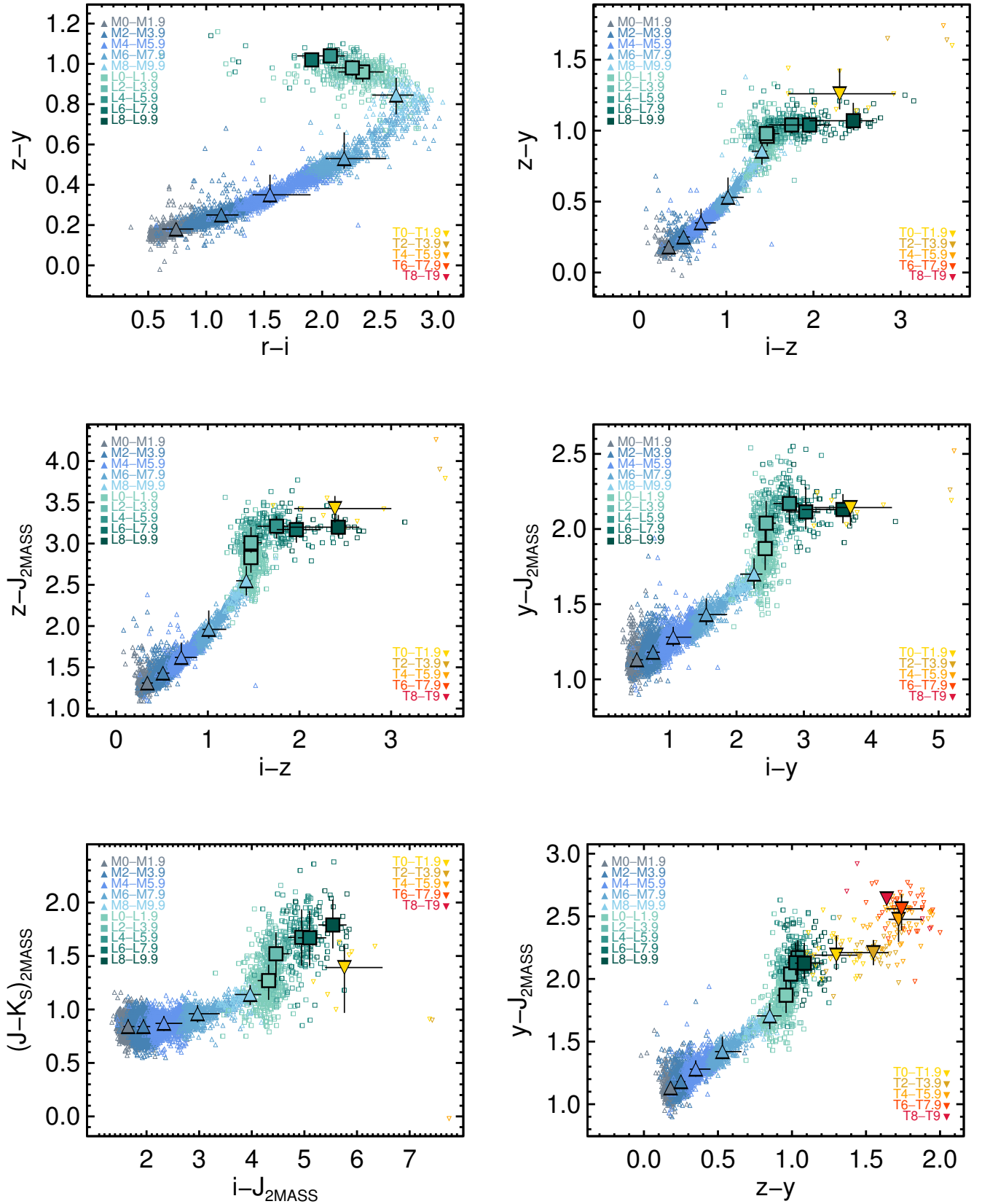


Figure 7. Color-color plots for the M, L, and T dwarfs in our PS1-detected catalog, using the same format as in Figure 5. The L dwarf color plateau is especially evident for $z_{P1} - y_{P1}$ and $z_{P1} - J_{2MASS}$.

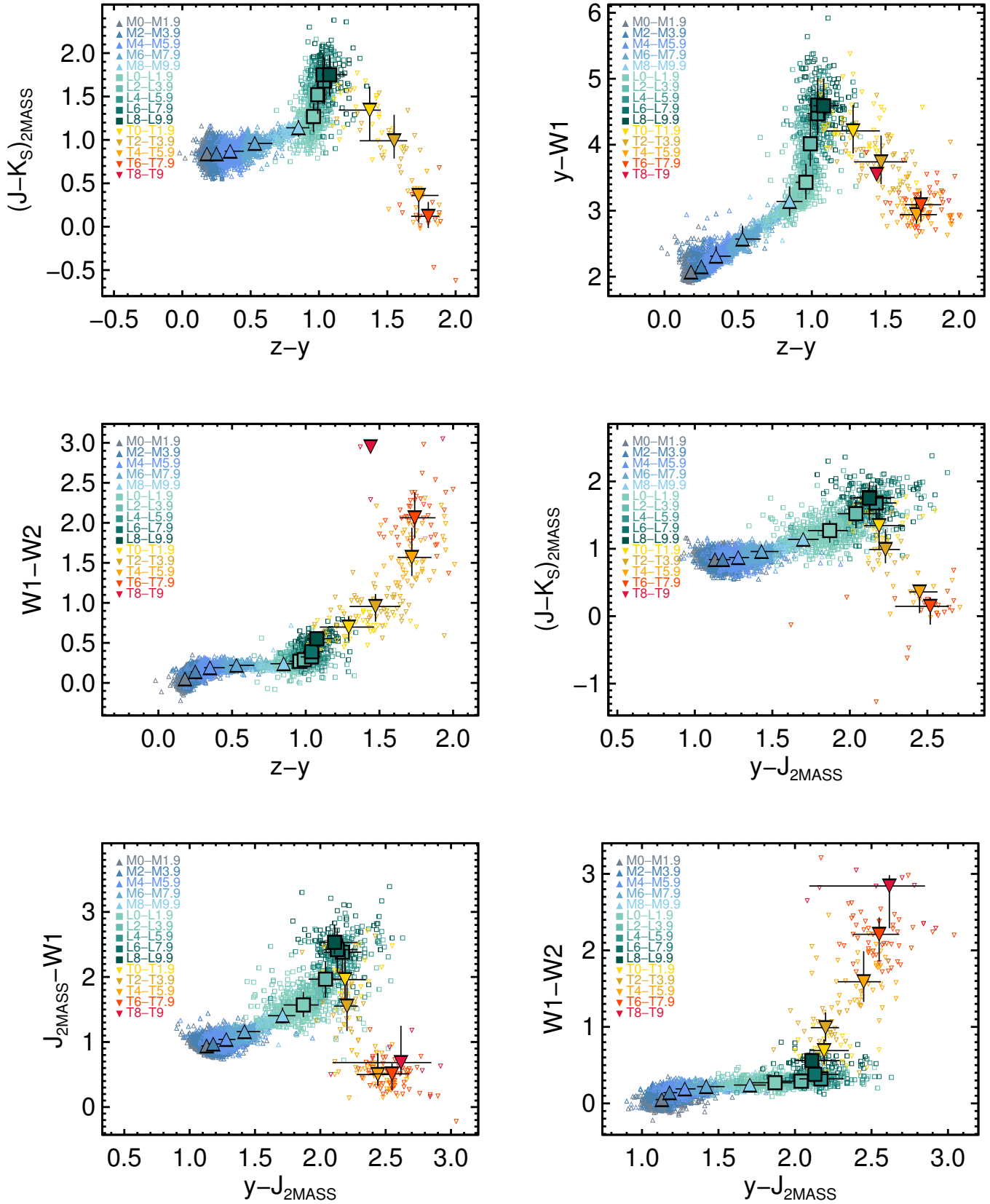


Figure 7. continued.

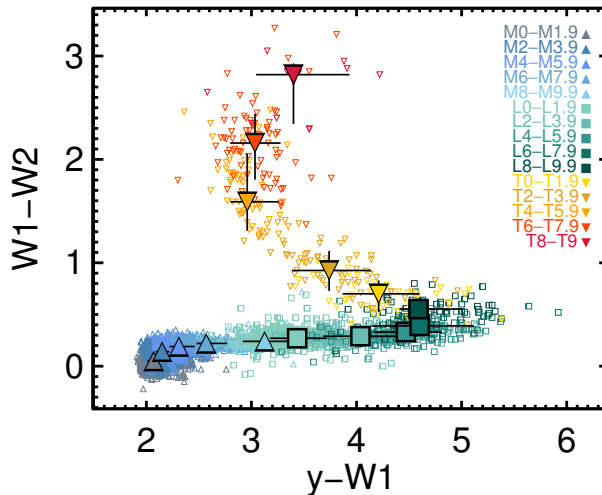


Figure 7. continued.

uncertainties. The mean position (α_0, δ_0) is calculated (in simple terms) by fitting the positions (α, δ) at each epoch t to

$$\begin{aligned}\alpha(t) &= \alpha_0 + \pi p_\alpha(t) + \mu_\alpha(t - t_0)/\cos(\delta) \\ \delta(t) &= \delta_0 + \pi p_\delta(t) + \mu_\delta(t - t_0)\end{aligned}\quad (1)$$

where π is the parallax, and p_α and p_δ are the parallax factors in R.A. and Decl., respectively. This is also, by construction, the position at which the covariance with the proper motion is minimized, and is therefore the best position given the set of observations. In cases where the pipeline is unable to fit a proper motion to the data, the mean position coordinates are simply the weighted means of the individual epochs. For objects with an associated 2MASS or *Gaia* DR1 detection, these are included in determining the mean epoch and position.

4.1.3. Our proper motion calculation

The PS1 database builds astronomical objects from individual detections at different epochs by grouping detections within $1''$ of each other. In cases where two distinct objects are detected within $1''$ of each other at a single epoch, detections at other epochs are associated with the closer of the two objects (for details, see [Magnier et al. 2017](#)). This procedure is successful for stationary and slow-moving point sources, but for an object that moved $\gtrsim 1''$ over the four-year timespan of the PS1 survey, the detections may not all be associated in the PS1 database. In our ultracool catalog, we found that objects with proper motions $\gtrsim 200$ mas yr $^{-1}$ were often split into two or more “partial objects”, identifiable by their proximity on the sky, similar photometry, and astrometric consistency with proper motions from the literature. These partial objects often had significantly different proper motion measurements but offered no *a priori* way to determine which (if any) of the measurements was correct. This motivated us to recalculate the proper motions for fast-moving objects, using an automated procedure to identify all the detections for an object along its path of motion. While our primary goal was to improve the proper motions of fast-moving objects, we performed the recalculation for all objects of spectral type M6 and later in our catalog.

To determine where to search for detections for each object, we calculated the distance between the PS1 and 2MASS positions and generated a search box for the PS1 data based on the implied proper motion of the distance divided by a baseline of 12 years. We added $4''$ in quadrature to 5 years times the implied proper motion and used the resulting value for the length of a square search box. We searched the PS1 and 2MASS databases for all detections within this box centered on the PS1 position. In cases where the 2MASS and PS1 positions were more than $2''$ apart, we also searched around the 2MASS position within a $1''$ box. Once we identified candidate detections, we determined the path on the sky from the 2MASS position to the PS1 position, and if the 2MASS–PS1 distance was more than $3''$, we excluded any points that were more than $1''$ away from the path. For objects in our catalog with no associated 2MASS detection, we used the proper motion from the PS1 database (if available) or the best available proper motion from

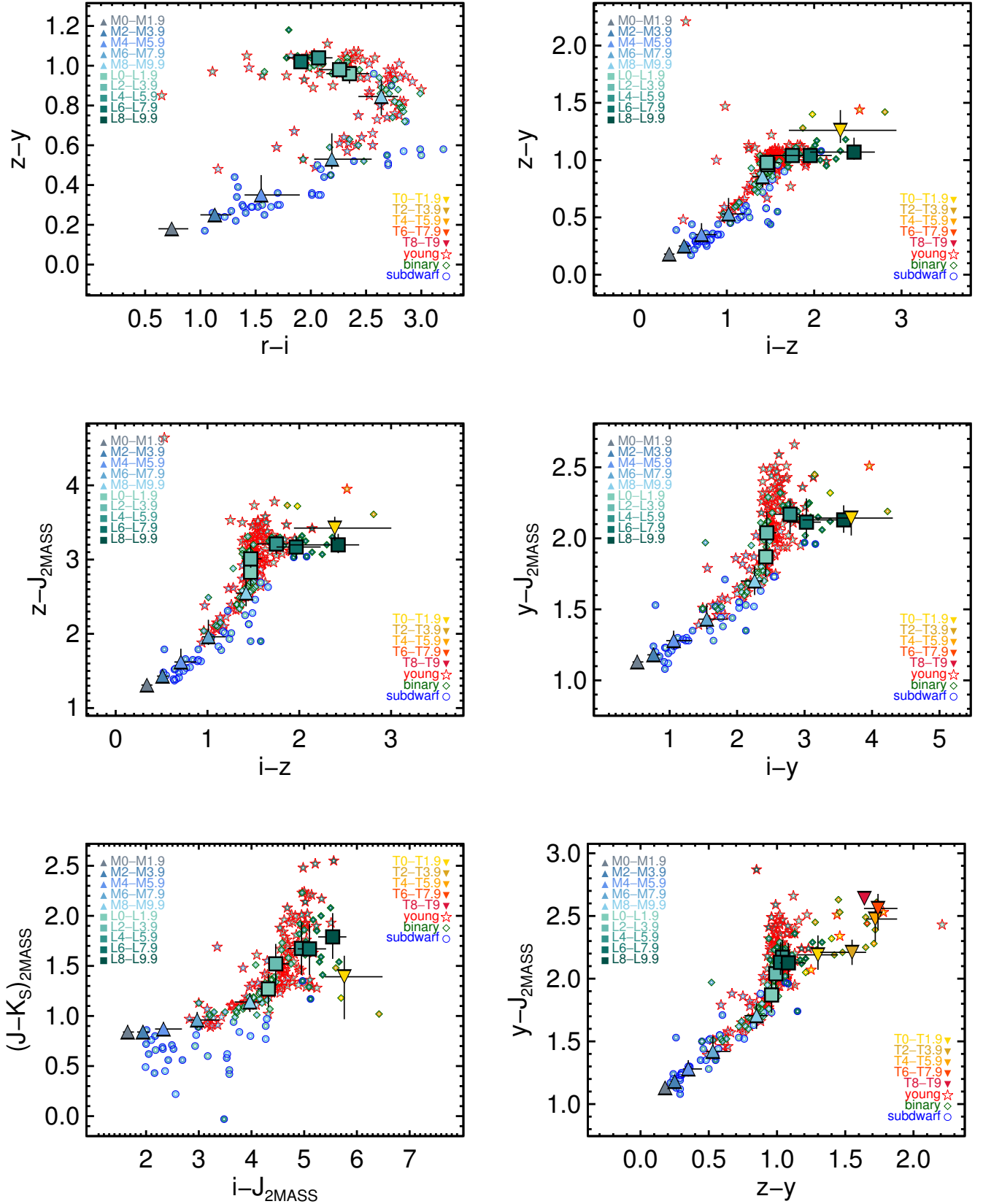


Figure 8. Color-color plots for known young objects, binaries, and subdwarfs in our PS1-detected catalog, using the same format as in Figure 6. Median colors and 68% confidence limits for normal field objects from Figure 7 are overlotted for reference.

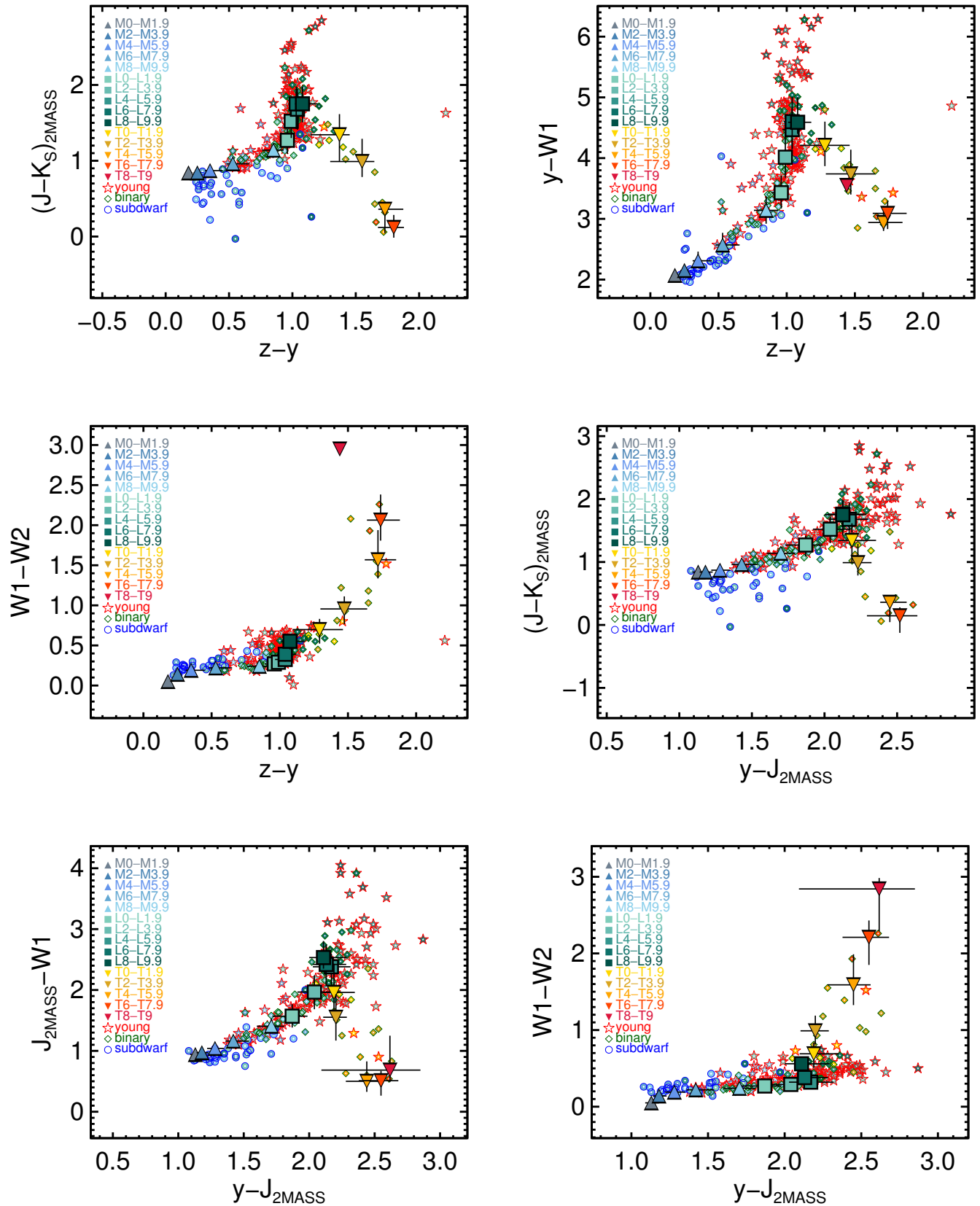


Figure 8. continued.

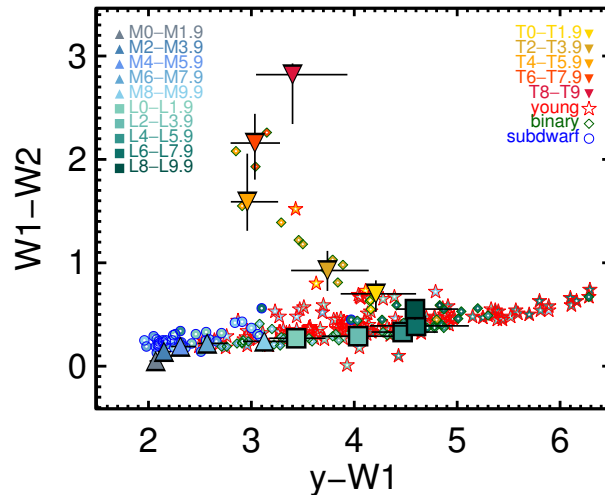


Figure 8. continued.

the literature to predict a 2MASS position by projecting backward 10 years from the PS1 position. For objects with no associated 2MASS detection and no PS1 or literature proper motion, we simply searched in a $4''$ box around the PS1 position. Finally, we searched the *Gaia* DR1 database for detections within $1''$ of the PS1 position, and included the astrometry from a *Gaia* match if one was found.

We then calculated proper motions using the method summarized in Section 4.1.1 for objects having at least seven detections (to ensure robust astrometric fits). We applied the same quality standards that we used for the PS1 database proper motions, rejecting those for which $\mu_\alpha \cos \delta$ or μ_δ had an error greater than 100 mas yr^{-1} and $\mu/\sigma_\mu < 3$. Our recalculations produced proper motions for 2376 M6–T9 dwarfs. These included 63 objects that do not have a proper motion in the PS1 database, most of which are moving faster than 200 mas yr^{-1} , demonstrating the success of our method. The largest proper motion for objects in our catalog reported in the PS1 database is 1561 mas yr^{-1} , but our recalculated measurements include 16 objects with greater proper motions, up to a maximum of 3507 mas yr^{-1} (SSSPM J1444–2019). The recalculation was unable to converge on a proper motion fit to the identified detections for 154 objects. 41 of the objects for which the recalculation failed do have PS1 database proper motions, but these are mostly poor measurements ($\sigma_\mu \gtrsim 40 \text{ mas yr}^{-1}$) for faint objects ($y \gtrsim 20 \text{ mag}$) with relatively few detections ($N \lesssim 10$).

Figure 10 compares our recalculated proper motions and errors to the values in the PS1 database. The recalculated proper motions are strongly consistent with the database measurements, and the errors for the recalculated proper motions are lower for 87% of the objects, with a median improvement in precision of 35%. We examined all objects for which the recalculated $\mu_\alpha \cos \delta$ or μ_δ differed by more than three times the error on the corresponding value in the PS1 database, and identified only six cases in which the recalculation produced a result clearly inconsistent with the separation between the PS1 and 2MASS positions or with a literature measurement. In each of these six cases, a nearby object appears to have significantly contaminated the proper motion calculation. We rejected the recalculated values for these six objects. In all other cases of significant discrepancy, the recalculated proper motion was consistent with a value in the literature (except for one object with no literature value), confirming that our recalculation improved the accuracy of these proper motions.

For our catalog (Table 7), we adopt the recalculated proper motions by default. We also present mean positions and epochs from our recalculations, which incorporate the 2MASS and *Gaia* DR1 positions used in the calculations. We use the PS1 database proper motions and positions only for the six contaminated recalculations described above and in 41 cases where our recalculation was unable to fit a proper motion. We also recalculated chip photometry for each object along with the proper motion, but we did not apply the rigorous outlier-clipping procedure used for the PS1 database photometry, so by default we use the database photometry in our catalog. We use our recalculated chip photometry in 55 cases where the database reports photometry of insufficient quality (or none at all) and our recalculated photometry passes the quality standards described in Section 3.1.2.

Table 5. More Median Colors

SpT	$i_{P1} - y_{P1}$			$i_{P1} - J_{2MASS}$			$z_{P1} - J_{2MASS}$			$(J - K_S)_{2MASS}$			$y_{P1} - W1$		
	Median	68%	<i>N</i>	Median	68%	<i>N</i>	Median	68%	<i>N</i>	Median	68%	<i>N</i>	Median	68%	<i>N</i>
	(mag)	(mag)		(mag)	(mag)		(mag)	(mag)		(mag)	(mag)		(mag)	(mag)	
M0–M0.9	0.48	+0.05 –0.05	991	1.61	+0.07 –0.08	991	1.29	+0.05 –0.05	991	0.84	+0.06 –0.06	991	2.05	+0.06 –0.06	969
M1–M1.9	0.59	+0.05 –0.05	707	1.74	+0.07 –0.08	707	1.34	+0.05 –0.04	707	0.85	+0.06 –0.07	707	2.10	+0.06 –0.05	700
M2–M2.9	0.69	+0.05 –0.04	1657	1.85	+0.07 –0.06	1657	1.39	+0.05 –0.05	1657	0.84	+0.06 –0.08	1657	2.12	+0.06 –0.05	1633
M3–M3.9	0.82	+0.06 –0.06	2107	2.02	+0.09 –0.09	2106	1.46	+0.06 –0.05	2106	0.84	+0.06 –0.07	2106	2.17	+0.06 –0.06	2079
M4–M4.9	0.99	+0.09 –0.06	1220	2.24	+0.13 –0.09	1220	1.57	+0.07 –0.06	1220	0.86	+0.06 –0.07	1220	2.26	+0.07 –0.07	1198
M5–M5.9	1.31	+0.07 –0.07	683	2.66	+0.09 –0.11	683	1.78	+0.07 –0.07	683	0.91	+0.06 –0.07	683	2.44	+0.06 –0.07	676
M6–M6.9	1.48	+0.13 –0.07	389	2.89	+0.17 –0.11	387	1.91	+0.11 –0.07	386	0.93	+0.07 –0.07	401	2.54	+0.10 –0.08	381
M7–M7.9	1.87	+0.25 –0.13	158	3.41	+0.30 –0.21	153	2.21	+0.18 –0.14	152	1.02	+0.07 –0.07	157	2.78	+0.17 –0.17	145
M8–M8.9	2.19	+0.14 –0.18	120	3.85	+0.19 –0.21	108	2.46	+0.14 –0.13	107	1.12	+0.06 –0.10	111	3.03	+0.15 –0.17	100
M9–M9.9	2.35	+0.11 –0.10	85	4.16	+0.11 –0.17	61	2.71	+0.09 –0.15	61	1.19	+0.15 –0.07	60	3.33	+0.17 –0.15	68
L0–L0.9	2.41	+0.07 –0.07	344	4.24	+0.15 –0.18	307	2.76	+0.15 –0.15	307	1.24	+0.13 –0.15	278	3.35	+0.26 –0.25	320
L1–L1.9	2.45	+0.11 –0.10	225	4.38	+0.15 –0.10	175	2.90	+0.13 –0.12	176	1.32	+0.16 –0.19	165	3.59	+0.25 –0.26	201
L2–L2.9	2.41	+0.12 –0.09	107	4.41	+0.18 –0.11	90	2.98	+0.11 –0.10	90	1.49	+0.19 –0.22	89	3.90	+0.36 –0.25	99
L3–L3.9	2.51	+0.14 –0.18	97	4.63	+0.20 –0.28	78	3.11	+0.13 –0.18	78	1.58	+0.21 –0.24	77	4.26	+0.23 –0.57	94
L4–L4.9	2.68	+0.20 –0.20	68	4.84	+0.26 –0.25	51	3.17	+0.15 –0.16	54	1.65	+0.29 –0.31	52	4.39	+0.31 –0.36	72
L5–L5.9	2.83	+0.12 –0.23	64	5.02	+0.14 –0.25	51	3.25	+0.10 –0.16	55	1.75	+0.20 –0.26	53	4.59	+0.30 –0.30	74
L6–L6.9	2.96	+0.25 –0.35	34	5.09	+0.24 –0.22	28	3.17	+0.15 –0.16	32	1.59	+0.38 –0.19	30	4.55	+0.23 –0.39	43
L7–L7.9	3.07	+0.37 –0.23	16	5.15	+0.43 –0.24	12	3.25	+0.16 –0.11	20	1.82	+0.16 –0.17	18	4.68	+0.52 –0.52	23
L8–L8.9	3.45	+0.32 –0.49	16	5.48	+0.32 –0.31	14	3.20	+0.23 –0.11	23	1.86	+0.15 –0.24	23	4.78	+0.37 –0.26	26
L9–L9.9	3.60	+0.76 –0.37	8	5.63	...	6	3.23	+0.27 –0.15	28	1.67	+0.27 –0.21	26	4.54	+0.19 –0.19	33
T0–T0.9	3.52	...	6	5.66	...	5	3.42	+0.26 –0.18	13	1.48	+0.14 –0.35	11	4.29	+0.35 –0.36	21
T1–T1.9	3.72	...	3	5.85	...	3	3.59	+0.12 –0.13	14	1.18	+0.38 –0.29	13	4.10	+0.43 –0.42	25
T2–T2.9	5.17	...	1	7.43	...	1	3.72	+0.13 –0.26	21	1.06	+0.33 –0.18	16	3.83	+0.31 –0.36	41
T3–T3.9	4.50	...	1	0	3.82	+0.13 –0.18	10	0.82	+0.34 –0.30	7	3.65	+0.50 –0.57	21
T4–T4.9	0	0	4.13	+0.10 –0.24	21	0.40	+0.04 –0.19	9	3.07	+0.44 –0.20	27
T5–T5.9	5.23	...	1	7.75	...	1	4.26	+0.20 –0.27	27	0.17	...	6	2.92	+0.23 –0.12	40
T6–T6.9	0	0	4.29	+0.15 –0.18	27	0.16	+0.13 –0.18	15	3.02	+0.22 –0.22	49
T7–T7.9	0	0	4.38	+0.15 –0.20	10	0.08	+0.22 –0.31	7	3.16	+0.39 –0.35	28
T8–T8.9	0	0	4.34	...	4	0	3.34	+0.60 –0.35	9
T9–T9.9	0	0	4.07	...	1	0	3.66	...	2

NOTE—For each spectral type and color, this table lists the median color and 68% confidence limits followed by the number of objects (*N*) used to determine the median. Confidence intervals were calculated only when $N \geq 7$.

4.2. Characteristics

For the remainder of Section 4, we restrict our discussion to objects with spectral types M6 and later in order to focus our kinematic analysis on ultracool dwarfs near the Sun. Early-M dwarfs are visible at distances well beyond the solar neighborhood ($\gtrsim 200$ pc) where large-scale galactic motions dominate the kinematics, entailing a discussion that is beyond the scope of this paper. We report PS1 proper motions for a total of 2405 M6–T9 dwarfs, including the largest sets of uniformly-calculated proper motions for confirmed L dwarfs (1242 objects) and T dwarfs (260 objects) to date. We caution that the proper motions in our catalog do not comprise a clearly-defined sample and reflect biases inherited from the programs that discovered the objects (Section 2.7), but our proper motions nevertheless serve as a large and illustrative sample of the local ultracool population.

Figure 11 shows the time baselines and number of epochs used for the ultracool proper motions in our catalog. Most of our proper motions were calculated using a 2MASS position and have time baselines spanning 13–17 years. Proper motions using only PS1 astrometry have time baselines spanning 1–5 years (data taken 2009–2014, including during PS1 commissioning). For about one-quarter of our sample (593 objects), a *Gaia* DR1 position was included in our proper motion.

Figures 12 and 13 show the proper motion distributions for our PS1 ultracool catalog. We find median proper motion components of $\mu_\alpha \cos \delta = -13.4$ mas yr $^{-1}$ and $\mu_\delta = -37.1$ mas yr $^{-1}$. Our distributions are similar to those found in previous catalogs of ultracool proper motions, including the L dwarf catalog of Schmidt et al. (2010, hereinafter S10), the Brown Dwarf Kinematics Project (BDKP; Faherty et al. 2009, 2012), the BANYAN All-Sky Survey (BASS) Input

Table 6. Spectral Energy Distributions for Field Ultracool Dwarfs

SpT	N	M_{gp1}		M_{rp1}		M_{ip1}		M_{zp1}		M_{yp1}		M_{J2MASS}		M_{H2MASS}		$M_{Ks2MASS}$		M_{W1}		M_{W2}		M_{W3}	
		Mean (mag)	σ (mag)	Mean (mag)	σ (mag)	Mean (mag)	σ (mag)	Mean (mag)	σ (mag)	Mean (mag)	σ (mag)	Mean (mag)	σ (mag)	Mean (mag)	σ (mag)	Mean (mag)	σ (mag)	Mean (mag)	σ (mag)	Mean (mag)	σ (mag)	Mean (mag)	σ (mag)
M6-M6.9	30	16.71	0.44	15.37	0.43	13.25	0.34	12.27	0.32	11.76	0.30	10.36	0.30	9.76	0.30	9.43	0.31	9.22	0.30	9.01	0.30	8.72	0.34
M7-M7.9	26	18.11	0.56	16.76	0.50	14.18	0.39	12.98	0.34	12.31	0.31	10.77	0.30	10.14	0.31	9.75	0.31	9.52	0.31	9.31	0.31	8.96	0.33
M8-M8.9	21	19.19	0.59	17.74	0.51	15.00	0.48	13.61	0.45	12.81	0.43	11.15	0.42	10.47	0.43	10.03	0.43	9.78	0.43	9.55	0.44	9.18	0.47
M9-M9.9	9	19.95	0.43	18.14	0.37	15.62	0.39	14.17	0.37	13.23	0.36	11.46	0.34	10.74	0.35	10.27	0.37	9.95	0.37	9.68	0.37	9.24	0.42
L0-L0.9	17	20.33	0.40	18.37	0.31	16.00	0.26	14.52	0.25	13.58	0.23	11.76	0.18	11.00	0.23	10.52	0.24	10.22	0.26	9.94	0.26	9.35	0.32
L1-L1.9	19	20.85	0.78	18.74	0.28	16.41	0.25	14.93	0.23	13.97	0.21	12.03	0.15	11.23	0.21	10.71	0.24	10.36	0.26	10.10	0.26	9.66	0.31
L2-L2.9	12	21.24	...	19.02	0.29	16.73	0.26	15.30	0.24	14.33	0.24	12.92	0.21	11.41	0.25	10.83	0.29	10.43	0.32	10.14	0.33	9.62	0.37
L3-L3.9	8	22.51	...	19.61	0.39	17.40	0.34	15.88	0.31	14.89	0.29	12.77	0.24	11.82	0.29	11.19	0.32	10.66	0.36	10.39	0.38	9.91	0.37
L4-L4.9	8	20.60	0.56	18.35	0.38	16.68	0.33	15.66	0.32	13.51	0.28	12.45	0.33	11.85	0.40	11.18	0.43	10.84	0.46	10.05	0.44
L5-L5.9	8	20.74	0.37	18.71	0.33	16.94	0.29	15.87	0.28	13.69	0.25	12.63	0.30	11.94	0.34	11.26	0.34	10.91	0.38	10.13	0.51
L6-L6.9	9	21.21	0.78	19.27	0.65	17.35	0.62	16.27	0.61	14.18	0.60	13.19	0.62	12.58	0.68	11.85	0.71	11.49	0.75	10.53	0.87
L7-L7.9	7	20.09	0.36	18.18	0.26	17.13	0.25	14.94	0.20	13.82	0.31	13.12	0.32	12.42	0.48	11.99	0.57	10.87	1.08
L8-L8.9	10	22.88	...	20.38	0.39	18.10	0.22	17.04	0.21	14.90	0.13	13.77	0.20	13.04	0.22	12.20	0.28	11.66	0.30	10.66	0.36
L9-L9.9	3	20.09	0.79	17.69	0.73	16.57	0.72	14.46	0.71	13.39	0.73	12.79	0.74	11.94	0.74	11.45	0.77	10.48	0.75
T0-T0.9	1	20.22	...	17.98	...	16.77	...	14.56	...	13.62	...	13.08	...	12.43	...	11.94	...	11.02	...
T1-T1.9	3	21.10	1.14	18.84	0.21	17.45	0.16	15.25	0.12	14.39	0.18	14.07	0.33	13.39	0.38	12.68	0.33	11.26	0.76
T2-T2.9	5	21.97	...	18.26	0.23	16.75	0.13	14.54	0.06	13.73	0.15	13.48	0.26	12.94	0.39	12.06	0.33	10.61	0.40
T3-T3.9	2	18.08	0.25	16.50	0.22	14.26	0.16	13.67	0.24	13.44	0.32	12.84	0.61	11.72	0.45
T4-T4.9	6	18.02	0.39	16.32	0.38	13.89	0.36	13.57	0.40	13.49	0.39	13.31	0.41	11.90	0.39	10.70	...
T5-T5.9	7	22.69	...	19.20	0.22	17.43	0.18	14.94	0.12	14.76	0.24	14.77	0.23	14.52	0.25	12.69	0.24	11.37	...
T6-T6.9	11	19.82	0.32	18.06	0.32	15.53	0.27	15.48	0.37	15.37	0.41	15.08	0.35	13.02	0.42	11.61	0.37
T7-T7.9	7	21.17	0.78	19.34	0.81	16.78	0.76	16.70	0.78	16.70	0.93	16.23	0.84	14.11	0.95	12.26	0.76
T8-T8.9	4	21.52	0.52	19.75	0.59	17.18	0.51	17.09	16.58	0.84	14.03	0.92	12.27	0.64
T9-T9.9	1	21.82	...	20.37	...	17.75	...	17.51	16.70	...	13.81	...	11.97	...

NOTE—SEDs constructed using parallaxes from the literature to determine absolute J_{2MASS} magnitudes, for which we report the weighted mean and rms for each spectral subtype bin. The number of objects used to determine M_{J2MASS} for each spectral subtype is listed in the second column (N). We use the median colors from our catalog to calculate absolute magnitudes in other bands. Binaries, subdwarfs, and young objects were excluded from these SEDs.

Table 7. Positions and Proper Motions of M, L, and T Dwarfs from the Pan-STARRS1 3π Survey

Discovery Name	Spectral Type ^{a,b}			Gravity ^b				PS1 Mean Position ^d		
	Opt	NIR	Adopted	Opt	NIR	Binary	Young ^c	α_{J2000} (deg)	δ_{J2000} (deg)	Epoch (MJD)
SDSS J000013.54+255418.6	T5	T4.5	T4.5	0.056400	25.905389	55326.38
SDSS J000112.18+153535.5	...	L3.7 INT-G	L3.7 INT-G	...	INT-G	...	Y	0.301175	15.592648	55750.95
WISEA J000131.93-084126.9	...	L1 pec (blue)	L1 pec (blue)	0.383130	-8.690953	55632.76
SDSS J000250.98+245413.8	...	L5.5	L5.5	0.712466	24.903795	55309.02
2MASS J0003422-282241	M7.5	M7: FLD-G	M7.5	...	FLD-G	0.927389	-28.378609	56120.45
2MASS J00044144-2058298	M8	...	M8	1.175450	-20.974698	55862.58
2MASS J00054844-2157196	M9	...	M9	1.454361	-21.955894	55708.99
ULAS J000613.24+154020.7	...	L9	L9	1.555343	15.672398	56032.02
SDSS J000614.06+160454.5	L0	...	L0	1.558610	16.081685	55734.32

PS1 Proper Motion											
$\mu_{\alpha \cos \delta}$ (mas yr ⁻¹)	err $\mu_{\alpha \cos \delta}$ (mas yr ⁻¹)	μ_{δ} (mas yr ⁻¹)	err μ_{δ} (mas yr ⁻¹)	μ (mas yr ⁻¹)	err μ (mas yr ⁻¹)	PA $_{\mu}$ (deg)	errPA $_{\mu}$ (deg)	χ^2_{ν}	N _{ep}	Δt (yr)	
-18.4	5.5	123.1	3.3	124.5	3.4	351.5	2.5	1.4	28	15.2	
137.3	2.2	-181.2	2.8	227.3	2.6	142.8	0.6	1.6	34	14.1	
339.9	2.6	-304.9	3.3	456.6	2.9	131.9	0.4	0.7	46	15.8	
22.4	17.4	-45.6	7.2	50.8	9.9	153.8	17.6	1.1	28	15.2	
285.8	1.5	-142.6	1.3	319.4	1.5	116.5	0.2	1.5	67	16.1	
751.9	1.9	91.9	2.5	757.5	1.9	83.0	0.2	2.0	74	15.1	
709.4	2.2	-122.9	2.5	720.0	2.2	99.8	0.2	1.7	66	14.9	
84.7	40.6	-38.5	20.4	93.0	35.6	114.4	21.4	0.9	16	3.9	
4.4	4.1	-41.8	3.9	42.0	3.9	174.0	5.6	0.7	40	17.2	

PS1 v_{\tan}						Literature Proper Motion					References ^f
π (mas)	err π (mas)	dist ^e (pc)	err $_{\text{dist}}$ (pc)	v_{\tan} (km s ⁻¹)	σ_{\tan} (km s ⁻¹)	$\mu_{\alpha \cos \delta}$ (mas yr ⁻¹)	err $\mu_{\alpha \cos \delta}$ (mas yr ⁻¹)	μ_{δ} (mas yr ⁻¹)	err μ_{δ} (mas yr ⁻¹)		
70.80	1.90	14.12	0.38	8.3	0.3	-19.1	1.5	126.7	1.3	43; 43	
...	...	24.34	2.93	26.2	3.2	135.2	10.7	-169.6	13.7	—; 54	
...	331.0	14.0	-299.0	14.0	—; 90	
...	...	53.33	6.54	12.8	3.0	—; —	
25.70	0.93	38.91	1.41	58.9	2.2	280.8	0.9	-141.5	0.8	131; 131	
...	...	18.94	3.14	68.0	11.3	825.5	75.7	-9.2	75.5	—; 70	
...	...	25.43	4.22	86.8	14.4	703.0	24.0	-119.0	4.0	—; 76	
...	...	43.24	5.35	19.1	7.7	92.9	23.3	-73.8	23.3	—; 74	
...	...	103.52	17.46	20.6	4.0	-5.0	19.0	-40.0	19.0	—; 139	

^a Spectral types taken from the literature (Section 2.4). When both optical and near-IR types are available, we adopt the optical type for M and L dwarfs and the near-IR type for T dwarfs. Most spectral types have an uncertainty of ± 0.5 subtypes; “:” = ± 1 subtype; “::” = ± 2 or more subtypes. “sd” = subdwarf; “esd” = extreme subdwarf (Gizis 1997).

^b β , γ , and δ indicate classes of increasingly low gravity based on optical (Kirkpatrick 2005; Cruz et al. 2009) or near-infrared (Gagné et al. 2015c) spectra. FLD-G indicates near-infrared spectral signatures of field-age gravity, INT-G indicates intermediate gravity, and VL-G indicates very low gravity (Allers & Liu 2013a).

^c Young objects identified by low-gravity classifications or other spectroscopic evidence for youth, membership in star-forming regions or young moving groups, or companionship to a young star (Section 2.5).

^d The mean PS1 position is the position calculated for the weighted mean epoch, in which the epochs are weighted by the rms of the R.A. and Decl. astrometric uncertainties.

^e Distances were calculated from trigonometric parallaxes when available. If no parallax was available, we calculated photometric distances using i_{P1} magnitudes for spectral types M0–M5 and $W2$ magnitudes (when available) for spectral types M6 and later.

^f References for spectral type, gravity, and binarity are given in Table 1.

^g Although classified as FLD-G, the spectrum shows hints of intermediate gravity (as described in Aller et al. 2016).

^h The R.A. and Decl. proper motion components listed in Table 2 of Lodieu et al. (2012b) appear to be reversed. We quote the corrected order here.

References—(1) Aberasturi et al. (2014), (2) Albert et al. (2011), (3) Aller et al. (2011), (4) Andrei et al. (2011), (5) Artigau et al. (2011), (6) Bardalez Gagliuffi et al. (2014), (7) Baron et al. (2015), (8) Bartlett (2007), (9) Beamin et al. (2013), (10) Béjar et al. (2008), (11) Best et al. (2015), (12) Best et al. (2017b), (13) Bihain et al. (2013), (14) Bouvier et al. (2008), (15) Bouy et al. (2015), (16) Burgasser et al. (2003b), (17) Burgasser et al. (2004), (18) Burgasser et al. (2007), (19) Burgasser et al. (2008a), (20) Burgasser et al. (2008c), (21) Burgasser et al. (2012), (22) Burgasser et al. (2015), (23) Burgasser et al. (2016), (24) Burningham et al. (2013), (25) Caballero (2007), (26) Cardoso et al. (2015), (27) Casewell et al. (2008), (28) Castro et al. (2013), (29) Castro & Gizis (2016), (30) Costa et al. (2005), (31) Costa et al. (2006), (32) Dahn et al. (2002), (33) Dahn et al. (2008), (34) Deacon et al. (2005), (35) Deacon & Hambly (2007), (36) Deacon et al. (2009), (37) Deacon et al. (2011), (38) Deacon et al. (2012b), (39) Deacon et al. (2014), (40) Deacon et al. (2017a), (41) Dieterich et al. (2014), (42) Dittmann et al. (2014), (43) Dupuy & Liu (2012), (44) Dupuy & Kraus (2013), (45) Dupuy et al. (2015), (46) Faherty et al. (2009), (47) Faherty et al. (2010), (48) Faherty et al. (2012), (49) Faherty et al. (2016), (50) Finch & Zacharias (2016), (51) Folkes et al. (2012), (52) Forbrich et al. (2016), (53) Gagné et al. (2014b), (54) Gagné et al. (2015b), (55) Gatewood & Coban (2009), (56) Gauza et al. (2015), (57) Gawroński et al. (2016), (58) Gelino et al. (2014), (59) Girard et al. (2011), (60) Gizis et al. (2011a), (61) Gizis et al. (2013), (62) Gizis et al. (2015), (63) Hambly et al. (2001), (64) Harrington et al. (1993), (65) Henry et al. (2006), (66) Hog et al. (2000), (67) Jameson et al. (2008), (68) Kellogg et al. (2016), (69) Kendall et al. (2004), (70) Kendall et al. (2007a), (71) Kirkpatrick et al. (2010), (72) Kirkpatrick et al. (2011), (73) Kirkpatrick et al. (2014), (74) Lawrence et al. (2012), (75) Leggett et al. (2012), (76) Lépine et al. (2002b), (77) Lépine & Shara (2005), (78) Lépine et al. (2009), (79) Lépine & Gaidos (2011), (80) Liu et al. (2011), (81) Liu et al. (2016), (82) Lodieu et al. (2005), (83) Lodieu et al. (2006), (84) Lodieu et al. (2012c), (85) Lodieu et al. (2012b), (86) Lodieu et al. (2013), (87) Lodieu (2013), (88) Lodieu et al. (2014), (89) Luhman et al. (2012), (90) Luhman & Sheppard (2014), (91) Luyten (1979), (92) Manjavacas et al. (2013), (93) Marocco et al. (2010), (94) Marocco et al. (2013), (95) Marsh et al. (2013), (96) McCaughrean et al. (2004), (97) Monet et al. (1992), (98) Monet et al. (2003), (99) Muzic et al. (2012), (100) Phan-Bao et al. (2008), (101) Phan-Bao (2011), (102) Pokorny et al. (2004), (103) Qi et al. (2015), (104) Radigan et al. (2008), (105) Reid (2003), (106) Riedel et al. (2014), (107) Roeser et al. (2010), (108) Sahlmann et al. (2014), (109) Sahlmann et al. (2015), (110) Sahlmann et al. (2016), (111) Salim & Gould (2003), (112) Schilbach et al. (2009), (113) Schmidt et al. (2007), (114) Schmidt et al. (2010), (115) Schneider et al. (2016b), (116) Scholz et al. (2009), (117) Scholz et al. (2014), (118) Schweitzer et al. (1999), (119) Seifahrt et al. (2010), (120) Sheppard & Cushing (2009), (121) Shkolnik et al. (2012), (122) Smart et al. (2013), (123) Smith et al. (2014b), (124) Smith et al. (2014a), (125) Stern et al. (2007), (126) Thompson et al. (2013), (127) Tinney et al. (1995), (128) Tinney (1996), (129) Tinney et al. (2003), (130) van Altena et al. (1995), (131) van Leeuwen (2007), (132) Vrba et al. (2004), (133) Wang et al. (2014b), (134) Weinberger et al. (2016), (135) West et al. (2008), (136) Wright et al. (2013), (137) Zacharias et al. (2005), (138) Zhang et al. (2009), (139) Zhang et al. (2010).

NOTE—This table is available in its entirety in machine-readable form in the online journal. A portion is shown here for guidance regarding its form and content. The full table contains 9888 rows. Columns 2–8 are the same as in Table 1, and are repeated here for reference.

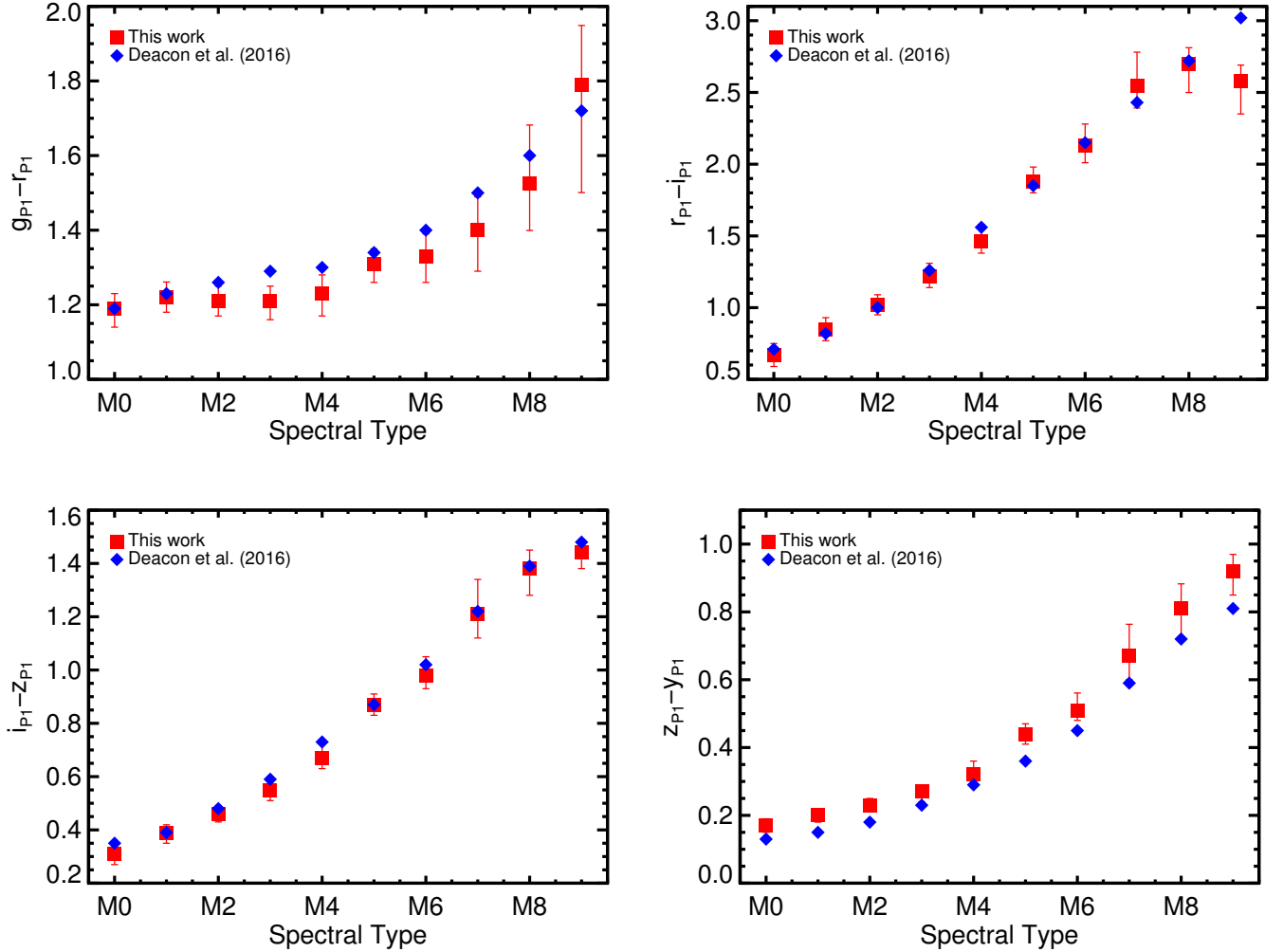


Figure 9. The colors of M dwarfs (median and 68% confidence intervals, red squares) as a function of spectral type, compared with the colors derived from the SED templates (blue diamonds) of Deacon et al. (2016). Our colors are generally quite consistent with those of D16, with small variations resulting from D16’s use of an earlier processing version of PS1 data (PV2) and differences in our input samples. The blueward turn in $r_{P1} - i_{P1}$ at spectral type M9 was not identified by D16 because of their use of $g_{P1} - i_{P1}$ as a proxy for spectral type, which does not clearly distinguish between the late-M spectral subtypes.

Sample (Gagné et al. 2015b), and the Late-Type Extension to MoVeRS (LaTE-MoVeRS; Theissen et al. 2017). Our median proper motion error of 2.9 mas yr^{-1} (Figure 13) is a factor of ≈ 9 smaller than that of S10, ≈ 5 smaller than BDKP, and ≈ 3 smaller than BASS and LaTE-MoVeRS. The high precision of the PS1 measurements is a consequence of the astrometric precision of PS1 and the large number of epochs ($N > 20$ for 90% of proper motions), as well as the long time baseline for objects with a 2MASS position.

Figure 14 compares our PS1 proper motions to those of S10, BDKP, BASS, and LaTE-MoVeRS, each of which shares more than 350 objects in common with our catalog, as well as other literature sources. We note that the overlaps of our PS1 catalog and the other catalogs are predominantly L dwarfs, with very few T dwarfs in common. We also include a comparison to Motion Verified Red Stars (MoVeRS; Theissen et al. 2016). MoVeRS contains mostly earlier-type M dwarfs and hotter stars and has only 132 ultracool dwarfs in common with our PS1 proper motion catalog (mostly late-M dwarfs), so it does not provide as robust a comparison for our full spectral type range as do the other catalogs. Our proper motions are consistent with all of these large catalogs, within 2σ for $\approx 95\%$ of objects in common from BASS, MoVeRS, and LaTE-MoVeRS, and for $\approx 90\%$ of objects in common from BDKP and S10. In addition, we see no systematic offset between our measurements and those from any of the comparison catalogs. We do see a slight offset from the aggregate of other published proper motions (many sources), indicating that proper motions in the

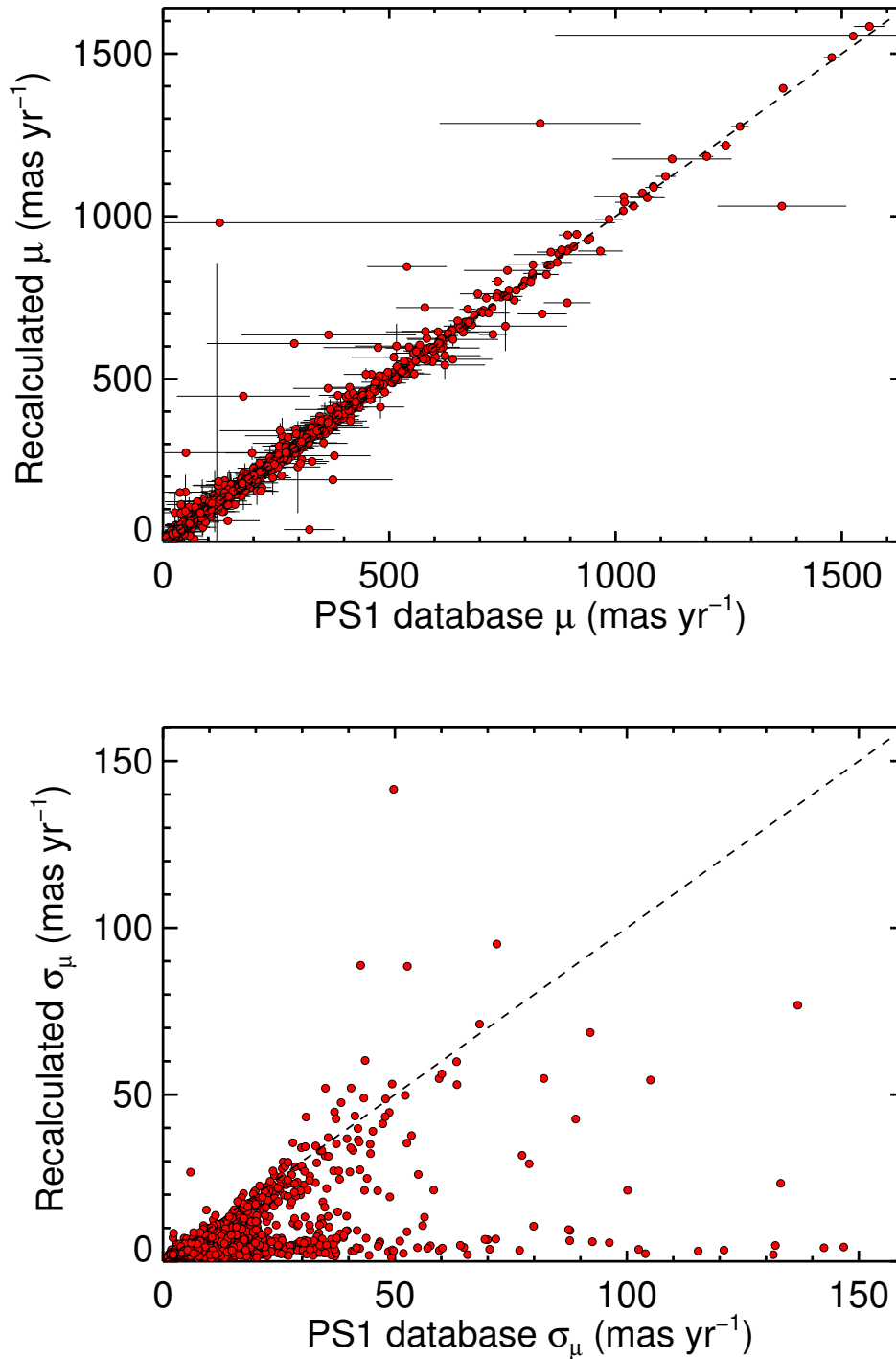


Figure 10. Comparison of the recalculated and PS1 database proper motions (*top*) and errors (*bottom*) for the M6–T9 dwarfs in our PS1 ultracool catalog. The dashed lines indicate equal values. The recalculated proper motions are strongly consistent with the database values, and in the cases of large discrepancy the recalculated proper motions are consistent with literature values (except for six cases of clear contamination by a nearby object). The errors for the recalculated proper motions are lower for 87% of the objects, with a median reduction of 35%.

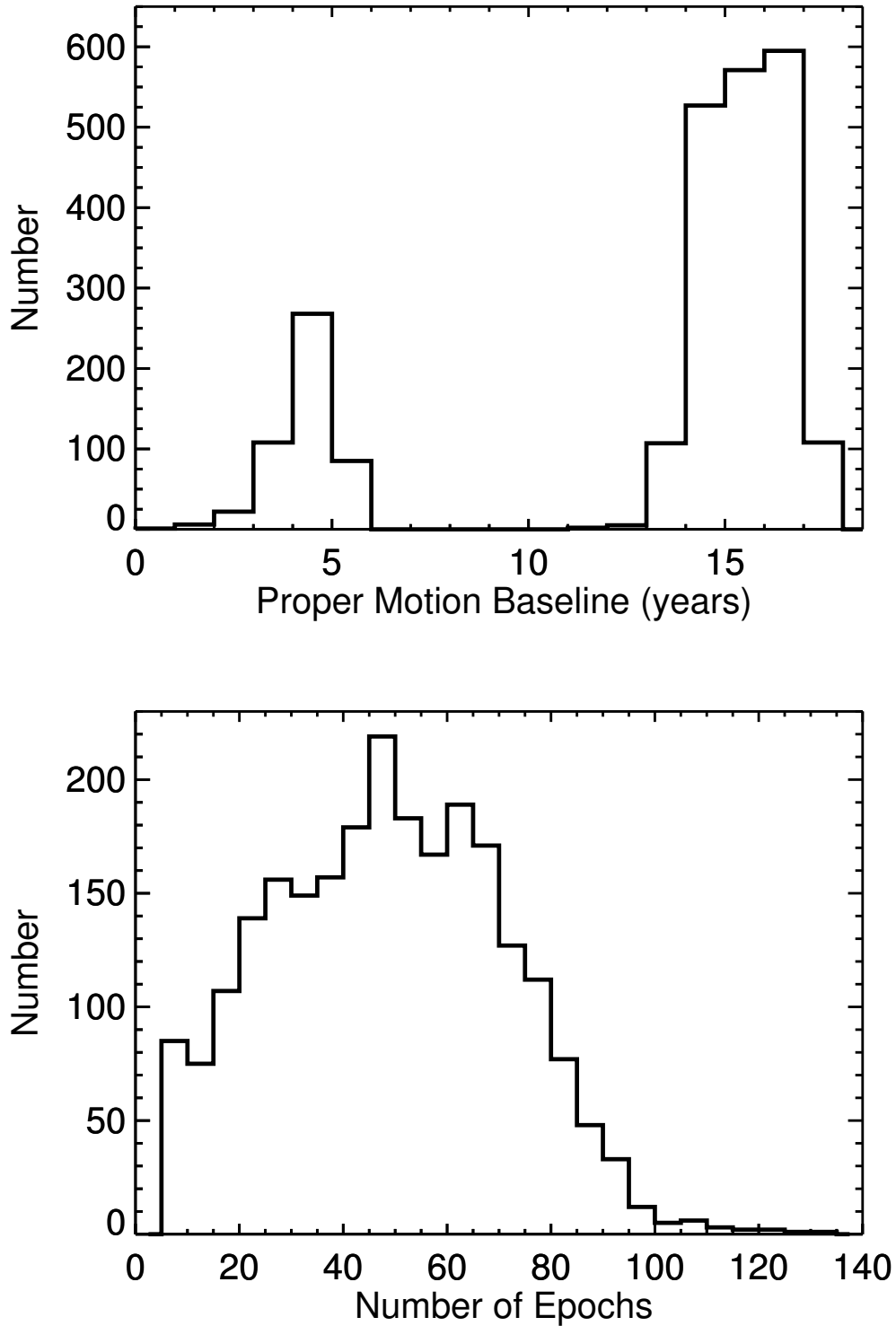


Figure 11. Distributions of the time baselines (*top*) and number of epochs (*bottom*) used to calculate the proper motions of the M6–T9 dwarfs in our PS1 ultracool catalog. For most objects (baselines ≈ 13 –17 years) a 2MASS position was used in the motion fit. Baselines less than 10 years indicate that only PS1 astrometry was used. When available (for about one-quarter of the objects), a *Gaia* DR1 position was also included. We required a minimum of seven epochs in order to calculate a proper motion fit.

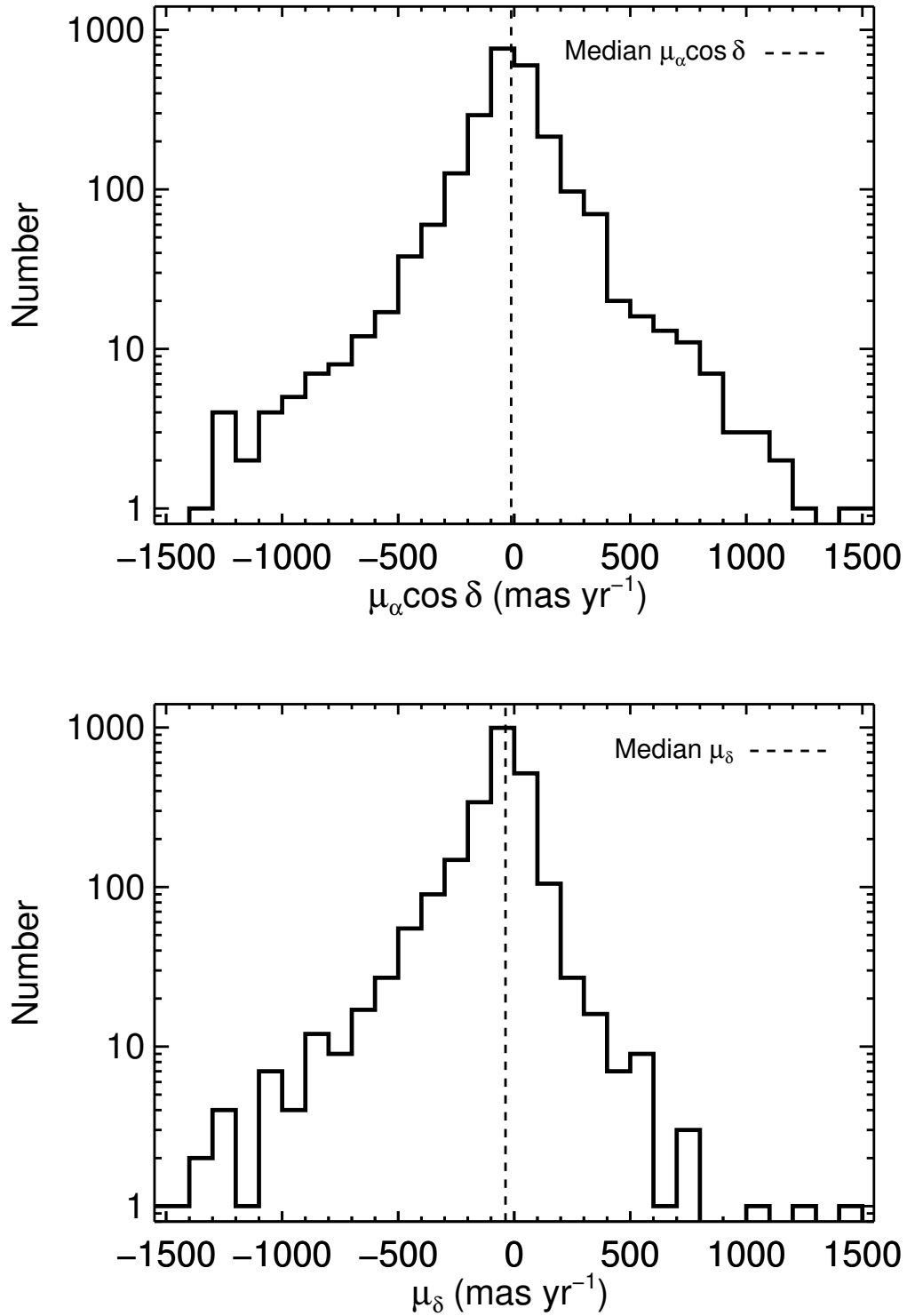


Figure 12. Distributions of the R.A. (*top*) and Decl. (*bottom*) proper motion components of the M6–T9 dwarfs in our PS1 ultracool catalog. The vertical dashed lines indicate the median values. The distributions are similar to those found in previous ultracool surveys (S10, BDKP, BASS, and LaTE-MoVeRS).

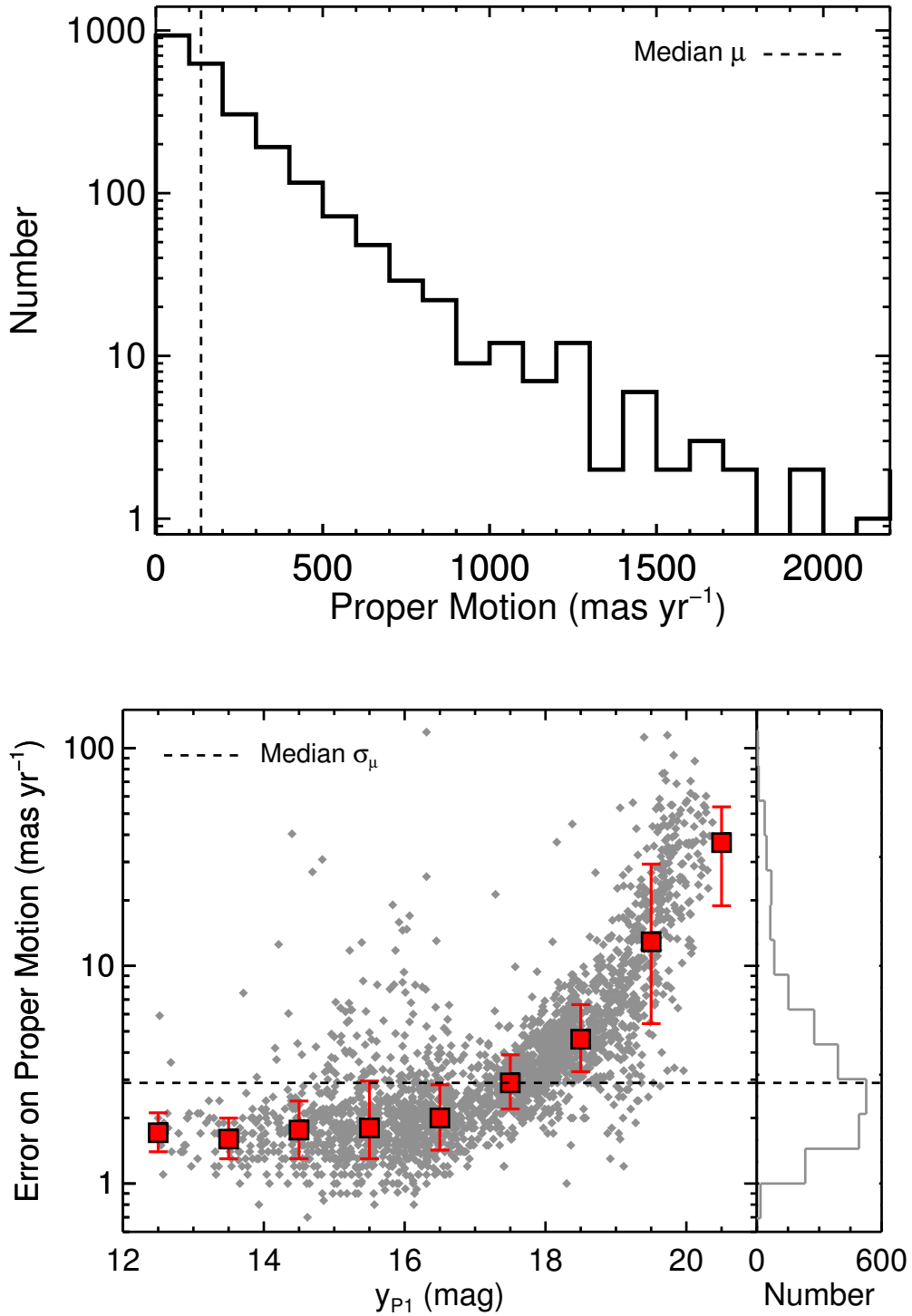


Figure 13. Distribution of the total proper motions (*top*) and proper motion errors as a function of y_{P1} (*bottom*) for the M6–T9 dwarfs in our PS1 ultracool catalog. The dashed lines indicate the median values, including a median error of 2.9 mas yr⁻¹. The large red squares indicate median errors for bins of one magnitude in y_{P1} , with error bars showing 68% confidence limits. Our errors are ≈ 9 times smaller than those in S10, ≈ 5 times smaller than those in BDKP, and ≈ 3 times smaller than those in BASS and LaTE-MoVeRS.

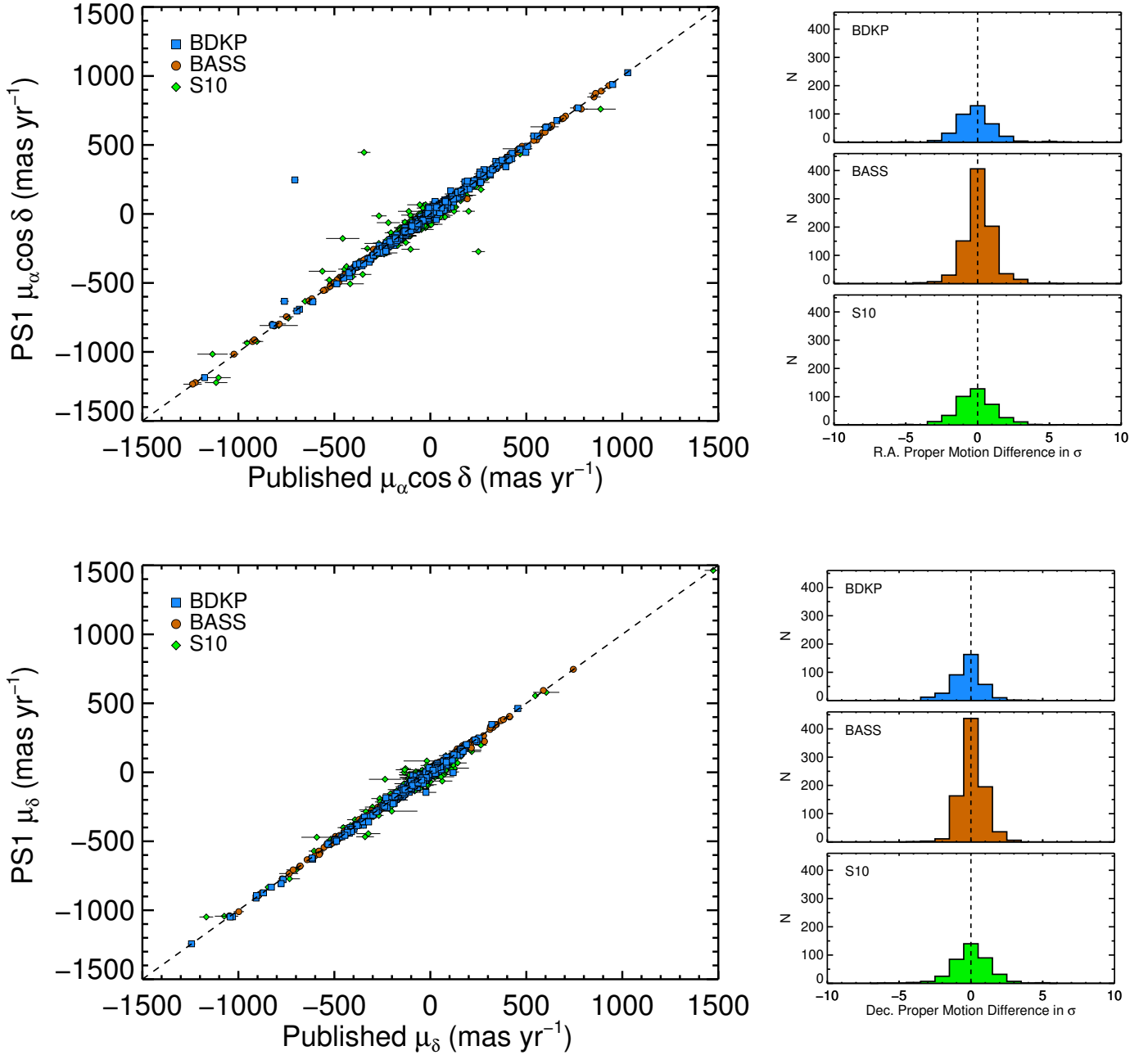


Figure 14. *Left:* Comparison of our PS1 proper motions in R.A. (*top*) and Decl. (*bottom*) with other proper motions from the literature, highlighting the large BDKP, BASS, S10, and (on the following page) MoVeRS and LaTE-MoVeRS catalogs. *Right:* Histograms showing differences in R.A. and Decl. proper motions (computed as PS1 value – literature value). $\approx 95\%$ of are within 2σ of the BASS, MoVeRS, and LaTE-MoVeRS measurements. $\approx 90\%$ of our proper motions are within 2σ of the BDKP and S10 measurements, and within 3σ of other literature values. The histograms show no systematic offset between our PS1 proper motions and those of the S10, BDKP, BASS, MoVeRS, and LaTE-MoVeRS catalogs, but suggest that other literature sources tend to have slightly larger proper motions.

literature tend be slightly larger than those from PS1 and the other large catalogs listed here. Nevertheless, 90% of our values are consistent at 3σ or less with these diverse literature sources.

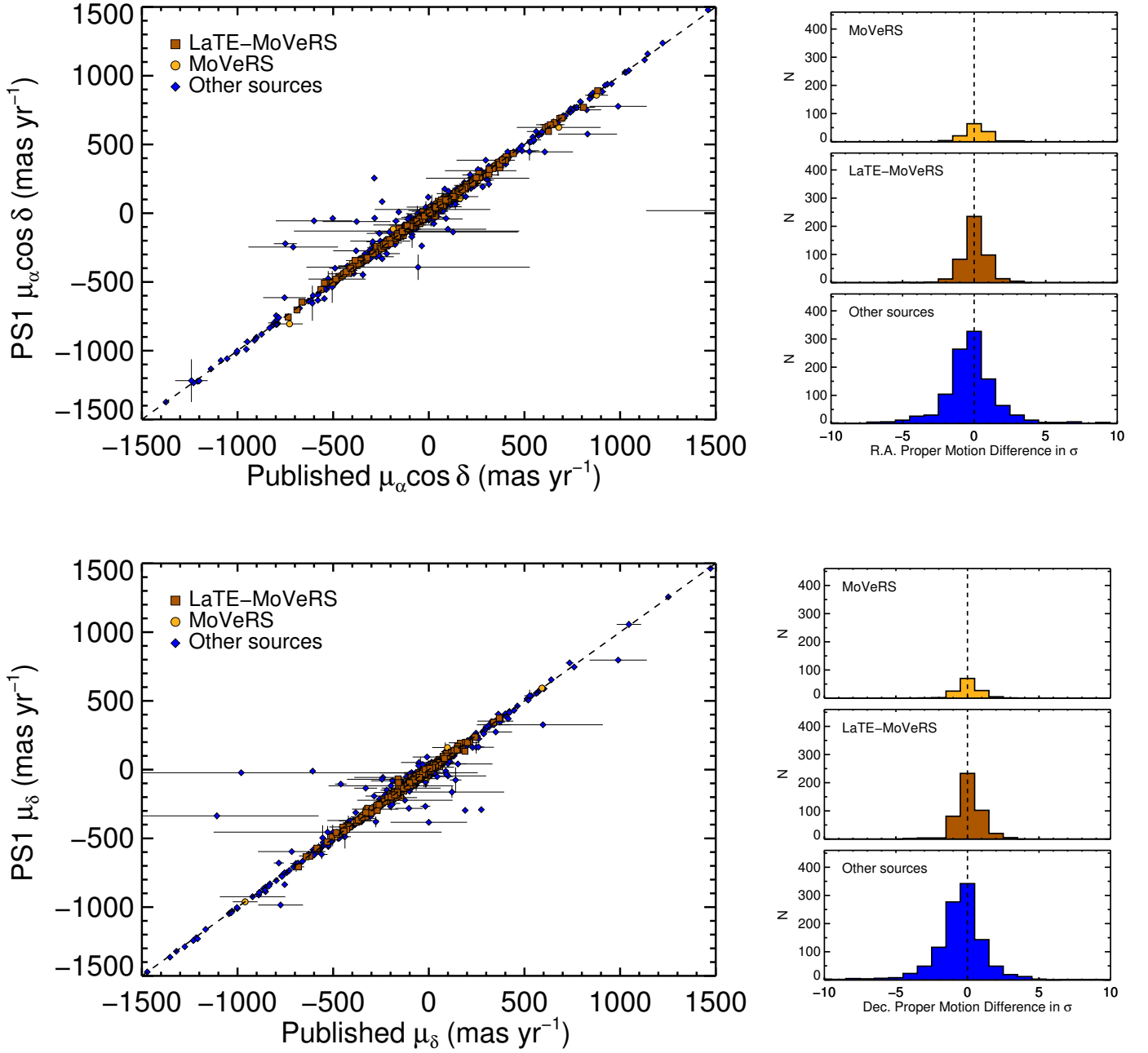


Figure 14. continued.

4.3. Kinematics

Our catalog includes distances and tangential velocities (v_{tan}) for each object with a proper motion (Table 7). We calculated distances from parallaxes in the literature (also in Table 7) when possible. When no parallax was available, we used i_{P1} photometry and the SED templates from D16 for M0–M5 dwarfs. D16 do not quote uncertainties for their SED templates, so based on the apparent scatter in their color transformations we adopt an uncertainty of 0.2 mag, and we add this in quadrature with the photometry errors to determine distance errors. For M6 and later-type dwarfs lacking parallaxes, we use $W2$ photometry with the spectral type–absolute magnitude polynomial and rms from Dupuy & Liu (2012) to calculate photometric distances and errors.

Figure 15 shows the distribution of tangential velocities among our single M6–T9 dwarfs, highlighting the young

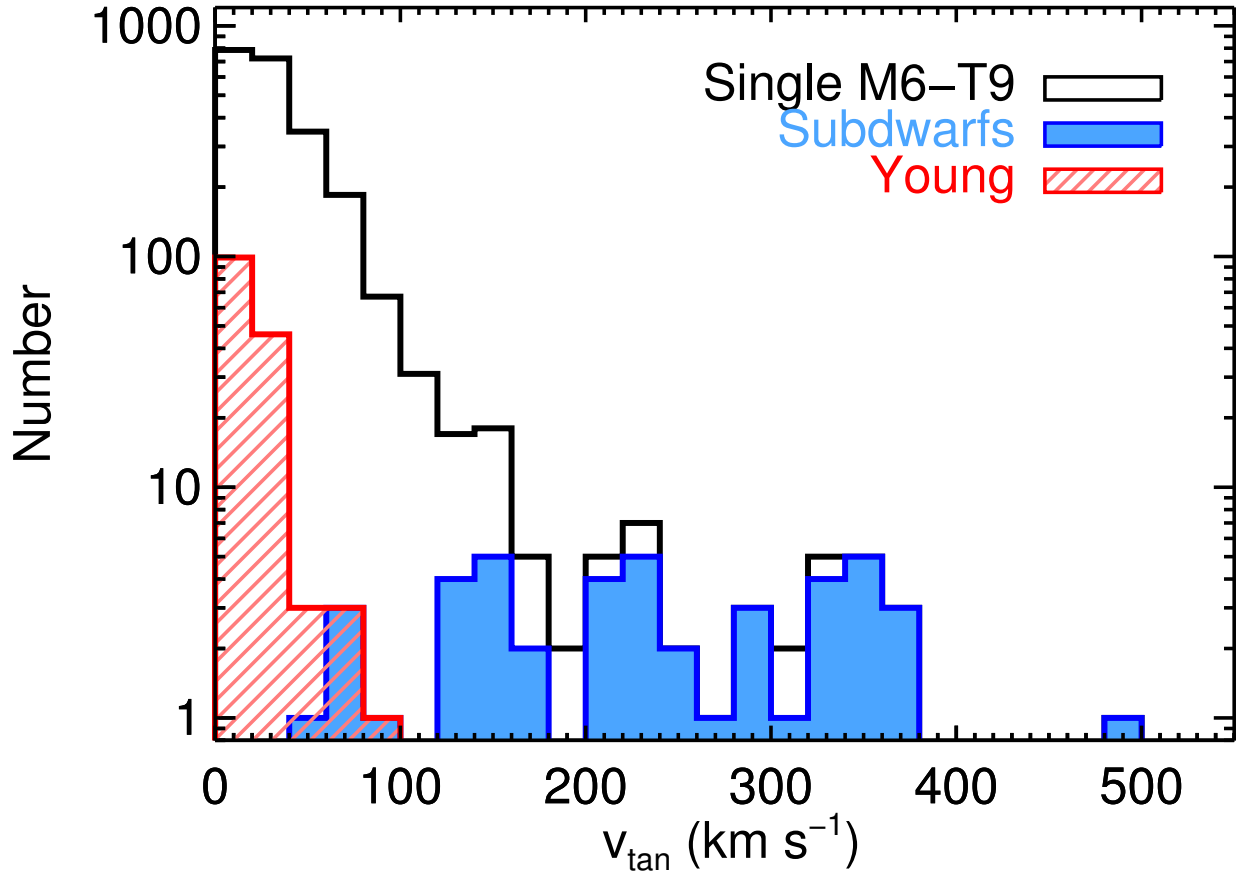


Figure 15. Distribution of tangential velocities for the single M6–T9 dwarfs in our catalog (black outline). Over 90% of objects have $v_{\text{tan}} < 75 \text{ km s}^{-1}$ indicating membership in the thin disk population (Dupuy & Liu 2012). The solid blue histogram highlights the subdwarfs in our catalog, which have the high v_{tan} values typical of members of the older thick disk and halo populations. The hatched red histogram shows young objects in our catalog, which typically have smaller v_{tan} values than field-age objects.

objects (Section 2.5) and subdwarfs. Excluding the young objects and subdwarfs, we find a median of $v_{\text{tan}} = 29 \text{ km s}^{-1}$ and a dispersion of $\sigma_{\text{tan}} = 29 \text{ km s}^{-1}$, consistent with the $v_{\text{tan}} = 26 \text{ km s}^{-1}$ and $\sigma_{\text{tan}} = 25 \text{ km s}^{-1}$ found by Faherty et al. (2009, hereinafter F09) for their 20 pc volume-limited ultracool sample and the $v_{\text{tan}} = 28 \text{ km s}^{-1}$ and $\sigma_{\text{tan}} = 25 \text{ km s}^{-1}$ found by S10 for their L dwarf sample. 90% of our PS1 sample has $v_{\text{tan}} < 75 \text{ km s}^{-1}$, indicating a very high probability of membership in the thin disk population (Dupuy & Liu 2012). 98% of our sample has $v_{\text{tan}} < 200 \text{ km s}^{-1}$, indicating that most of the remaining objects are likely to be in the thick disk population (Dhital et al. 2010; Dupuy & Liu 2012), consistent with the kinematics of the LaTE-MoVeRS sample (Theissen et al. 2017).

Figure 15 demonstrates that the young objects and subdwarfs are members of distinct kinematic populations, corroborating Faherty et al. (2012). Almost all young objects have $v_{\text{tan}} < 60 \text{ km s}^{-1}$, with a median of 16 km s^{-1} and dispersion 13 km s^{-1} , slower than the rest of the thin-disk population. On the other hand, all but one subdwarf have $v_{\text{tan}} > 60 \text{ km s}^{-1}$ and subdwarfs comprise 85% of the objects with $v_{\text{tan}} > 200 \text{ km s}^{-1}$, extending to much higher velocities than other objects. The high v_{tan} of the subdwarfs implies they are likely to be members of the older thick disk or halo ($v_{\text{tan}} > 200 \text{ km s}^{-1}$) populations, as expected for low-metallicity objects.

F09 and S10 used $(J - K_S)_{2\text{MASS}}$ colors, tangential velocities, and velocity dispersions to identify young populations of late-M and L dwarfs with kinematics distinct from the field population. F09 found that red $(J - K_S)_{2\text{MASS}}$ outliers in their sample have lower v_{tan} and σ_{tan} , while blue outliers have higher v_{tan} and σ_{tan} . S10 found evidence that this correlation between $(J - K_S)_{2\text{MASS}}$ and velocity dispersion extends throughout the field L dwarf population and is not limited to outliers. Both studies link the reddest objects to young, low-velocity thin disk populations and the bluest

objects to older, high-velocity thick disk and halo populations.

To examine the relationship between v_{tan} and color differences in our catalog, we use the $\delta_{J-K_S} = [(J - K_S) - (J - K_S)_{\text{med}}] / \sigma_{J-K_S}$ defined by S10, where $(J - K_S)_{\text{med}}$ and σ_{J-K_S} are the median and rms $J - K_S$ colors, respectively, for each spectral type. δ_{J-K_S} therefore gives us a spectral type-independent measurement of the extent to which an object's $J - K_S$ color differs from the median, where a negative δ_{J-K_S} value means the object is bluer than the median color. In Figure 16, we compare our v_{tan} to δ_{J-K_S} for single M6–T9 dwarfs. We also calculated median v_{tan} values for bins of 1σ in δ_{J-K_S} , excluding subdwarfs and young objects from the medians in order to assess the color dependence of v_{tan} for the generic ultracool field population. We show these median v_{tan} values in Figure 16, and we overplot the subdwarfs and young objects for comparison. The blue outliers are mostly subdwarfs with $v_{\text{tan}} > 100 \text{ km s}^{-1}$ while the red outliers are primarily young objects with $v_{\text{tan}} < 10 \text{ km s}^{-1}$, supporting the link between color outliers and age found by F09 and S10. Excluding the subdwarfs and young objects, the field population in our catalog shows a trend toward higher v_{tan} for bluer-than-median objects that is consistent with the σ_{tan} trend identified by S10, but we see no correlation between v_{tan} and $J - K_S$ for redder objects.

We explored whether the trend of higher v_{tan} for bluer-than-median objects held true across the full spectral type range of our sample, because color variations in different spectral types will have different physical causes (e.g., different types of atmospheric clouds). We calculated the same median v_{tan} values for narrower ranges of spectral type (M6–M9.5, L0–L3.5, L4–L8.5, L9–T3.5, and T4–T9). Figure 17 shows these medians, which make clear that the trend toward higher v_{tan} for bluer field objects is a late-M and L dwarf phenomenon but does not apply to T dwarfs.

We also explored the direct relationship between spectral type and tangential velocity, as any correlation would imply an age trend in ultracool spectral types. Figure 18 shows v_{tan} as a function of spectral type. We include median v_{tan} values for bins of two spectral subtypes, excluding subdwarfs and young objects from the medians but overplotting them for reference. We see no evidence for a dependence of v_{tan} on spectral type for ultracool dwarfs.

5. A BINARY DISCOVERED IN PS1

During outlier inspection we discovered a new visual binary. 2MASS J09033514–0637336 (hereinafter 2MASS J0903–0637), first identified and assigned a spectral type of M7 by Cruz et al. (2003), is clearly resolved in individual r_{P1} , i_{P1} , z_{P1} , and y_{P1} warp images, even though it appears in the PS1 database as a single object (see Section 2.6 for a discussion of similar objects). Using the i_{P1} warp images, we measure a difference in flux of $0.10 \pm 0.03 \text{ mag}$, separation of

$1''.14 \pm 0''.02$, and position angle of $239^\circ.3 \pm 1^\circ.0$ for 2MASS J0903–0637. We detect no change in separation or position angle over the four-year span of the PS1 survey. 2MASS J0903–0637 has a proper motion from PS1 of $63.9 \pm 3.4 \text{ mas yr}^{-1}$; if one of the two components were actually a stationary background object, we would see the other component move by $\approx 0''.25$ in four years, a change in position significantly larger than our measurement uncertainties. We therefore conclude that the components are gravitationally bound. Using the i_{P1} photometry for 2MASS J0903–0637 and the absolute magnitude for M7 dwarfs from D16, and correcting for a binary with the measured 0.10 mag flux ratio, we calculate a photometric distance of $60.9 \pm 5.7 \text{ pc}$. This places the projected binary separation at $69.5 \pm 6.6 \text{ AU}$, unusually wide for ultracool field binaries (e.g., Duchêne & Kraus 2013). As expected given the small angular separation, the pair is unresolved in 2MASS and *WISE* images, and therefore was not previously identified as a binary. This was a serendipitous discovery, and we have not undertaken a comprehensive search for more binaries that are newly resolved by PS1 for this catalog.

6. SUMMARY

We present a catalog of 9888 M, L, and T dwarfs with photometry and proper motions from the Pan-STARRS1 3π Survey. This catalog contains all known L and T dwarfs as of 2015 December having well-measured photometry in at least one of the five PS1 bands ($g_{\text{P1}}r_{\text{P1}}i_{\text{P1}}z_{\text{P1}}y_{\text{P1}}$), including 1265 L dwarfs and 352 T dwarfs. The catalog also contains 463 late-M dwarfs chosen to represent the diversity of the nearby population, including low-gravity objects, high proper motion objects, young moving group members, known or suspected binaries, and wide companions to more massive stars, along with a large sample of 7808 field M dwarfs identified by SDSS. We cross-matched our catalog with 2MASS, AllWISE, and *Gaia* DR1 to obtain photometry spanning 0.55 to $12 \mu\text{m}$. We carefully vetted the detections in PS1, 2MASS, and AllWISE to ensure their association with previously identified M, L, and T dwarfs.

We use two types of photometry from PS1 in our catalog: chip photometry (highest accuracy) for most objects and warp photometry (greater depth) for faint, slow-moving objects. We identified a number of false detections (i.e., measurements of background noise) at the warp limiting magnitude for objects in our catalog, and we develop a method for screening warp detections to ensure they are real.

We use the photometry along with parallaxes from the literature to create empirical SEDs for field ultracool dwarfs

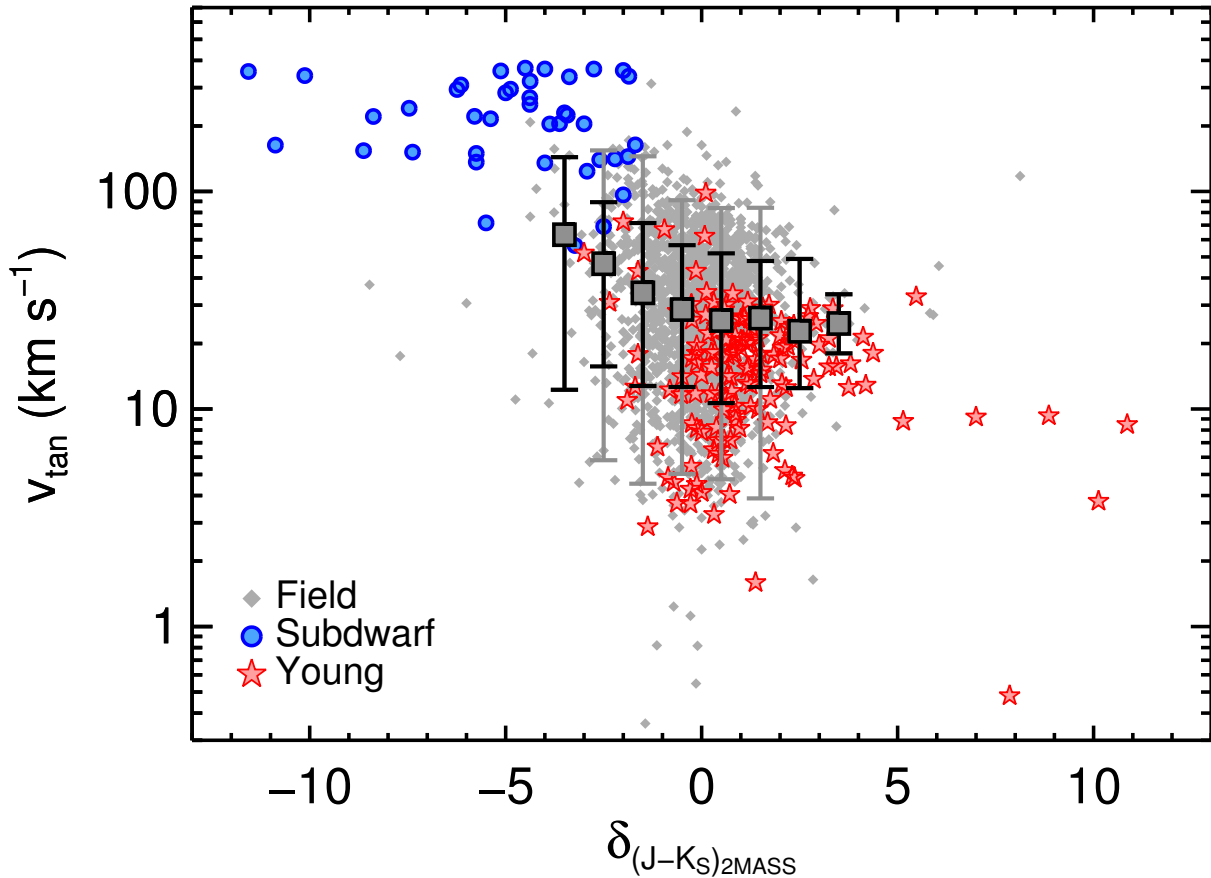


Figure 16. Tangential velocity as a function of $\delta_{(J-K_S)_{2MASS}}$ (the number of standard deviations by which an object’s $(J - K_S)_{2MASS}$ color differs from the median $(J - K_S)_{2MASS}$ for its spectral type) for single M6–T9 dwarfs. The large gray squares indicate median v_{tan} values for 1σ bins of δ_{J-K_S} , with dark and light error bars marking 68% and 95% confidence intervals, respectively. The medians do not include subdwarfs or young objects, but we overplot these with blue circles and red stars, respectively, for comparison. The blue end of the field population tends toward higher v_{tan} , but on the red end there is no correlation with v_{tan} .

covering g_{P1} to $W3$ bands. We determine typical colors of M0–T9 dwarfs, and we present numerous color-spectral type and color-color diagrams, along with median colors for each spectral subtype. We separate binaries, young objects, and subdwarfs from the rest of the field population, and we compare the colors of the different groups. Our catalog includes 494 L dwarfs detected in r_{P1} , the largest sample of L dwarfs detected in this optical band. r_{P1} L dwarf colors show striking features, including a sharp blueward turn at the M/L transition due to decreasing TiO absorption in r_{P1} , and a handful of young objects with colors bluer than the median for their spectral type.

We calculate proper motions for our catalog using multiple-epoch astrometry from PS1 along with 2MASS and *Gaia* when available. Our method allows us to link the epochs of fast-moving objects that are split into more than one “object” in PS1, improving the precision of our proper motions compared to the PS1 database for 87% of the M6 and later dwarfs in our catalog and producing measurements for 63 objects lacking proper motions in PS1. Our catalog contains proper motions for 9770 objects with a median precision of 2.9 mas yr^{-1} (a factor of ≈ 3 – 10 improvement over previous large catalogs), tied to the *Gaia* DR1 reference frame. The catalog includes proper motions for a total of 2405 M6–T9 dwarfs, including 406 objects with no previously published values and 1176 measurements that improve upon previous literature values. Our catalog incorporates the largest set of homogeneous proper motions for L and T dwarfs published to date.

We assess the kinematics of the late-M, L, and T dwarfs in our sample and find evidence that bluer late-M and L dwarfs with field ages (i.e., not subdwarfs) have higher tangential velocities, consistent with the trend towards

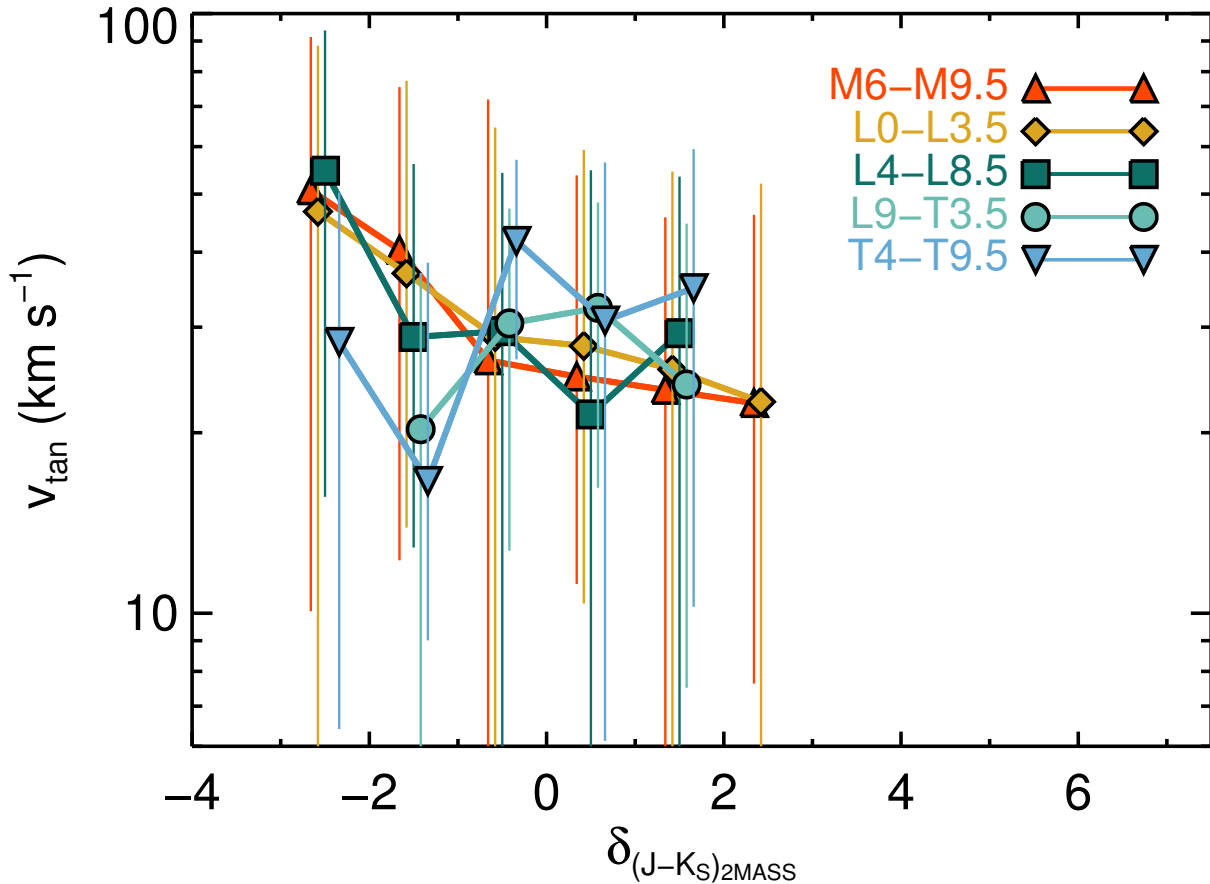


Figure 17. Median tangential velocities for 1σ bins of δ_{J-K_S} (same as in Figure 16), split into five spectral type ranges (see legend). The δ_{J-K_S} bins are the same for each spectral type range; the median symbols have been offset slightly to improve visibility. The colored lines indicate the 68% confidence intervals for each δ_{J-K_S} bin. The trend toward higher tangential velocities for bluer objects holds true for the late-M and L dwarfs, but not for T dwarfs.

higher σ_{tan} for bluer L dwarfs found by S10. More work is needed using well-defined (i.e., volume-limited) samples with accurate distances to precisely characterize the relationship between colors and kinematics for nearby ultracool dwarfs.

Tables in this paper are available in electronic form from the online journal and at http://www.ifa.hawaii.edu/users/wbest/Will_Best/PS1_MLT_Dwarfs.html.

We thank the anonymous referee for detailed comments that improved the paper in several significant ways, and Gabriel Bihain for helpful comments on the catalog. The Pan-STARRS1 Surveys (PS1) have been made possible through contributions of the Institute for Astronomy, the University of Hawaii, the Pan-STARRS Project Office, the Max-Planck Society and its participating institutes, the Max Planck Institute for Astronomy, Heidelberg and the Max Planck Institute for Extraterrestrial Physics, Garching, The Johns Hopkins University, Durham University, the University of Edinburgh, Queen’s University Belfast, the Harvard-Smithsonian Center for Astrophysics, the Las Cumbres Observatory Global Telescope Network Incorporated, the National Central University of Taiwan, the Space Telescope Science Institute, the National Aeronautics and Space Administration under Grant No. NNX08AR22G issued through the Planetary Science Division of the NASA Science Mission Directorate, the National Science Foundation under Grant No. AST-1238877, the University of Maryland, Eotvos Lorand University (ELTE), and the Los Alamos National Laboratory. This publication makes use of data products from the Two Micron All Sky Survey, which is a joint project of the University of Massachusetts and the Infrared Processing and Analysis Center/California Institute of Technology,

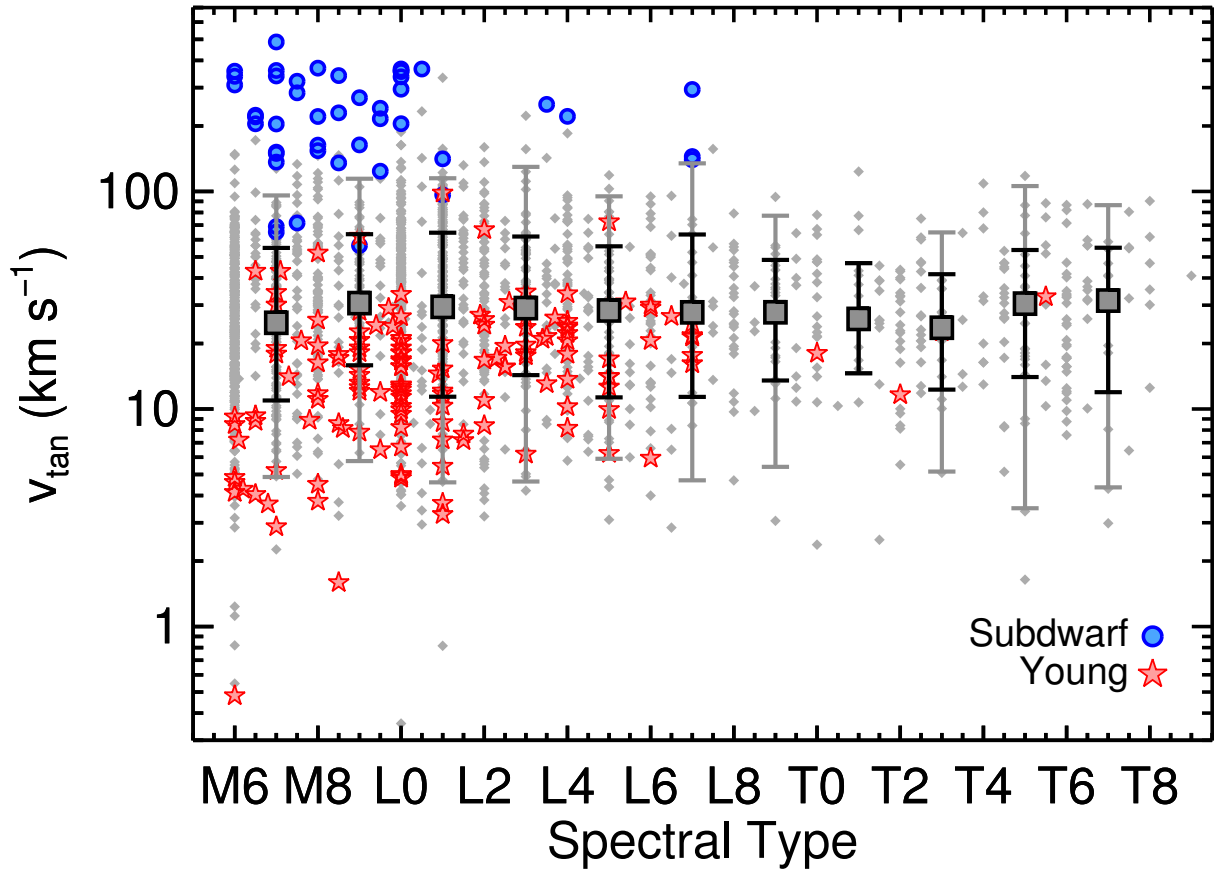


Figure 18. Tangential velocity as a function of spectral type for the single M6–T9 dwarfs in our catalog, using the same format as in Figure 16. Large gray symbols indicate median tangential velocities for bins of two spectral subtypes, excluding subdwarfs and young objects. We find no correlation between spectral type and tangential velocity in our catalog.

funded by the National Aeronautics and Space Administration and the National Science Foundation. This publication makes use of data products from the Wide-field Infrared Survey Explorer, which is a joint project of the University of California, Los Angeles, and the Jet Propulsion Laboratory/California Institute of Technology, and NEOWISE, which is a project of the Jet Propulsion Laboratory/California Institute of Technology. *WISE* and NEOWISE are funded by the National Aeronautics and Space Administration. This work has made use of data from the European Space Agency (ESA) mission *Gaia* (<http://www.cosmos.esa.int/gaia>), processed by the *Gaia* Data Processing and Analysis Consortium (DPAC, <http://www.cosmos.esa.int/web/gaia/dpac/consortium>). Funding for the DPAC has been provided by national institutions, in particular the institutions participating in the *Gaia* Multilateral Agreement. This research has made use of NASA’s Astrophysical Data System, the UKIDSS data products, and the Database of Ultracool Parallaxes, maintained by Trent Dupuy at <https://www.cfa.harvard.edu/~tdupuy/plx>. This research has made extensive use of the SIMBAD and Vizier databases operated at CDS, Strasbourg, France. This work was greatly facilitated by many features of the TOPCAT software written by Mark Taylor (<http://www.starlink.ac.uk/topcat/>). WMJB received support from NSF grant AST09-09222. WMBJ, MCL, and EAM received support from NSF grant AST-1313455.

REFERENCES

- Aberasturi, M., Burgasser, A. J., Mora, A., et al. 2014, *AJ*, 148,
 Aganze, C., Burgasser, A. J., Faherty, J. K., et al. 2016, *AJ*, 151,
 46
 Albert, L., Artigau, E., Delorme, P., et al. 2011, *AJ*, 141, 203

- Allen, P. R., Burgasser, A. J., Faherty, J. K., & Kirkpatrick, J. D. 2012, *AJ*, 144, 62
- Allen, P. R., Koerner, D. W., McElwain, M. W., Cruz, K. L., & Reid, I. N. 2007, *AJ*, 133, 971
- Allen, P. R., Koerner, D. W., Reid, I. N., & Trilling, D. E. 2005, *ApJ*, 625, 385
- Aller, K. M., Kraus, A. L., Liu, M. C., et al. 2013, *ApJ*, 773, 63
- Aller, K. M., Liu, M. C., Magnier, E. A., et al. 2016, *ApJ*, 821, 120
- Allers, K. N., & Liu, M. C. 2013a, *ApJ*, 772, 79
- Allers, K. N., & Liu, M. C. 2013b, in *Brown Dwarfs Come of Age*, *Mem. S.A.It.*, 84, 1089
- Allers, K. N., Liu, M. C., Dupuy, T. J., & Cushing, M. C. 2010, *ApJ*, 715, 561
- Allers, K. N., Liu, M. C., Shkolnik, E. L., et al. 2009, *ApJ*, 697, 824
- Alves de Oliveira, C., Moraux, E., Bouvier, J., et al. 2013, *A&A*, 549, 123
- Andrei, A. H., Smart, R. L., Penna, J. L., et al. 2011, *AJ*, 141, 54
- Artigau, E., Doyon, R., Lafreniere, D., et al. 2006, *ApJ*, 651, L57
- Artigau, E., Lafreniere, D., Doyon, R., et al. 2011, *ApJ*, 739, 48
- Bardalez Gagliuffi, D. C., Gelino, C. R., & Burgasser, A. J. 2015, *AJ*, 150, 163
- Bardalez Gagliuffi, D. C., Burgasser, A. J., Gelino, C. R., et al. 2014, *ApJ*, 794, 143
- Baron, F., Lafreniere, D., Artigau, E., et al. 2015, *ApJ*, 802, 37
- Barrado Y Navascués, D., Zapatero Osorio, M. R., Martín, E. L., et al. 2002, *A&A*, 393, L85
- Bartlett, J. L. 2007, PhD Thesis
- Basri, G., Mohanty, S., Allard, F., et al. 2000, *ApJ*, 538, 363
- Beamín, J. C., Minniti, D., Gromadzki, M., et al. 2013, *A&A*, 557, L8
- Becklin, E. E., & Zuckerman, B. 1988, *Nature*, 336, 656
- Béjar, V. J. S., Zapatero Osorio, M. R., Pérez Garrido, A., et al. 2008, *ApJ*, 673, L185
- Bernard, E. J., Ferguson, A. M. N., Schlafly, E. F., et al. 2014, *MNRAS*, 442, 2999
- Bessell, M. S. 1991, *AJ*, 101, 662
- Best, W. M. J., Liu, M. C., Dupuy, T. J., & Magnier, E. A. 2017a, *ApJL*, 843, L4
- Best, W. M. J., Liu, M. C., Magnier, E. A., et al. 2013, *ApJ*, 777, 84
- . 2015, *ApJ*, 814, 118
- . 2017b, *ApJ*, 837, 95
- Bihain, G., Rebolo, R., Zapatero Osorio, M. R., Béjar, V. J. S., & Caballero, J. A. 2010, *A&A*, 519, 93
- Bihain, G., Scholz, R.-D., Storm, J., & Schnurr, O. 2013, *A&A*, 557, 43
- Bochanski, J. J., Hawley, S. L., Covey, K. R., et al. 2010, *AJ*, 139, 2679
- Boeshaar, P. C. 1976, Ph.D. Thesis Ohio State Univ.
- Boudreault, S., & Lodieu, N. 2013, *MNRAS*, 434, 142
- Bouvier, J., Kendall, T., Meeus, G., et al. 2008, *A&A*, 481, 661
- Bouy, H., Brandner, W., Martín, E. L., et al. 2003, *AJ*, 126, 1526
- Bouy, H., Bertin, E., Sarro, L. M., et al. 2015, *A&A*, 577, A148
- Bowler, B. P., Liu, M. C., & Dupuy, T. J. 2010, *ApJ*, 710, 45
- Bryja, C., Humphreys, R. M., & Jones, T. J. 1994, *AJ*, 107, 246
- Bryja, C., Jones, T. J., Humphreys, R. M., et al. 1992, *Astrophysical Journal*, 388, L23
- Burgasser, A. J. 2004, *ApJ*, 614, L73
- . 2007, *AJ*, 134, 1330
- Burgasser, A. J., Cruz, K. L., Cushing, M., et al. 2010a, *ApJ*, 710, 1142
- Burgasser, A. J., Cruz, K. L., & Kirkpatrick, J. D. 2007, *ApJ*, 657, 494
- Burgasser, A. J., Dhital, S., & West, A. A. 2009a, *AJ*, 138, 1563
- Burgasser, A. J., Geballe, T. R., Leggett, S. K., Kirkpatrick, J. D., & Golimowski, D. A. 2006a, *ApJ*, 637, 1067
- Burgasser, A. J., & Kirkpatrick, J. D. 2006, *ApJ*, 645, 1485
- Burgasser, A. J., Kirkpatrick, J. D., Cruz, K. L., et al. 2006b, *ApJS*, 166, 585
- Burgasser, A. J., Kirkpatrick, J. D., Liebert, J., & Burrows, A. S. 2003a, *ApJ*, 594, 510
- Burgasser, A. J., Kirkpatrick, J. D., & Lowrance, P. J. 2005a, *AJ*, 129, 2849
- Burgasser, A. J., Kirkpatrick, J. D., McElwain, M. W., et al. 2003b, *AJ*, 125, 850
- Burgasser, A. J., Kirkpatrick, J. D., Reid, I. N., et al. 2003c, *ApJ*, 586, 512
- Burgasser, A. J., Liu, M. C., Ireland, M. J., Cruz, K. L., & Dupuy, T. J. 2008a, *ApJ*, 681, 579
- Burgasser, A. J., Looper, D. L., Kirkpatrick, J. D., Cruz, K. L., & Swift, B. J. 2008b, *ApJ*, 674, 451
- Burgasser, A. J., Looper, D. L., & Rayner, J. T. 2010b, *AJ*, 139, 2448
- Burgasser, A. J., Luk, C., Dhital, S., et al. 2012, *ApJ*, 757, 110
- Burgasser, A. J., & McElwain, M. W. 2006, *AJ*, 131, 1007
- Burgasser, A. J., McElwain, M. W., & Kirkpatrick, J. D. 2003d, *AJ*, 126, 2487
- Burgasser, A. J., McElwain, M. W., Kirkpatrick, J. D., et al. 2004, *AJ*, 127, 2856
- Burgasser, A. J., Reid, I. N., Leggett, S. K., et al. 2005b, *ApJ*, 634, L177
- Burgasser, A. J., Sitarski, B. N., Gelino, C. R., Logsdon, S. E., & Perrin, M. D. 2011, *ApJ*, 739, 49
- Burgasser, A. J., Tinney, C. G., Cushing, M. C., et al. 2008c, *ApJ*, 689, L53
- Burgasser, A. J., Witte, S., Helling, C., et al. 2009b, *ApJ*, 697, 148
- Burgasser, A. J., Kirkpatrick, J. D., Brown, M. E., et al. 1999, *ApJ*, 522, L65
- Burgasser, A. J., Wilson, J. C., Kirkpatrick, J. D., et al. 2000a, *AJ*, 120, 1100
- Burgasser, A. J., Kirkpatrick, J. D., Cutri, R. M., et al. 2000b, *ApJ*, 531, L57
- Burgasser, A. J., Kirkpatrick, J. D., Brown, M. E., et al. 2002, *ApJ*, 564, 421
- Burgasser, A. J., Kirkpatrick, J. D., Burrows, A. S., et al. 2003e, *ApJ*, 592, 1186
- Burgasser, A. J., Gillon, M., Melis, C., et al. 2015, *AJ*, 149, 104
- Burgasser, A. J., Lopez, M. A., Mamajek, E. E., et al. 2016, *ApJ*, 820, 32
- Burningham, B., Pinfield, D. J., Lucas, P. W., et al. 2010a, *MNRAS*, 406, 1885
- Burningham, B., Leggett, S. K., Lucas, P. W., et al. 2010b, *MNRAS*, 404, 1952
- Burningham, B., Lucas, P. W., Leggett, S. K., et al. 2011, *MNRASL*, 414, L90
- Burningham, B., Cardoso, C. V., Smith, L., et al. 2013, *MNRAS*, 433, 457
- Burrows, A. S., Sudarsky, D., & Hubeny, I. 2006, *ApJ*, 640, 1063
- Caballero, J. A. 2007, *ApJ*, 667, 520
- Cardoso, C. V., Burningham, B., Smart, R. L., et al. 2015, *MNRAS*, 450, 2486
- Carrasco, J. M., Evans, D. W., Montegriffo, P., et al. 2016, *A&A*, 595, A7
- Casewell, S. L., Jameson, R. F., & Burleigh, M. R. 2008, *MNRAS*, 390, 1517
- Castro, P. J., & Gizis, J. E. 2012, *ApJ*, 746, 3
- . 2016, *ApJ*, 816, 78
- Castro, P. J., Gizis, J. E., Harris, H. C., et al. 2013, *ApJ*, 776, 126

- Chambers, K. C., Magnier, E. A., Metcalfe, N., et al. 2017, in preparation, arXiv:1612.05560
- Chiu, K., Fan, X., Leggett, S. K., et al. 2006, *AJ*, 131, 2722
- Chiu, K., Liu, M. C., Jiang, L., et al. 2008, *MNRAS*, 385, L53
- Close, L. M., Potter, D., Brandner, W., et al. 2002a, *ApJ*, 566, 1095
- Close, L. M., Siegler, N., Freed, M., & Biller, B. A. 2003, *ApJ*, 587, 407
- Close, L. M., Siegler, N., Potter, D., Brandner, W., & Liebert, J. 2002b, *ApJ*, 567, L53
- Cohen, M., Wheaton, W. A., & Megeath, S. T. 2003, *AJ*, 126, 1090
- Costa, E., Méndez, R. A., Jao, W. C., et al. 2005, *AJ*, 130, 337
- , 2006, *AJ*, 132, 1234
- Crifo, F., Phan-Bao, N., Delfosse, X., et al. 2005, *A&A*, 441, 653
- Cruz, K. L., Burgasser, A. J., Reid, I. N., & Liebert, J. 2004, *ApJ*, 604, L61
- Cruz, K. L., Kirkpatrick, J. D., & Burgasser, A. J. 2009, *AJ*, 137, 3345
- Cruz, K. L., & Reid, I. N. 2002, *AJ*, 123, 2828
- Cruz, K. L., Reid, I. N., Liebert, J., Kirkpatrick, J. D., & Lowrance, P. J. 2003, *AJ*, 126, 2421
- Cruz, K. L., Reid, I. N., Kirkpatrick, J. D., et al. 2007, *AJ*, 133, 439
- Cushing, M. C., Kirkpatrick, J. D., Gelino, C. R., et al. 2014, *AJ*, 147, 113
- Cushing, M. C., & Vacca, W. D. 2006, *AJ*, 131, 1797
- Cushing, M. C., Kirkpatrick, J. D., Gelino, C. R., et al. 2011, *ApJ*, 743, 50
- Cutri, R. M., Skrutskie, M. F., Van Dyk, S., et al. 2003, *VizieR On-line Data Catalog*, II/246, 0
- , 2006, Explanatory Supplement to the 2MASS All Sky Data Release
- Cutri, R. M., Wright, E. L., Conrow, T., et al. 2014, *VizieR On-line Data Catalog*, II/328, 0
- Dahn, C. C., Liebert, J., & Harrington, R. S. 1986, *AJ*, 91, 621
- Dahn, C. C., Harris, H. C., Vrba, F. J., et al. 2002, *AJ*, 124, 1170
- Dahn, C. C., Harris, H. C., Levine, S. E., et al. 2008, *ApJ*, 686, 548
- Dawson, P., Scholz, A., Ray, T. P., et al. 2014, *MNRAS*, 442, 1586
- Day-Jones, A. C., Marocco, F., Pinfield, D. J., et al. 2013, *MNRAS*, 430, 1171
- Deacon, N. R., & Hambly, N. C. 2007, *A&A*, 468, 163
- Deacon, N. R., Hambly, N. C., & Cooke, J. A. 2005, *A&A*, 435, 363
- Deacon, N. R., Hambly, N. C., King, R. R., & McCaughrean, M. J. 2009, *MNRAS*, 394, 857
- Deacon, N. R., Liu, M. C., Magnier, E. A., et al. 2011, *AJ*, 142, 77
- , 2012a, *ApJ*, 755, 94
- , 2012b, *ApJ*, 757, 100
- , 2014, *ApJ*, 792, 119
- Deacon, N. R., Kraus, A. L., Mann, A. W., et al. 2016, *MNRAS*, 455, 4212
- Deacon, N. R., Magnier, E. A., Liu, M. C., et al. 2017a, *MNRAS*, 467, 1126
- Deacon, N. R., Magnier, E. A., Best, W. M. J., et al. 2017b, *MNRAS*, 468, 3499
- Delfosse, X., Tinney, C. G., Forveille, T., et al. 1999, *A&AS*, 135, 41
- , 1997, *A&A*, 327, L25
- Delorme, P., Willott, C. J., Forveille, T., et al. 2008, *A&A*, 484, 469
- Dhital, S., West, A. A., Stassun, K. G., & Bochanski, J. J. 2010, *AJ*, 139, 2566
- Dieterich, S. B., Henry, T. J., Jao, W.-C., et al. 2014, *AJ*, 147, 94
- Dittmann, J. A., Irwin, J. M., Charbonneau, D., & Berta-Thompson, Z. K. 2014, *ApJ*, 784, 156
- Dobbie, P. D., Kenyon, F., Jameson, R. F., et al. 2002, *MNRAS*, 329, 543
- Duchêne, G., & Kraus, A. 2013, *ARAA*, 51, 269
- Dupuy, T. J., Forbrich, J., Rizzuto, A., et al. 2016, *ApJ*, 827, 23
- Dupuy, T. J., & Kraus, A. L. 2013, *Science*, 341, 1492
- Dupuy, T. J., & Liu, M. C. 2012, *ApJS*, 201, 19
- , 2017, *ApJS*, 231, 15
- Dupuy, T. J., Liu, M. C., & Bowler, B. P. 2009, *ApJ*, 706, 328
- Dupuy, T. J., Liu, M. C., Bowler, B. P., et al. 2010, *ApJ*, 721, 1725
- Dupuy, T. J., Liu, M. C., Leggett, S. K., et al. 2015, *ApJ*, 805, 56
- Epchtein, N., Deul, E., Derriere, S., et al. 1999, *A&A*, 349, 236
- Faherty, J. K., Burgasser, A. J., Cruz, K. L., et al. 2009, *AJ*, 137, 1
- Faherty, J. K., Burgasser, A. J., West, A. A., et al. 2010, *AJ*, 139, 176
- Faherty, J. K., Rice, E. L., Cruz, K. L., Mamajek, E. E., & Núñez, A. 2013, *AJ*, 145, 2
- Faherty, J. K., Burgasser, A. J., Walter, F. M., et al. 2012, *ApJ*, 752, 56
- Faherty, J. K., Riedel, A. R., Cruz, K. L., et al. 2016, *ApJS*, 225, 10
- Fan, X., Knapp, G. R., Strauss, M. A., et al. 2000, *AJ*, 119, 928
- Finch, C. T., & Zacharias, N. 2016, *AJ*, 151, 160
- Folkes, S. L., Pinfield, D. J., Jones, H. R. A., et al. 2012, *MNRAS*, 427, 3280
- Forbrich, J., Dupuy, T. J., Reid, M. J., et al. 2016, *ApJ*, 827, 22
- Forveille, T., Beuzit, J. L., Delorme, P., et al. 2005, *A&A*, 435, L5
- Freed, M., Close, L. M., & Siegler, N. 2003, *ApJ*, 584, 453
- Gagné, J., Burgasser, A. J., Faherty, J. K., et al. 2015a, *ApJL*, 808, L20
- Gagné, J., Lafreniere, D., Doyon, R., et al. 2014a, *ApJL*, 792, L17
- Gagné, J., Lafreniere, D., Doyon, R., Malo, L., & Artigau, E. 2014b, *ApJ*, 783, 121
- , 2015b, *ApJ*, 798, 73
- Gagné, J., Faherty, J. K., Cruz, K. L., et al. 2015c, *ApJS*, 219, 33
- Gagné, J., Faherty, J. K., Mamajek, E. E., et al. 2017, *ApJS*, 228, 18
- Gaia Collaboration, Brown, A. G. A., Vallenari, A., et al. 2016a, *A&A*, 595, A2
- Gaia Collaboration, Prusti, T., de Bruijne, J. H. J., et al. 2016b, *A&A*, 595, A1
- Gatewood, G., & Coban, L. 2009, *AJ*, 137, 402
- Gauza, B., Bejar, V. J. S., Pérez Garrido, A., et al. 2015, *ApJ*, 804, 96
- Gauza, B., Béjar, V. J. S., Rebolo, R., et al. 2012, *MNRAS*, 427, 2457
- Gawroński, M. P., Goździewski, K., & Katarzyński, K. 2016, *MNRAS*
- Geballe, T. R., Knapp, G. R., Leggett, S. K., et al. 2002, *ApJ*, 564, 466
- Geißler, K., Metchev, S. A., Kirkpatrick, J. D., Berriman, G. B., &Looper, D. L. 2011, *ApJ*, 732, 56
- Gelino, C. R., Kirkpatrick, J. D., Cushing, M. C., et al. 2011, *AJ*, 142, 57
- Gelino, C. R., Smart, R. L., Marocco, F., et al. 2014, *AJ*, 148, 6
- Giampapa, M. S., & Liebert, J. 1986, *ApJ*, 305, 784
- Giclas, H. L., Burnham, R., & Thomas, N. G. 1967, *Bulletin / Lowell Observatory* ; no. 138, 7
- Gillon, M., Jehin, E., Lederer, S. M., et al. 2016, *Nature*, 533, 221
- Gilmore, G., Reid, I. N., & Hewett, P. 1985, *MNRAS*, 213, 257
- Girard, T. M., van Altena, W. F., Zacharias, N., et al. 2011, *AJ*, 142, 15
- Gizis, J. E. 1997, *AJ*, 113, 806

- . 2002, *ApJ*, 575, 484
- Gizis, J. E., Allers, K. N., Liu, M. C., et al. 2015, *ApJ*, 799, 203
- Gizis, J. E., Burgasser, A. J., Berger, E., et al. 2013, *ApJ*, 779, 172
- Gizis, J. E., Burgasser, A. J., Faherty, J. K., Castro, P. J., & Shara, M. M. 2011a, *AJ*, 142, 171
- Gizis, J. E., Kirkpatrick, J. D., & Wilson, J. C. 2001, *AJ*, 121, 2185
- Gizis, J. E., Monet, D. G., Reid, I. N., Kirkpatrick, J. D., & Burgasser, A. J. 2000a, *MNRAS*, 311, 385
- Gizis, J. E., Monet, D. G., Reid, I. N., et al. 2000b, *AJ*, 120, 1085
- Gizis, J. E., & Reid, I. N. 1997, *PASP*, 109, 849
- Gizis, J. E., Reid, I. N., Knapp, G. R., et al. 2003, *AJ*, 125, 3302
- Gizis, J. E., Troup, N. W., & Burgasser, A. J. 2011b, *ApJL*, 736, L34
- Gizis, J. E., Faherty, J. K., Liu, M. C., et al. 2012, *AJ*, 144, 94
- Goldman, B., Marsat, S., Henning, T., Clemens, C., & Greiner, J. 2010, *MNRAS*, 405, 1140
- Goldman, B., Röser, S., Schilbach, E., et al. 2013, *A&A*, 559, A43
- Golimowski, D. A., Leggett, S. K., Marley, M. S., et al. 2004, *AJ*, 127, 3516
- Gomes, J. I., Pinfield, D. J., Marocco, F., et al. 2013, *MNRAS*, 431, 2745
- Green, G. M., Schlafly, E. F., Finkbeiner, D. P., et al. 2014, *ApJ*, 783, 114
- Hall, P. B. 2002, *ApJ*, 564, L89
- Hambly, N. C., MacGillivray, H. T., Read, M. A., et al. 2001, *MNRAS*, 326, 1279
- Harrington, R. S., Dahn, C. C., Kallarakal, V. V., et al. 1993, *AJ*, 105, 1571
- Hawley, S. L., Covey, K. R., Knapp, G. R., et al. 2002, *AJ*, 123, 3409
- Henry, T. J., Jao, W.-C., Subasavage, J. P., et al. 2006, *AJ*, 132, 2360
- Henry, T. J., & Kirkpatrick, J. D. 1990, *ApJ*, 354, L29
- Henry, T. J., Subasavage, J. P., Brown, M. A., et al. 2004, *AJ*, 128, 2460
- Høg, E., Fabricius, C., Makarov, V. V., et al. 2000, *A&A*, 355, L27
- Huelamo, N., Ivanov, V. D., Kurtev, R., et al. 2015, *A&A*, 578, A1
- Irwin, M., McMahon, R. G., & Reid, I. N. 1991, *MNRAS*, 252, 61P
- Ivezić, Ž., Tyson, J. A., Abel, B., et al. 2008, *arXiv.org*, 0805.2366v4
- Jameson, R. F., Casewell, S. L., Bannister, N. P., et al. 2008, *MNRAS*, 384, 1399
- Kaiser, N., Burgett, W., Chambers, K. C., et al. 2010, in *Proc. SPIE, University of Hawai'i, USA*, 12
- Kellogg, K., Metchev, S. A., Gagné, J., & Faherty, J. 2016, *ApJL*, 821, L15
- Kellogg, K., Metchev, S. A., Geißler, K., et al. 2015, *AJ*, 150, 182
- Kendall, T. R., Delfosse, X., Martín, E. L., & Forveille, T. 2004, *A&A*, 416, L17
- Kendall, T. R., Jones, H. R. A., Pinfield, D. J., et al. 2007a, *MNRAS*, 374, 445
- Kendall, T. R., Maunon, N., Azzopardi, M., & Gigoyan, K. 2003, *A&A*, 403, 929
- Kendall, T. R., Tamura, M., Tinney, C. G., et al. 2007b, *A&A*, 466, 1059
- Kirkpatrick, J. D. 2005, *ARAA*, 43, 195
- Kirkpatrick, J. D., Beichman, C. A., & Skrutskie, M. F. 1997a, *ApJ*, 476, 311
- Kirkpatrick, J. D., Dahn, C. C., Monet, D. G., et al. 2001a, *AJ*, 121, 3235
- Kirkpatrick, J. D., Henry, T. J., & Irwin, M. J. 1997b, *AJ*, 113, 1421
- Kirkpatrick, J. D., Henry, T. J., & Liebert, J. 1993, *ApJ*, 406, 701
- Kirkpatrick, J. D., Henry, T. J., & McCarthy, D. W. J. 1991, *ApJS*, 77, 417
- Kirkpatrick, J. D., Henry, T. J., & Simons, D. A. 1995, *AJ*, 109, 797
- Kirkpatrick, J. D., Liebert, J., Cruz, K. L., Gizis, J. E., & Reid, I. N. 2001b, *PASP*, 113, 814
- Kirkpatrick, J. D., McGraw, J. T., Hess, T. R., Liebert, J., & McCarthy, D. W. J. 1994, *ApJS*, 94, 749
- Kirkpatrick, J. D., Reid, I. N., Liebert, J., et al. 1999, *ApJ*, 519, 802
- . 2000, *AJ*, 120, 447
- Kirkpatrick, J. D., Cruz, K. L., Barman, T. S., et al. 2008, *ApJ*, 689, 1295
- Kirkpatrick, J. D., Looper, D. L., Burgasser, A. J., et al. 2010, *ApJS*, 190, 100
- Kirkpatrick, J. D., Cushing, M. C., Gelino, C. R., et al. 2011, *ApJS*, 197, 19
- Kirkpatrick, J. D., Gelino, C. R., Cushing, M. C., et al. 2012, *ApJ*, 753, 156
- Kirkpatrick, J. D., Schneider, A. C., Fajardo-Acosta, S., et al. 2014, *ApJ*, 783, 122
- Kirkpatrick, J. D., Kellogg, K., Schneider, A. C., et al. 2016, *ApJS*, 224, 36
- Knapp, G. R., Leggett, S. K., Fan, X., et al. 2004, *AJ*, 127, 3553
- Koen, C. 2013, *MNRAS*, 428, 2824
- Koerner, D. W., Kirkpatrick, J. D., McElwain, M. W., & Bonaventura, N. R. 1999, *ApJ*, 526, L25
- Kraus, A. L., & Hillenbrand, L. A. 2009, *ApJ*, 703, 1511
- Lachapelle, F.-R., Lafreniere, D., Gagné, J., et al. 2015, *ApJ*, 802, 61
- Law, N. M., Hodgkin, S. T., & Mackay, C. D. 2006, *MNRAS*, 368, 1917
- Lawrence, A., Warren, S. J., Almaini, O., et al. 2007, *MNRAS*, 379, 1599
- . 2012, *VizieR On-line Data Catalog, II/314*, 0
- Leggett, S. K. 1992, *ApJS*, 82, 351
- Leggett, S. K., Allard, F., Berriman, G., Dahn, C. C., & Hauschildt, P. H. 1996, *ApJS*, 104, 117
- Leggett, S. K., Geballe, T. R., Fan, X., et al. 2000, *ApJ*, 536, L35
- Leggett, S. K., Golimowski, D. A., Fan, X., et al. 2002, *ApJ*, 564, 452
- Leggett, S. K., Saumon, D., Marley, M. S., et al. 2012, *ApJ*, 748, 74
- Leinert, C., Weitzel, N., Richichi, A., Eckart, A., & Tacconi-Garman, L. E. 1994, *A&A*, 291, L47
- Lépine, S., & Gaidos, E. 2011, *AJ*, 142, 138
- Lépine, S., Rich, R. M., Neill, J. D., Caulet, A., & Shara, M. M. 2002a, *ApJ*, 581, L47
- Lépine, S., Rich, R. M., & Shara, M. M. 2003a, *ApJ*, 591, L49
- . 2003b, *AJ*, 125, 1598
- Lépine, S., & Shara, M. M. 2005, *AJ*, 129, 1483
- Lépine, S., Shara, M. M., & Rich, R. M. 2002b, *AJ*, 124, 1190
- . 2003c, *ApJ*, 585, L69
- Lépine, S., Thorstensen, J. R., Shara, M. M., & Rich, R. M. 2009, *AJ*, 137, 4109
- Liebert, J., Dahn, C. C., Gresham, M., & Strittmatter, P. A. 1979, *ApJ*, 233, 226
- Liebert, J., & Gizis, J. E. 2006, *PASP*, 118, 659
- Liebert, J., Kirkpatrick, J. D., Cruz, K. L., et al. 2003, *AJ*, 125, 343
- Lindegren, L., Lammers, U., Bastian, U., et al. 2016, *A&A*, 595, A4
- Liu, M. C., Dupuy, T. J., & Allers, K. N. 2016, *ApJ*, 833, 96

- Liu, M. C., Dupuy, T. J., & Leggett, S. K. 2010, *ApJ*, 722, 311
- Liu, M. C., & Leggett, S. K. 2005, *ApJ*, 634, 616
- Liu, M. C., Leggett, S. K., Golimowski, D. A., et al. 2006, *ApJ*, 647, 1393
- Liu, M. C., Wainscoat, R. J., Martín, E. L., Barris, B., & Tonry, J. L. 2002, *ApJ*, 568, L107
- Liu, M. C., Deacon, N. R., Magnier, E. A., et al. 2011, *ApJL*, 740, L32
- Liu, M. C., Magnier, E. A., Deacon, N. R., et al. 2013, *ApJL*, 777, L20
- Lodieu, N. 2013, *MNRAS*, 431, 3222
- Lodieu, N., Boudreault, S., & Béjar, V. J. S. 2014, *MNRAS*, 445, 3908
- Lodieu, N., Deacon, N. R., & Hambly, N. C. 2012a, *MNRAS*, 422, 1495
- Lodieu, N., Dobbie, P. D., Cross, N. J. G., et al. 2013, *MNRAS*, 435, 2474
- Lodieu, N., Espinoza Contreras, M., Zapatero Osorio, M. R., et al. 2012b, *A&A*, 542, 105
- Lodieu, N., Hambly, N. C., & Jameson, R. F. 2006, *MNRAS*, 373, 95
- Lodieu, N., Hambly, N. C., Jameson, R. F., & Hodgkin, S. T. 2008, *MNRAS*, 383, 1385
- Lodieu, N., Hambly, N. C., Jameson, R. F., et al. 2007a, *MNRAS*, 374, 372
- Lodieu, N., Scholz, R.-D., & McCaughrean, M. J. 2002, *A&A*, 389, L20
- Lodieu, N., Scholz, R.-D., McCaughrean, M. J., et al. 2005, *A&A*, 440, 1061
- Lodieu, N., Zapatero Osorio, M. R., Martín, E. L., Solano, E., & Aberasturi, M. 2010, *ApJL*, 708, L107
- Lodieu, N., Zapatero Osorio, M. R., Rebolo, R., Martín, E. L., & Hambly, N. C. 2009, *A&A*, 505, 1115
- Lodieu, N., Pinfield, D. J., Leggett, S. K., et al. 2007b, *MNRAS*, 379, 1423
- Lodieu, N., Burningham, B., Day-Jones, A. C., et al. 2012c, *A&A*, 548, 53
- Looper, D. L. 2011, ProQuest Dissertations And Theses; Thesis (Ph.D.)—University of Hawai'i at Manoa
- Looper, D. L., Kirkpatrick, J. D., & Burgasser, A. J. 2007, *AJ*, 134, 1162
- Looper, D. L., Kirkpatrick, J. D., Cutri, R. M., et al. 2008, *ApJ*, 686, 528
- Loutrel, N. P., Luhman, K. L., Lowrance, P. J., & Bochanski, J. J. 2011, *ApJ*, 739, 81
- Lucas, P. W., Tinney, C. G., Burningham, B., et al. 2010, *MNRASL*, 408, L56
- Luhman, K. L. 2013, *ApJL*, 767, L1
- . 2014, *ApJ*, 786, L18
- Luhman, K. L., Mamajek, E. E., Allen, P. R., & Cruz, K. L. 2009, *ApJ*, 703, 399
- Luhman, K. L., & Sheppard, S. S. 2014, *ApJ*, 787, 126
- Luhman, K. L., Patten, B. M., Marengo, M., et al. 2007, *ApJ*, 654, 570
- Luhman, K. L., Loutrel, N. P., McCurdy, N. S., et al. 2012, *ApJ*, 760, 152
- Luyten, W. J. 1979, A Catalogue of Stars with Proper Motions Exceeding 0"2 Annually (NLTT Catalogue) (Minneapolis: Univ. Minnesota)
- Mace, G. N. 2014, ProQuest Dissertations and Theses, 75-09(E), 1
- Mace, G. N., Kirkpatrick, J. D., Cushing, M. C., et al. 2013, *ApJS*, 205, 6
- Magnier, E. A., Schlafly, E., Finkbeiner, D., et al. 2013, *ApJS*, 205, 20
- Magnier, E. A., Schlafly, E. F., Finkbeiner, D. P., et al. 2017, in preparation, arXiv:1612.05242
- Manjavacas, E., Goldman, B., Reffert, S., & Henning, T. 2013, *A&A*, 560, 52
- Marocco, F., Smart, R. L., Jones, H. R. A., et al. 2010, *A&A*, 524, 38
- Marocco, F., Andrei, A. H., Smart, R. L., et al. 2013, *AJ*, 146, 161
- Marocco, F., Jones, H. R. A., Day-Jones, A. C., et al. 2015, *MNRAS*, 449, 3651
- Marsh, K. A., Wright, E. L., Kirkpatrick, J. D., et al. 2013, *ApJ*, 762, 119
- Marshall, J. L. 2008, *AJ*, 135, 1000
- Martín, E. L., Basri, G., Zapatero Osorio, M. R., Rebolo, R., & García López, R. J. 1998, *ApJ*, 507, L41
- Martín, E. L., Brandner, W., & Basri, G. 1999a, *Science*, 283, 1718
- Martín, E. L., Brandner, W., Bouvier, J., et al. 2000, *ApJ*, 543, 299
- Martín, E. L., Delfosse, X., Basri, G., et al. 1999b, *AJ*, 118, 2466
- Martín, E. L., Rebolo, R., & Magazzu, A. 1994, *ApJ*, 436, 262
- Martín, E. L., Phan-Bao, N., Bessell, M., et al. 2010, *A&A*, 517, 53
- Matsuoka, Y., Peterson, B. A., Murata, K. L., et al. 2011, *AJ*, 142, 64
- McCarthy, M. F., Bertiau, F. C., & Treanor, P. J. 1964, *Ricerche Astronomiche*, 6, 571
- McCaughrean, M. J., Close, L. M., Scholz, R.-D., et al. 2004, *A&A*, 413, 1029
- McCaughrean, M. J., Scholz, R.-D., & Lodieu, N. 2002, *A&A*, 390, L27
- McElwain, M. W., & Burgasser, A. J. 2006, *AJ*, 132, 2074
- McGovern, M. R., Kirkpatrick, J. D., McLean, I. S., et al. 2004, *ApJ*, 600, 1020
- Metchev, S. A., Kirkpatrick, J. D., Berriman, G. B., & Looper, D. L. 2008, *ApJ*, 676, 1281
- Mohanty, S., & Basri, G. 2003, *ApJ*, 583, 451
- Monet, D. G., Dahn, C. C., Vrba, F. J., et al. 1992, *AJ*, 103, 638
- Monet, D. G., Levine, S. E., Canzian, B., et al. 2003, *AJ*, 125, 984
- Montagnier, G., Ségransan, D., Beuzit, J. L., et al. 2006, *A&A*, 460, L19
- Mugrauer, M., Seifahrt, A., Neuhäuser, R., & Mazeh, T. 2006, *MNRASL*, 373, L31
- Murphy, S. J., Lawson, W. A., & Bento, J. 2015, *MNRAS*, 453, 2220
- Murray, D. N., Burningham, B., Jones, H. R. A., et al. 2011, *MNRAS*, 414, 575
- Muzic, K., Radigan, J., Jayawardhana, R., et al. 2012, *AJ*, 144, 180
- Noll, K. S., Geballe, T. R., Leggett, S. K., & Marley, M. S. 2000, *ApJ*, 541, L75
- Phan-Bao, N. 2011, *Astronomische Nachrichten*, 332, 668
- Phan-Bao, N., & Bessell, M. S. 2006, *A&A*, 446, 515
- Phan-Bao, N., Guibert, J., Crifo, F., et al. 2001, *A&A*, 380, 590
- Phan-Bao, N., Bessell, M. S., Martín, E. L., et al. 2006, *MNRASL*, 366, L40
- . 2008, *MNRAS*, 383, 831
- Pineda, J. S., Hallinan, G., Kirkpatrick, J. D., et al. 2016, *ApJ*, 826, 73
- Pinfield, D. J., Burningham, B., Tamura, M., et al. 2008, *MNRAS*, 390, 304
- Pokorny, R. S., Jones, H. R. A., Hambly, N. C., & Pinfield, D. J. 2004, *A&A*, 421, 763
- Probst, R. G., & Liebert, J. 1983, *ApJ*, 274, 245
- Qi, Z., Yu, Y., Bucciarelli, B., et al. 2015, *AJ*, 150, 137
- Radigan, J., Jayawardhana, R., Lafreniere, D., et al. 2013, *ApJ*, 778, 36

- Radigan, J., Lafreniere, D., Jayawardhana, R., & Doyon, R. 2008, *ApJ*, 689, 471
- Rebolo, R., Zapatero Osorio, M. R., Madrugá, S., et al. 1998, *Science*, 282, 1309
- Reid, I. N. 2003, *AJ*, 126, 2449
- Reid, I. N., & Cruz, K. L. 2002, *AJ*, 123, 2806
- Reid, I. N., Cruz, K. L., & Allen, P. R. 2007, *AJ*, 133, 2825
- Reid, I. N., Cruz, K. L., Kirkpatrick, J. D., et al. 2008, *AJ*, 136, 1290
- Reid, I. N., & Gilmore, G. 1981, *MNRAS*, 196, 15P
- Reid, I. N., & Gizis, J. E. 2005, *PASP*, 117, 676
- Reid, I. N., Gizis, J. E., Kirkpatrick, J. D., & Koerner, D. W. 2001, *AJ*, 121, 489
- Reid, I. N., Hawley, S. L., & Gizis, J. E. 1995, *AJ*, 110, 1838
- Reid, I. N., Kirkpatrick, J. D., Gizis, J. E., et al. 2000, *AJ*, 119, 369
- Reid, I. N., Kirkpatrick, J. D., Liebert, J., et al. 2002, *AJ*, 124, 519
- Reid, I. N., Lewitus, E., Allen, P. R., Cruz, K. L., & Burgasser, A. J. 2006a, *AJ*, 132, 891
- Reid, I. N., Lewitus, E., Burgasser, A. J., & Cruz, K. L. 2006b, *ApJ*, 639, 1114
- Reid, I. N., & Walkowicz, L. M. 2006, *PASP*, 118, 671
- Reid, I. N., Cruz, K. L., Laurie, S. P., et al. 2003a, *AJ*, 125, 354
- Reid, I. N., Cruz, K. L., Allen, P., et al. 2003b, *AJ*, 126, 3007
- , 2004, *AJ*, 128, 463
- Reiners, A., & Basri, G. 2006, *AJ*, 131, 1806
- Reylé, C., & Robin, A. C. 2004, *A&A*, 421, 643
- Rice, E. L., Faherty, J. K., & Cruz, K. L. 2010, *ApJL*, 715, L165
- Riedel, A. R., Finch, C. T., Henry, T. J., et al. 2014, *AJ*, 147, 85
- Rodono, M., Ciatti, F., & Vittone, A. 1980, *AJ*, 85, 298
- Rodriguez, D. R., Zuckerman, B., Kastner, J. H., et al. 2013, *ApJ*, 774, 101
- Roeser, S., Demleitner, M., & Schilbach, E. 2010, *AJ*, 139, 2440
- Ruiz, M. T., Leggett, S. K., & Allard, F. 1997, *ApJ*, 491, L107
- Ruiz, M. T., Wischnjewsky, M., Rojo, P. M., & Gonzalez, L. E. 2001, *ApJS*, 133, 119
- Sahlmann, J., Lazorenko, P. F., Bouy, H., et al. 2016, *MNRAS*, 455, 357
- Sahlmann, J., Lazorenko, P. F., Ségransan, D., et al. 2014, *A&A*, 565, A20
- , 2015, *A&A*, 577, A15
- Salim, S., & Gould, A. 2003, *ApJ*, 582, 1011
- Salim, S., Lépine, S., Rich, R. M., & Shara, M. M. 2003, *ApJ*, 586, L149
- Sarro, L. M., Bouy, H., Berihuete, A., et al. 2014, *A&A*, 563, A45
- Saumon, D., & Marley, M. S. 2008, *ApJ*, 689, 1327
- Schilbach, E., Röser, S., & Scholz, R.-D. 2009, *A&A*, 493, L27
- Schlafly, E. F., Finkbeiner, D. P., Juric, M., et al. 2012, *ApJ*, 756, 158
- Schlafly, E. F., Green, G., Finkbeiner, D. P., et al. 2014, *ApJ*, 789, 15
- Schlieder, J. E., Bonnefoy, M., Herbst, T. M., et al. 2014, *ApJ*, 783, 27
- Schmidt, S. J., Cruz, K. L., Bongiorno, B. J., Liebert, J., & Reid, I. N. 2007, *AJ*, 133, 2258
- Schmidt, S. J., Hawley, S. L., West, A. A., et al. 2015, *AJ*, 149, 158
- Schmidt, S. J., West, A. A., Hawley, S. L., & Pineda, J. S. 2010, *AJ*, 139, 1808
- Schneider, A. C., Cushing, M. C., Kirkpatrick, J. D., et al. 2014, *AJ*, 147, 34
- Schneider, A. C., Greco, J., Cushing, M. C., et al. 2016a, *ApJ*, 817, 112
- Schneider, A. C., Melis, C., Song, I., & Zuckerman, B. 2011, *ApJ*, 743, 109
- Schneider, A. C., Windsor, J., Cushing, M. C., Kirkpatrick, J. D., & Wright, E. L. 2016b, *ApJL*, 822, L1
- Schneider, D. P., Greenstein, J. L., Schmidt, M., & Gunn, J. E. 1991, *AJ*, 102, 1180
- Schneider, D. P., Knapp, G. R., Hawley, S. L., et al. 2002, *AJ*, 123, 458
- Scholz, R.-D. 2010a, *A&A*, 515, 92
- , 2010b, *A&A*, 510, L8
- , 2014, *A&A*, 561, 113
- Scholz, R.-D., Bihain, G., Schnurr, O., & Storm, J. 2011, *A&A*, 532, L5
- , 2012, *A&A*, 541, 163
- Scholz, R.-D., Bihain, G., & Storm, J. 2014, *A&A*, 567, A43
- Scholz, R.-D., Lehmann, I., Matute, I., & Zinnecker, H. 2004a, *A&A*, 425, 519
- Scholz, R.-D., Lodieu, N., & McCaughrean, M. J. 2004b, *A&A*, 428, L25
- Scholz, R.-D., & Meusinger, H. 2002, *MNRAS*, 336, L49
- Scholz, R.-D., Meusinger, H., & Jahreiss, H. 2001, *A&A*, 374, L12
- Scholz, R.-D., Storm, J., Knapp, G. R., & Zinnecker, H. 2009, *A&A*, 494, 949
- Schweitzer, A., Scholz, R.-D., Stauffer, J., Irwin, M., & McCaughrean, M. J. 1999, *A&A*, 350, L62
- Seifahrt, A., Reiners, A., Almaghrbi, K. A. M., & Basri, G. 2010, *A&A*, 512, A37
- Sheppard, S. S., & Cushing, M. C. 2009, *AJ*, 137, 304
- Shkolnik, E. L., Anglada-Escudé, G., Liu, M. C., et al. 2012, *ApJ*, 758, 56
- Shkolnik, E. L., Liu, M. C., & Reid, I. N. 2009, *ApJ*, 699, 649
- Siegler, N., Close, L. M., Burgasser, A. J., et al. 2007, *AJ*, 133, 2320
- Siegler, N., Close, L. M., Cruz, K. L., Martín, E. L., & Reid, I. N. 2005, *ApJ*, 621, 1023
- Siegler, N., Close, L. M., Mamajek, E. E., & Freed, M. 2003, *ApJ*, 598, 1265
- Silvestri, N. M., Lemagie, M. P., Hawley, S. L., et al. 2007, *AJ*, 134, 741
- Sivarani, T., Lépine, S., Kembhavi, A. K., & Gupchup, J. 2009, *ApJL*, 694, L140
- Skrutskie, M. F., Cutri, R. M., Stiening, R., et al. 2006, *AJ*, 131, 1163
- Skrzypek, N., Warren, S. J., Faherty, J. K., et al. 2015, *A&A*, 574, A78
- Smart, R. L., Tinney, C. G., Bucciarelli, B., et al. 2013, *MNRAS*, 433, 2054
- Smith, L., Lucas, P. W., Burningham, B., et al. 2014a, *MNRAS*, 437, 3603
- Smith, L., Lucas, P. W., Bunce, R., et al. 2014b, *MNRAS*, 443, 2327
- Stern, D., Kirkpatrick, J. D., Allen, L. E., et al. 2007, *ApJ*, 663, 677
- Stone, J. M., Skemer, A. J., Kratter, K. M., et al. 2016, *ApJL*, 818, L12
- Strauss, M. A., Fan, X., Gunn, J. E., et al. 1999, *ApJ*, 522, L61
- Stumpf, M. B., Brandner, W., Bouy, H., Henning, T., & Hippler, S. 2010, *A&A*, 516, 37
- Stumpf, M. B., Brandner, W., Köhler, R., Bouy, H., & Henning, T. 2009, *COOL STARS*, 1094, 561
- Stumpf, M. B., Geißler, K., Bouy, H., et al. 2011, *A&A*, 525, 123
- Theissen, C. A., & West, A. A. 2014, *ApJ*, 794, 146
- Theissen, C. A., West, A. A., & Dhital, S. 2016, *AJ*, 151, 41
- Theissen, C. A., West, A. A., Shippee, G., Burgasser, A. J., & Schmidt, S. J. 2017, *AJ*, 153, 92
- Thompson, M. A., Kirkpatrick, J. D., Mace, G. N., et al. 2013, *PASP*, 125, 809
- Thorstensen, J. R., & Kirkpatrick, J. D. 2003, *PASP*, 115, 1207
- Tinney, C. G. 1993a, *ApJ*, 414, 279

- . 1993b, *AJ*, 105, 1169
- . 1996, *MNRAS*, 281, 644
- Tinney, C. G., Burgasser, A. J., & Kirkpatrick, J. D. 2003, *AJ*, 126, 975
- Tinney, C. G., Burgasser, A. J., Kirkpatrick, J. D., & McElwain, M. W. 2005, *AJ*, 130, 2326
- Tinney, C. G., Delfosse, X., Forveille, T., & Allard, F. 1998, *A&A*, 338, 1066
- Tinney, C. G., Mould, J. R., & Reid, I. N. 1993, *AJ*, 105, 1045
- Tinney, C. G., Reid, I. N., Gizis, J. E., & Mould, J. R. 1995, *AJ*, 110, 3014
- Tonry, J. L., Stubbs, C. W., Lykke, K. R., et al. 2012, *ApJ*, 750, 99
- Tremblin, P., Amundsen, D. S., Chabrier, G., et al. 2016, *ApJL*, 817, L19
- Tsvetanov, Z. I., Golimowski, D. A., Zheng, W., et al. 2000, *ApJ*, 531, L61
- van Altena, W. F., Lee, J. T., & Hoffleit, E. D., eds. 1995, *The General Catalogue of Trigonometric [Stellar] Parallaxes* (New Haven, CT: Yale University Observatory)
- van Biesbroeck, G. 1961, *AJ*, 66, 528
- van Leeuwen, F. 2007, *A&A*, 474, 653
- Vrba, F. J., Henden, A. A., Luginbuhl, C. B., et al. 2004, *AJ*, 127, 2948
- Wang, P. F., Chen, W. P., Lin, C. C., et al. 2014a, *ApJ*, 784, 57
- Wang, Y., Jones, H. R. A., Smart, R. L., et al. 2014b, *PASP*, 126, 15
- Weinberger, A. J., Boss, A. P., Keiser, S. A., et al. 2016, *AJ*, 152, 24
- West, A. A., Hawley, S. L., Bochanski, J. J., et al. 2008, *AJ*, 135, 785
- Wilson, J. C., Kirkpatrick, J. D., Gizis, J. E., et al. 2001, *AJ*, 122, 1989
- Wilson, J. C., Miller, N. A., Gizis, J. E., et al. 2003, in *IAU Symp. 211, Brown Dwarfs*, ed. E. L. Martín (San Francisco: ASP), 197
- Wright, E. L., Eisenhardt, P. R. M., Mainzer, A. K., et al. 2010, *AJ*, 140, 1868
- Wright, E. L., Skrutskie, M. F., Kirkpatrick, J. D., et al. 2013, *AJ*, 145, 84
- York, D. G., Adelman, J., Anderson, J. E. J., et al. 2000, *AJ*, 120, 1579
- Zacharias, N., Monet, D. G., Levine, S. E., et al. 2005, *VizieR On-line Data Catalog*, I/297, 0
- Zapatero Osorio, M. R., Béjar, V. J. S., Martín, E. L., et al. 2000, *Science*, 290, 103
- Zapatero Osorio, M. R., Béjar, V. J. S., Rebolo, R., Martín, E. L., & Basri, G. 1999, *ApJ*, 524, L115
- Zhang, Z. H., Pokorny, R. S., Jones, H. R. A., et al. 2009, *A&A*, 497, 619
- Zhang, Z. H., Pinfield, D. J., Day-Jones, A. C., et al. 2010, *MNRAS*, 404, 1817
- Zhang, Z. H., Pinfield, D. J., Burningham, B., et al. 2013, *MNRAS*, 434, 1005